SEDIMENT DYNAMICS IN AN ENERGETIC ESTUARY

By

Jesse Lopez
A DISSERTATION

Presented to the Division of Environmental and Biomolecular Systems
and the Oregon Health & Science University
School of Medicine
in partial fulfilment of
the requirements for the degree of

Doctor of Philosophy
February 2017

CERTIFICATE OF APPROVAL

This is to certify that the PhD dissertation of
Jesse Lopez
has been approved

_____
António Baptista (Mentor)

_____
Tawnya Peterson (Committee Chair)

_____
Guy Gelfenbaum (Committee Member)

_____
Holly Simon (Committee Member)

CONTENTS

ACKNOWLEDGEMENTS

I would like to thank my collaborators associated with CMOP especially Byron Crump, Craig McNeil, and Tom Sanford as well as their students, colleagues, and staffs for assistance in collection of data and data analysis. I thankful for the CMOP modeling team past and present including Yvette Spitz, Mojgan Rostaminia, Katie Morrice, and Clara Llebot for their feedback on modelling efforts. I am especially grateful to Tuomas Kärnä for his support, insight, and extensive contributions in ideas and software that have substantially eased the completion of this work. I'd also like to thank the staff at OHSU including Bonnie Gibbs, Jim Mohan, Ethan Van Matre and especially Charles Seaton, Paul Tuner, and Michael Wilkins for their support in the collection and processing of data and simulations. I would like to thank my supervisor during my practicum at Argonne National Laboratory, Jed Brown. I'd like to thank all of the committee members that I've had over the years including Rick Johnson, Holly Simon, Joe Needoba, Tawnya Peterson, and Guy Gelfenbaum. Finally, I'd like to thank my advisor Antonio Baptista for his support, guidance, and for providing the opportunity to complete this work.

This work was supported by the DOE CSGF, grant number DOE CSGF DE-FG02-97ER25308. The National Science Foundation partially supported this research through cooperative agreement OCE-0424602.

This work used the National Energy Research Scientific Computing Center (NERSC) a DOE Office of Science User Facility supported by the Office of Science of the U.S. Department of Energy under Contract No. DE-AC02-05CH11231, as well as the Extreme Science and Engineering Discovery Environment (XSEDE), National Science Foundation grant number ACI-1053575.

ABSTRACT

This study aims to characterize the suspended sediment dynamics of the Columbia River estuary and describe the impact of suspended sediment on the aquatic light field, using field observations and a numerical sediment model.

The model used for this study, SELFE, was optimized to improve computational efficiency and strong-scaling. The sediment model coupled to SELFE was then validated against a benchmark of idealized test cases and a realistic application to the Columbia River estuary. A yearlong simulation of the Columbia River was then skill assessed and analyzed to describe suspended sediment dynamics, dominant transport processes, and sediment pathways. An empirical predictive model for the light attenuation coefficient was derived from observations of photosynthetically active radiation and water quality variables. Results from the numerical sediment model were then used as inputs to the light model to describe the estuarine light field.

Results from the sediment model benchmark show that it reproduces analytical, semi-analytical, and laboratory results in idealized barotropic open channel and trench migration test cases. In an idealized baroclinic estuary, SELFE reproduces sediment dynamics representative of an idealized estuarine turbidity maximum (ETM) in a manner similar to other models and in agreement with theoretical estuarine circulation. In a realistic Columbia River estuary application, the model reproduces the variability and magnitude of suspended sediment concentrations with a bias in the vertical location when stratification is under-predicted. Analysis of yearlong simulations shows that mean advection dominates suspended sediment transport, but tidal pumping periodically produces residual upstream transport when the estuary is partially mixed. Suspended sediment transport is

predominantly in the along-channel direction with minor periodic lateral pulses, the largest of which occur in the North Channel. Integrated suspended sediment fluxes show that the main channels constitute the dominant sediment pathway, while secondary pathways cut through Cathlamet Bay and intertidal shoals upstream of the North Channel. A conceptual model of system-wide sediment dynamics describing the ETMs reveal a four stage tidal pattern modulated by stratification where erosion and transport largely occur during ebb and flood tides, and deposition occurs during high and low water stages. The empirical light attenuation model indicates that suspended sediment and CDOM are the dominant varying light attenuation factors. Applying numerical sediment model results to the light attenuation model suggests that the estuary is generally within the euphotic zone except in the deepest sections of the main channels. However, the extent and intensity of light limitation shows strong tidal, tidal month, and seasonal variability as a result of fluctuating circulation and suspended sediment dynamics.

The findings show that the SELFE sediment model is validated and capable of approximating estuarine sediment dynamics including those associated with the ETMs in the Columbia River estuary. Observations and model results indicate that suspended sediment concentrations depend largely on tidal range and riverine suspended load, but that the transport of suspended sediment follows a regular pattern driven by river discharge, tidal conditions, and stratification. The processes associated with this cycle occur in a region roughly collocated with the chemical estuary and constitute an ETM zone.

LIST OF TABLES

LIST OF FIGURES

LIST OF ABBREVIATIONS AND ACRONYMS

ETM(s)	**Estuarine Turbidity Maxim(um/a)**
SSP	**Suspended Sediment Patch**
CMOP-WP	**CMOP Winched Profiler**
CTD	**Conductivity Temperature Depth**
ADCP	**Acoustic Doppler Current Profiler**
OBS	**Optical Backscatter**
ADV	**Acoustic Doppler Velocimeter**
NTU	**Nephelometric Turbidity Units**
SSC	**Suspended Sediment Concentration**
SPM	**Suspended Particulate Matter**
CDOM	**Colored Dissolved Organic Matter**
MSL	**Mean Sea Level**
PAR	**Photosynthetically Active Radiation**
TKE	**Turbulence Kinetic Energy**
CREDDP	**Columbia River Estuary Data Development Program**
CRETM	**Columbia River Estuarine Turbidity Maxima**
RISE	**River Influences on Shelf Ecosystems**
CMOP	**Center for Coastal Margin Observation & Prediction**
SATURN	**Science and Technology University Research Network**
OC1	**CMOP 2012 Fall Cruise, North Channel Anchorage Site 1**

OC2	**CMOP 2012 Fall Cruise, North Channel Anchorage Site 2**
SELFE	**Semi-implicit Eulerian-Lagrangian Finite Element model**
FVCOM	**Finite Volume Community Ocean Model**
SUNTANS	**Stanford Unstructured-grid, Nonhydrostatic, parallel coastal ocean model**
ROMS	**Regional Ocean Modeling System**
NCOM	**Naval Research Laboratory Navy Coastal Ocean Model**
NARR	**North American Regional Reanalysis**
CSTM	**Community Sediment Transport Model**
GOTM	**General Ocean Turbulence Model**
GLS	**Generic Length Scale**
CSTM	**Community Sediment Transport Model**
MPI	**Message Passing Interface**
ELM	**Eulerian-Lagrangian Method**
TVD	**Total Variation Diminishing**
WENO	**Weighted Essentially non-oscillatory**
CFL	**Courant Friedrichs-Lewy**
XSEDE	**eXtreme Science and Engineering Discovery Environment**
NERSC	**National Energy Research Scientific Computing Center**
DOE	**Department of Energy**
NOAA	**National Oceanic and Atmospheric Administration**
USGS	**United States Geological Survey**

1 INTRODUCTION

Estuaries are the inland transitional environments that lie at the interface of rivers and oceans. Home and nursery grounds for a broad range of terrestrial and aquatic species, estuaries are among the most biologically productive environments providing habitat for ecologically, economically, and culturally important species ranging from benthic filter feeders to migratory salmon. Beyond provisioning an abundance of natural resources, estuaries provide access to both riverine and oceanic transport networks for migratory species and human commerce. These properties render regions adjacent to estuaries lucrative for human endeavors catalyzing development such that estuarine regions are amongst the most heavily populated on the planet.

An estuary is a dynamic environment where river discharge and tidal motion drive the mixing of buoyant fresh river water with dense marine water creating a river-to-ocean continuum. Along this continuum, water properties, especially salinity, vary substantially creating a rich diversity of ecological niches where specialized flora and fauna thrive. At a minute scale, microbial and bacterial communities perform biogeochemical transformations rendering estuaries natural filters of

terrestrially sourced nutrients.

An essential component of these biogeochemical processes, one that acts as both a constraint and a catalyst, are the sediment dynamics of a system. The interaction between the ocean, rivers, climate, and geology literally shape estuarine environments through the morphological processes of erosion and deposition. Furthermore, suspended sediment acts as a control on biology by limiting light penetration through the aquatic environment thereby acting as a constraint on primary productivity and benthic fauna while simultaneously providing cover for juvenile fish from avian predators.

This work is an effort to better describe the characteristics and variability of sediment dynamics and the effect of suspended sediment on the aquatic light environment in the Columbia River estuary using a numerical model informed by, and skilled assessed with, field observations.

1.1 Setting: The Columbia River estuary

The Columbia River is the second largest river by discharge in the contiguous United States and is the largest single source of fresh water to the Northeast Pacific Ocean (Simenstad et al., 1990) (Figure 1). The vast drainage basin includes portions of two Canadian provinces and seven states in the Pacific Northwest and Northern Rocky Mountain regions of the continental United States. The Columbia River has been extensively dammed to aid in flood control, provide water for irrigation in the arid region west of the Cascades, and to enable the generation of hydroelectric power (Fox et al., 1984). Management of the river system has substantially altered the hydrograph. The annual mean and freshet discharge rates have decreased compared to the pre-dam era, whereas discharge during the

Fall and Winter seasons has increased due to the release of stored water in reservoirs for hydroelectric power generation (Sherwood et al., 1990a). To facilitate the development of pasture for cattle in the nineteenth century and shipping commerce in the twentieth century, the lower estuary has been extensively modified through the use of hydraulic structures and regular dredging (Sherwood et al., 1990a). These changes have reduced the volume of the estuary, limited the tidal influence, and focused more of the river discharge into the deep main channels (Fox et al., 1984).

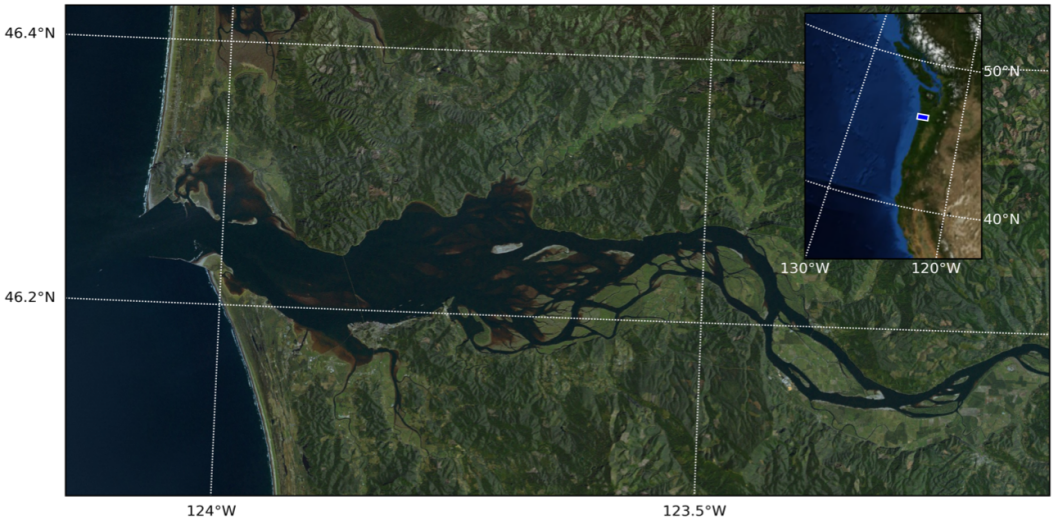

Figure 1 The Columbia River estuary.

The Columbia River estuary is a drowned river plain estuary formed during a period of rapid sea-level rise following the last Pleistocene (Sherwood & Creager, 1990). Like other west coast estuaries, the Columbia River is inundated with mixed, semi-diurnal tides; the mean tidal range is ~2.5 m, varying from ~1.6 to 3.6 m between neap and spring tides (Chawla et al., 2008). The river discharge at Beaver Army Terminal ranges from 3,000 $m^3 s^{-1}$ during low flow conditions up to 20,000 $m^3 s^{-1}$ during large freshets with an annual average of ~8,000 $m^3 s^{-1}$

(Chawla et al., 2008; Fox et al., 1984). In periods of low and intermediate river discharge, the estuary migrates between partially mixed (spring tides) and strongly stratified (neap tides) regimes. High river discharge causes the estuary to adjust and oscillate between time-depended salt wedge (spring tides) and salt wedge (neap tides) regimes. Two large channels and broad intertidal shoals dominate the topography of the lower estuary. The North Channel receives the majority of the tidal prism while the majority of the river flows through the regularly dredged South Channel (Chawla et al., 2008). The velocities of two main channels are far higher than the adjacent shallow regions (Chawla et al., 2008). However, the tidal velocities and the length of the salt intrusion have decreased due to the construction of the jetty system (Sherwood et al., 1990a). The channelization of the estuary focuses the salinity intrusion into the two main channels with a mean distance of approximately 25 km and a maximum of 41 km during periods of low river discharge (Chawla et al., 2008; Fox et al., 1984; Sherwood et al., 1990a).

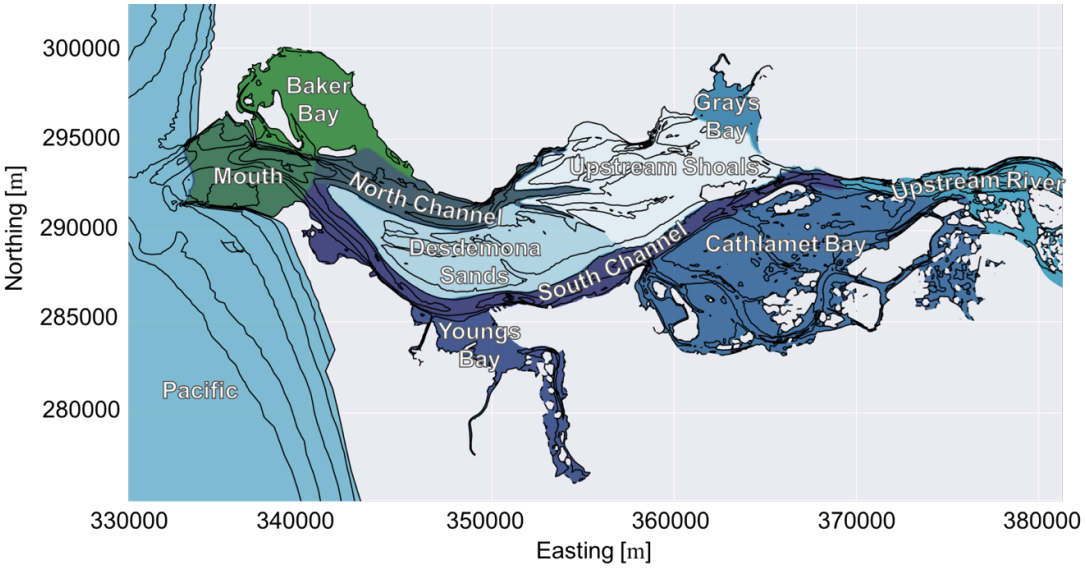

Figure 2 Regions within the Columbia River estuary in the Oregon state plane coordinate system.

The presence of four lateral bays provide sanctuaries of slower, shallower waters compared to those found in the main channels (Figure 2). Two lateral bays lie north of the main channels. Located near the mouth, the brackish Baker Bay lies mostly protected from the North Channel by the pair of Sand Islands and dikes. A large channel meandered through Baker Bay before the construction of jetties and pile dikes and dredging diverted the majority of ebbing river flow through the South Channel (Sherwood et al., 1990). The remnants of this channel and a broader complex form the largest and deepest channels in the North Channel and upstream shoals (Sherwood et al., 1990). Further upstream, the smaller Grays Bay remains completely fresh except for low flow periods. Similarly, there are two adjacent bays to the south of the main channel. Adjacent to the South Channel, the brackish Youngs Bay lies between Hammond and Astoria, in Oregon. Cathlamet Bay, a shallow region composed of numerous marshes and channels, lies upstream and is subject to periodic salinity intrusions during low flow conditions.

1.2 Previous sudies of the Columbia River estuary

Simenstad et al. (1990) provided a thorough history of the scientific observations of the Columbia River estuary which is summared below. Surveys of the bathymetry and tides began in the 1850s with a series of detailed projects in 1867-75, 1935-1939, and 1958. The U.S. Army Corps of Engineers (USACE) conducted a series of studies associated with dredging projects in 1932 and 1959 producing influential descriptions of salt transport, flushing time, estuarine classification, and circulation theory (Hansen & Rattray, 1966; Hughes & Rattray, 1980; Neal, 1965). The same project produced descriptions of erosion, bed load, and suspended sediment load using observations and laboratory studies (O'Brien, 1972).

Concerned about the transport of radionuclides from the Hanford Site, the U.S. Atomic Energy Commission supported physical studies of the estuary. These studies produced early descriptions of circulation and transport (Lutz et al., 1971; Perkins et al., 1966), transport of particulate and dissolved material (Conomos et al., 1972; Conomos & Gross, 1972), and the river plume (Barnes et al., 1972). These studies also provided descriptions of the distribution of sediment size classes, bedforms, and evidence of the estuarine turbidity maxima (ETMs) (Hubbell & Glenn, 1973). Studies in support of dredging by the USACE produced updated descriptions of bathymetry, suspended sediment load, and hydrodynamics (Sternberg et al., 1977). A focused study of the ETMs described them as advective features with concentrations of suspended sediments varying over tidal month and seasonal time scales (Gelfenbaum, 1983).

The Columbia River Estuary Data Development Program (CREDDP) program characterized the hydrodynamics, sedimentology, and ecology of the estuary. The substantial body of work was summarized in a comprehensive atlas (Fox et al., 1984) and a circulation focused manuscript (Jay, 1984). The Columbia River Estuarine Turbidity Maxima (CRETM) project focused on understanding how ETMs trap particulate matter leading to enhanced biogeochemical productivity (Simenstad et al., 1994). A number of manuscripts were produced from this project including descriptions of processes driving estuarine circulation and the ETMs (Jay & Musiak, 1994; Jay & Musiak, 1995), bacterial productivity in the ETMs (Baross et al., 1994; Crump et al., 1999), biogeochemical transformations (Prahl et al., 1997), primary production (Lara-Lara et al., 1990a; Lara-Lara et al., 1990b), copepod populations (Morgan et al., 1997), and the conceptual model of the ETMs as a “particle conveyor belt” (Small & Prahl, 2004).

The RISE project (Hickey et al., 2010) focused on the Columbia River plume producing a number of works on modeling plumes using three-dimensional models (Banas, MacCready, & Hickey, 2009; Banas et al., 2009; MacCready et al., 2009), the physics of the plume (Horner-Devine, 2009; Kilcher & Nash, 2010; Nash et al., 2009; Pan & Jay, 2009), effects of the plume on biology (Banas et al., 2009; Frame & Lessard, 2009; Kudela & Peterson, 2009; Peterson & Peterson, 2009), and particle dynamics (Spahn et al., 2009). Other projects have focused on the dynamics and suspended sediment dynamics near the mouth including descriptions of the littoral cell over short- (Ruggiero et al., 2005) and long-terms (Gelfenbaum et al., 1999; Gelfenbaum & Kaminsky, 2010) and validation of a coupled three-dimensional hydrodynamic-wave model (Elias et al. 2012).

The Center for Coastal Margin Observation & Prediction (CMOP) has leveraged previous studies and has worked to improve the characterization of local regions within the Columbia River estuary that are exceptionally biologically productive including the ETMs. The CMOP program oversaw the maturation of previous generations of physically focused observation systems (Steere et al., 2000) into the SATURN observation network which provides long-term, real-time time series of physical and biogeochemical variables (Baptista et al., 2008; Baptista et al., 2015). Field observations from the SATURN network and research cruises supported by modeling efforts have enchanced characterizations of microbial distribution (Fortunato et al., 2013; Fortunato & Crump, 2011, 2015; Smith et al., 2010), the origin of organic matter in the ETMs (Herfort et al., 2011), descriptions of a blooming protist (Herfort et al. 2011; Herfort et al., 2011), and biogeochemical transformations (Fortunato & Crump, 2015; Pfeiffer-Herbert et al., 2015; Smith et al., 2015; Smith, et al., 2013).

1.3 Research objectives

Despite the previous studies, significant gaps remain in the core characterization of suspended sediment dynamics and the ETMs in the Columbia River estuary. The literature is not even consistent about the number of ETMs in the system, often identifying only the two ETMs located in the main channels (Small & Prahl, 2004) but occasionally referencing also a third ETM located near the mouth and topographically trapped (Fain et al., 2001; Jay & Musiak, 1994). Many studies suggest that the ETMs materialize and dissipate within a tidal month period (Gelfenbaum, 1983; Jay & Musiak, 1994; Reed & Donovan, 1994), but observations from the SATURN observatory (Baptista et al., 2015) and CMOP research cruises suggest that ETMs are persistent migrating features. The origin of material for the ETMs has been described as predominantly riverine (Fox et al., 1984), but DNA analyses of particulate organic material suggests oceanic influence (Herfort et al., 2011; Smith et al., 2013). Interaction of suspended sediment from lateral bays and intertidal shoals with the main channels has been hypothesized and inferred, but never verified with observations or model results (Fain et al., 2001; Sherwood et al., 1990a). The channelization of the estuary has likely made the main channels the dominant sediment pathways, but the importance of other pathways through the lateral bays and the upstream shoals remains undescribed. Improved descriptions of the temporal and spatial variability of suspended sediment would enhance understanding of suspended sediment transport through the estuary and would provide important contextual information about the ETMs including temporal evolution and the origin of source material.

The turbidity of the water affects biology by attenuating light penetration through the water column and thereby acting as a control on primary production and

benthic flora and by providing cover for juvenile salmonids from predators (Bottom et al., 2005). The spatial distribution of turbidity and the effects on the aquatic light environment, primary productivity, and juvenile salmon nursery habitat remains very coarsely described (Lara-Lara et al., 1990a; Lara-Lara et al., 1990b). An improved description of the spatial distribution of turbidity and its subsequent effects on these processes will improve the understanding of the sediment dynamics in the estuary. It will also help to enable future high-level characterizations and estimates of biogeochemical processes strongly associated sediment dynamics and the ETMs.

The objective of this research project is to better characterize suspended sediment dynamics and their effect on the light environment in the Columbia River estuary using a combination of numerical model results and observation data. Specifically, the detailed objectives are to:

1. Develop and validate a SELFE-based sediment model of the Columbia River estuary capable of describing suspended sediment variability.
2. Describe the characteristics, patterns, and relationship between the North and South Channel ETMs in the Columbia River estuary including the variability over tidal to seasonal time scales.
3. Identify the dominant transport processes that drive suspended sediment dynamics including those associated with ETMs.
4. Characterize the dominant sediment pathways through the estuary.
5. Develop an empirical light attenuation model from observations of PAR and water quality variables.
6. Apply results from the numerical sediment model to the light attenuation

model to create system-wide descriptions of the estuarine light environment.

1.4 Document Organization

This work is organized into five chapters.

This chapter, Chapter 1, introduces the Columbia River estuary, describes previous and contemporary studies with relevance to sediment dynamics and the ETMs, and details the objectives of this work.

Chapter 2 describes the numerical model used in this study including the governing equations, discretization, and implementation details for the sediment model. The sediment model is then validated against three idealized tests and a realistic application to the Columbia River estuary. Model skill and limitations are described.

A yearlong sediment model simulation of the Columbia River estuary for 2012, skill assessed against observations from the SATURN observatory, is presented in Chapter 3. Suspended sediment dynamics, dominant pathways, transport processes over sub-tidal to seasonal time scales, and a three-dimensional conceptual model of sediment dynamics are described from model results.

Chapter 4 describes the development of an empirically derived model for the light attenuation coefficient. Sediment model results are applied to the light attenuation model to describe time and spatially varying light extinction coefficient and photic depth for the entire system for 2012. Implementation of the light extinction coefficient model in the numerical sediment model and results from a brief test are described.

Chapter 5 summarizes the work described here providing a discussion of implications, limitations, and suggested future work.

2 SEDIMENT MODEL BENCHMARK

2.1 Introduction

Sediment dynamics of estuaries control morphodynamic and biogeochemical processes with implications ranging from ecosystem function and health (Ferguson et al., 1996) to navigation (Meade, 1972) among other aspects of system sustainability, management and operation. Driven by tides and buoyancy, estuarine circulation commonly leads to a complex vertical structure of density and currents requiring three-dimensional modeling to represent the inherently depth-varying circulation and sediment processes. As a consequence, sediment modules have been developed for existing three-dimensional circulation models including structured grid models such as Delft3D (Lesser et al., 2004) and ROMS (Warner et al., 2008) and unstructured grid models including FVCOM (Chen et al., 2003), SUNTANS (Fringer et al., 2006), and SELFE (Zhang & Baptista, 2008) and its derivative SCHISM (Zhang et al., 2016). Regardless of the grid structure and specific numerics, sediment modeling systems generally solve the advection-

diffusion equation for a user-defined number of suspended sediment classes with distinct approaches for boundary conditions, interactions with bathymetry, and bed load transport.

Validation of sediment models has consisted predominantly of idealized cases with assessments against analytical or laboratory results. Open channel cases without density effects requiring reproduction of a Rouse profile are a common test to evaluate suspended sediment dynamics (Lesser et al., 2004; Pinto et al., 2012; Warner et al., 2008). The trench migration test case of *van Rijn* (1986) is commonly used to evaluate simulation skill for predictive bedload and morphodynamic behavior (Lesser et al., 2004; Pinto et al., 2012; Warner et al., 2008). Idealized estuarine test cases that include density effects have been used to evaluate sediment behavior in controlled conditions, but lack quantitative solutions (Burchard & Baumert, 1998; Warner et al., 2008). Validation tests inclusive of short wave effects include both laboratory experiments (Lesser et al., 2004) and comparisons against field observations (Warner et al., 2008).

Realistic applications of suspended sediment models are frequently used to study processes associated with estuarine turbidity maxima (ETM). *Brenon & Hir* (1999) studied the development of the Seine ETM using a single non-cohesive class with a parameterization derived from literature values. *Burchard et al.* (2003) used a single non-cohesive class characteristic of that system to simulate and study the Elbe ETM using GETM. *Lin et al.* (2003) characterized the ETM and a secondary turbidity maximum in the York River using a single non-cohesive class with other parameterizations derived from sensitivity studies. *de Nijs & Pietrzak* (2012) evaluated the skill of Delft3D to represent the characteristics of multiple ETMs in the stratified Rotterdam Waterway in realistic conditions using a single

non-cohesive sediment size class, with the derivation of sediment parameterization details not disclosed. *Ralston et al.* (2012) used four non-cohesive classes with sediment parameterization based on previous studies to describe the effects of bathymetry on sediment transport in the Hudson using ROMS. In another study with multiple classes, *Ralston et al.* (2013) used three non-cohesive classes to study sediment dynamics along intertidal flats in the Skagit Bay using FVCOM with the parameterization derived from available observations and literature values.

The aim of this paper is to validate an unstructured grid sediment model coupled to SELFE through a combination of idealized test cases (barotropic open channel, barotropic trench migration, and baroclinic tidally driven estuary) and a realistic application to an energetic estuary. The idealized tests are drawn from literature, and are designed to assess model skill at representing essential processes: suspended sediment transport, erosion and deposition, bed load transport, and morphological evolution. Model sensitivity to hydrodynamic and sediment parameterizations are described and optimal results are qualitatively compared against previous work and available analytical, semi-analytical, or laboratory results. Field observations from endurance stations and shipborne instrumentation in Columbia River estuary, USA are used to assess model skill in representing observed sediment dynamics in the complex and energetic Columbia River estuary. To facilitate future model inter-comparison and to promote the improvement in skill of sediment models, the tests and data are publically available as a benchmark (Lopez & Baptista, 2016b).

2.2 Methods

2.2.1 Hydrodynamics model

SELFE (Zhang & Baptista, 2008) solves the Reynolds-averaged Navier-Stokes equations using both hydrostatic and Boussinesq assumptions. The governing equations are solved in a semi-implicit finite element (P_1-P_{NC}) framework using a combination of numerical methods. The advection of momentum is solved with a semi-Lagrangian method following *Casulli & Cheng* (1992). Scalar transport is solved using either upwind or total variation diminishing (TVD) Eulerian finite volume methods. Beyond the intrinsic differences between upwind and TVD, in SELFE the upwind scheme includes an implicit calculation of vertical flux, whereas TVD utilizes an explicit calculation resulting in a much slower time to solution. Comparisons of upwind and TVD transport schemes reveal minor differences in model skill of temperature and salinity in the Columbia River estuary. Because of the minor differences in skill and large differences in computational cost, we chose to use the much faster upwind scheme. Governing equations are closed by the general length scale (GLS) equations (Umlauf & Burchard, 2005) implemented in either a native SELFE implementation or by on-line coupling the GOTM library. The domain is discretized using a triangular, unstructured mesh in the horizontal similar to a hybrid CD grid and a hybrid Z- and S-level approach in the vertical.

In this chapter we discuss the implications of two distinct treatments for the solution of the momentum equation at the bottom boundary on represented sediment dynamics. As is common in coastal hydrodynamic models, SELFE uses a bottom boundary condition where the internal Reynolds stress is balanced with the stress from bottom friction

$$\nu \frac{\partial u}{\partial z} = \tau_b \tag{1}$$

where ν is the vertical eddy viscosity, u is the velocity, z is the vertical coordinate, and τ_b is the bottom stress. Assuming a turbulent boundary layer, a logarithmic velocity profile in the bottom boundary layer, and using turbulence closure theory to find the eddy viscosity results in a constant Reynolds stress in the bottom boundary layer:

$$\nu \frac{\partial u}{\partial z} = \frac{\kappa_0}{ln(\delta_b/z_o)} \sqrt{C_D} |u_b| u_b \tag{2}$$

where C_d is the drag coefficient, z_0 is the bottom roughness, κ_0 is the von Karman, δ_b is the thickness of the computational cell, and $\boldsymbol{u_b}$ is the bottom velocity (Zhang & Baptista, 2008). Specifically, $\boldsymbol{u_b}$ is taken to be the velocity at the top of the bottommost computational cell. Traditionally in SELFE, the discretized momentum equation was solved from the free surface to the top of the bottommost computational cell with the bottom node assigned a velocity of 0 to be consistent with a log layer adhering to the law of the wall. A new implementation, starting with version 4.0 of SELFE, solves the momentum equation from the surface to the bottom node to be consistent with the finite element formulation resulting in a non-zero velocity at the bottom node and an improved representation of the bottom boundary layer. The two implementations produce distinct estimates of $\boldsymbol{u_b}$ used in Equation 2 resulting in distinct representations of bottom stress and shear. The implications of the new bottom boundary treatment of momentum for sediment modelling are discussed in idealized test cases. For convenience in differentiation, we refer to the traditional implementation as "no-

slip" and the newer treatment as "slip" recognizing that formally both treatments are partial slip conditions.

2.2.2 Sediment model

The sediment model evaluated here is derived from the Community Sediment Transport Model (CSTM) (Warner et al., 2008). The non-cohesive classes, bed property changes, and bed morphology from the CSTM model were ported by *Pinto et al.* (2012) to work with the unstructured grids and methods used in SELFE. The model used here is algorithmically similar to *Pinto et al.* (2012), but was substantially refactored to align more closely with the original CSTM implementation. Minor implementation changes to improve stability including limiting slopes and increasing checks for numerically undefined numbers were required for the model to work in the Columbia River domain.

The sediment model solves for the time evolution of suspended sediments in three-dimensions and morphological changes. Specifically, the model calculates the vertical settling, bed load transport, and interactions with the bed through erosion and deposition for a user-defined number of non-cohesive classes. Suspended sediment concentrations are calculated by solving the advection-diffusion equation with additional terms for settling velocity and horizontal velocity

$$\frac{\partial C_n}{\partial t} + u\frac{\partial C_n}{\partial x} + v\frac{\partial C_n}{\partial y} + w\frac{\partial C_n}{\partial z} = \frac{\partial}{\partial z}\left(\kappa\frac{\partial C_n}{\partial z}\right) + w_{s,n}\frac{\partial C_n}{\partial z} + F_h \qquad (3)$$

where C_n is the sediment concentration of class n, (u, v, w) are the directional velocity components, κ is the eddy diffusivity, $w_{s,n}$ is the settling velocity of class n, and F_h is the horizontal diffusion. Equation 3 is solved using either the upwind or

TVD transport schemes in SELFE (Zhang & Baptista, 2008). The vertical movement of sediment is handled using a hybrid WENO-PPM semi-Lagrangian method (Warner et al., 2008). Multiple bed layers are supported and erosional flux is calculated using the method outlined by *Harris & Wiberg* (2001). Specifically, the depositional flux, D_n, is calculated using

$$D_n = w_{s,n} \cdot c_b \tag{4}$$

where $w_{s,n}$ is the settling velocity for sediment class n and C_b is the total sediment concentration in the bottom cell. The erosional flux for sediment class n, E_n, is defined as

$$E_n = \begin{cases} E_{0,n}(1-p) f_p \left(\dfrac{\tau_{sf}}{\tau_{cr,n}} - 1 \right), & if\ \tau_{sf} > \tau_{cr,n} \\ 0, & otherwise \end{cases} \tag{5}$$

where $E_{0,n}$ is the bed erodibility constant, p is the porosity of the top layer of the sediment, f_p is the volumetric fraction, τ_{sf} is the bed shear stress, $\tau_{cr,n}$ is the critical shear stress, $d_{50,n}$ is the median sediment diameter, $\rho_{s,n}$ is the density of the sediment, and ρ_w is the density of the water. Bed load calculations use the formulation of either *Meyer-Peter & Müller* (1948) or *van Rijn* (2007). Updates to bathymetry resulting from erosion, deposition, and bed load, the Exner equation, are calculated using the SAND2D bottom update module (Fortunato & Oliveira, 2004). This module uses a finite volume method where the sediment flux is conserved over the cells neighboring a node center using a forward Euler time-stepping scheme. The sediment module is also two-way coupled to the hydrodynamics of SELFE through the equation of state

$$\rho = \rho_o + \sum_{n=1}^{N} \frac{C_n}{\rho_{s,n}} \left(\rho_{s,n} - \rho_w \right) \tag{6}$$

where the new density ρ includes densities of water and each sediment class weighted by their respective concentrations.

2.2.3 Model skill assessment

As is common practice in applied sediment modeling, an important part of the skill assessment in this paper is qualitative. However, we also explore quantitative metrics that are commonly used in circulation modeling: root mean square error (RMSE), Willmott Score (WS), Murphy Score (MS), correlation coefficient (Corr), and bias**.**

The root mean square error (RMSE) is defined as

$$RMSE = \sqrt{\langle (m-o)^2 \rangle} \tag{7}$$

where $m = m_{i\,i=1}^{n}$ are the modeled time series, $o = o_{i\,i=1}^{n}$ are the observed times series, and $\langle \cdot \rangle$ indicates the average over the series. The primary advantage of using RMSE results from the intuitive interpretation because the metric and measured values sharing the same units. A disadvantage of using RMSE is the large weight outliers impart on the metric and that it does not provide a means to compare variables measured in different units.

In contrast, the Willmott score (WS) allows comparison between variables because it is non-dimensional (Willmott, 1981). The WS is defined as

$$WS = 1 - \frac{\langle (m-o)^2 \rangle}{\langle (|m - \langle o \rangle| + |o - \langle o \rangle|)^2 \rangle} \tag{8}$$

A frequent criticism of the WS is the yielding of high skill scores for unrelated time series (Ralston et al., 2010).

An alternative skill metric that is not as susceptible to outliers, is non-dimensional, and allows for comparisons between units is the Murphy Score (MS),

$$MS = 1 - \frac{\langle (m-o)^2 \rangle}{\langle (m_r - o)^2 \rangle} \quad (9)$$

where m_r is the reference model that is compared against. A Murphy Score of 1 indicates a perfect model, 0 (zero) indicates that the model is equivalent to the reference model, and a negative score indicates skill worse than the reference. In this study we typically use the mean of the observations as the reference model. However, for the trench migration test in Section 2.3.2 the reference model is the initial depth, and, following common nomenclature in the morphological literature (Sutherland et al., 2004), we refer in that case to the Murphy Score as the Brier Skill Score (BSS).

Finally, we also consider both correlation coefficient and bias for comprehensive purposes. The correlation coefficient, $Corr$, is a measure of linear correlation between two signals defined as

$$Corr = \frac{\mathrm{COV}(m,o)}{\sigma_m \sigma_o} \quad (10)$$

where $\mathrm{COV}(m,o)$ is the covariance of model results m and observations o and their respective standard deviations are denoted by σ_m and σ_o. The bias, is simply the mean difference between the model results and observations.

2.3 Idealized tests

2.3.1 Transport: Steady open channel

This test evaluates the simulated transport of suspended sediment in an unstratified open channel and has been studied previously in *Warner et al.* (2008) and *Pinto et al.* (2012). The domain is a long open channel (L = 10,000 m, W = 1,000 m, H = 10 m) with a constant slope of 4 x 10^{-5} m m^{-1}. The boundary

conditions consist of a fixed depth of 10 m imposed at the downstream end and a logarithmic velocity profile applied at the upstream boundary with a depth-averaged velocity of 1 m s^{-1}. The horizontal grid consists of 2,000 elements and 1,111 nodes, and 21 S-levels ($\theta_b = 1$ and $\theta_f = 3$) were used in the vertical. Both the SELFE and GOTM implementations of the GLS equations were tested to evaluate the effects of turbulence closure on the solution. Specifically, from the native SELFE GLS implementation we use *k-kl*, *k-ε*, and *k-ω* with the Kantha-Clayson stability function and *k-ε* and *k-ω* with the Canuto-A stability function from the GOTM library (Table 1). Strict direct comparisons between SELFE and GOTM implementations of the GLS equations are not possible for any specific closure model. The SELFE implementation does not have an option for the Canuto-A stability function, and GOTM would not converge to a solution when using Kantha-Clayson. Nevertheless, the selected turbulence closure models demonstrate important differences between the GLS implementation in GOTM and SELFE.

Table 1 Model parameters for open channel test.

Parameter	Variables	Values
H-Grid	# nodes, # elems	1111, 2000
V-Grid	# S-levels	21
V-Grid	H_c, θ_b, θ_f	5.0, 1.0, 3.0
Time step	dt [s]	90
Bottom roughness	Z_{ob} [m]	0.0053
Initial density profile	[dp/dz]	0
Simulation length	[days]	1
Settling velocity	w_s [mm/s]	1
Erosion rate	E_o [kg/m^2/s]	5 x 10^{-5}
Critical stress	τ_{ce} [N/m^2]	0.05
Porosity	Φ	0.9
Bed slope	S_o	4 x 10^{-5}
Horizontal boundary condition	$\overline{\boldsymbol{u}}$ [m/s]	1

We compare the effects of the selection of the turbulence closure model and bottom boundary treatment on eddy diffusivity, turbulent kinetic energy (TKE), suspended sediment concentrations (SSC) and velocity profiles against semi-analytical and analytical solutions. (J. Paul Rinehimer, personal communication; See Appendix A). The analytical solution assumes a Prandlt number of 0.8, a logarithmic velocity profile, a no-slip bottom boundary treatment, a Rouse SSC profile, and setting the free parameter z_0 to 0.0053 m to match the numerical experiments. The numerical semi-analytical solution is obtained from the numerical model by imposing a parabolic eddy viscosity, K_M, and eddy diffusivity, K_H, instead of using a GLS turbulence closure model. The semi-analytical eddy viscosity and eddy diffusivity apply the same assumptions used in the calculations of the analytical solution.

Figure 3 shows the results using the "no-slip" bottom boundary described in Section 2.2.1. All turbulence closures capture the analytical solution of velocity well, but underestimate near-bed velocities (Panel A). The SELFE implemented closures tend to underestimate velocity. The semi-analytical solution uniquely overestimates velocity throughout the water column compared to the analytical solution. The eddy diffusivity (Panel C) is underestimated for all closures, consistent with the findings of *Warner et al.* (2008) and *Pinto et al.* (2012). The native SELFE implementation of the GLS produces eddy diffusivity profiles distinctively skewed near the surface (k-ε and k-ω) and bottom (k-ε), whereas the GOTM closures produce smoother, non-symmetric profiles. Profiles for TKE (Panel D) feature large spikes one level above the bottom for all closures, but are amplified for SELFE implemented closures. SSC profiles (Panel B) are underestimated compared to the analytical and semi-analytical solutions, as found

in previous studies (Pinto et al., 2012; Warner et al., 2008). SSC profiles result from a balance of the sediment settling velocity and the upward velocity from the eddy diffusivity implicating the underprediction of erosion and eddy diffusivity in the resulting in the underestimate of SSC.

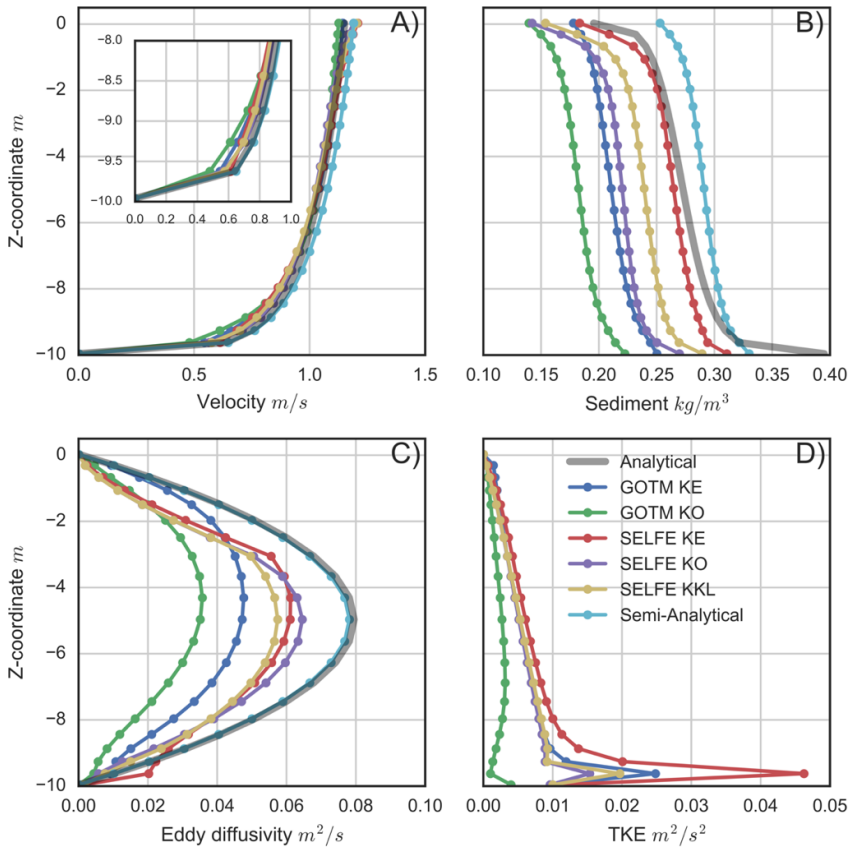

Figure 3 Profiles of model results from open channel case with a no slip bottom boundary condition. Velocity (A), suspended sediment (B), eddy diffusivity (C), and TKE (D).

For contrast, Figure 4 shows results using the "slip" bottom boundary treatment. As was the case with the "no-slip" treatment, velocity profiles are well represented by all closures (Panel A), with the semi-analytical solution producing distinctive overestimations. However, all closures overestimate near-bottom velocities and most underestimate surface velocities when used with the "slip" bottom boundary. All closures again underestimate eddy diffusivity (Panel C), leading in aggregate to

lower values than in the "no-slip" case. The convex shape near-the surface in the SELFE closures are still present, but are less severe and the near bed spikes are absent. Also, all profiles are now more symmetrical and thus, in that sense, closer to the analytical solution. The *k-ε* closures produce the largest diffusivities, with the SELFE native implementation leading to the largest maximum value, but the GOTM implementation most closely aligns with the analytical solution. For TKE (Panel D), the artificial near-bottom spikes are eliminated for GOTM closures and substantially reduced for SELFE implementations. Estimates of SSC (Panel B) are lower than those predicted in the "no-slip" case, which is attributed to the elimination or reduction of artificial near-bed TKE spikes.

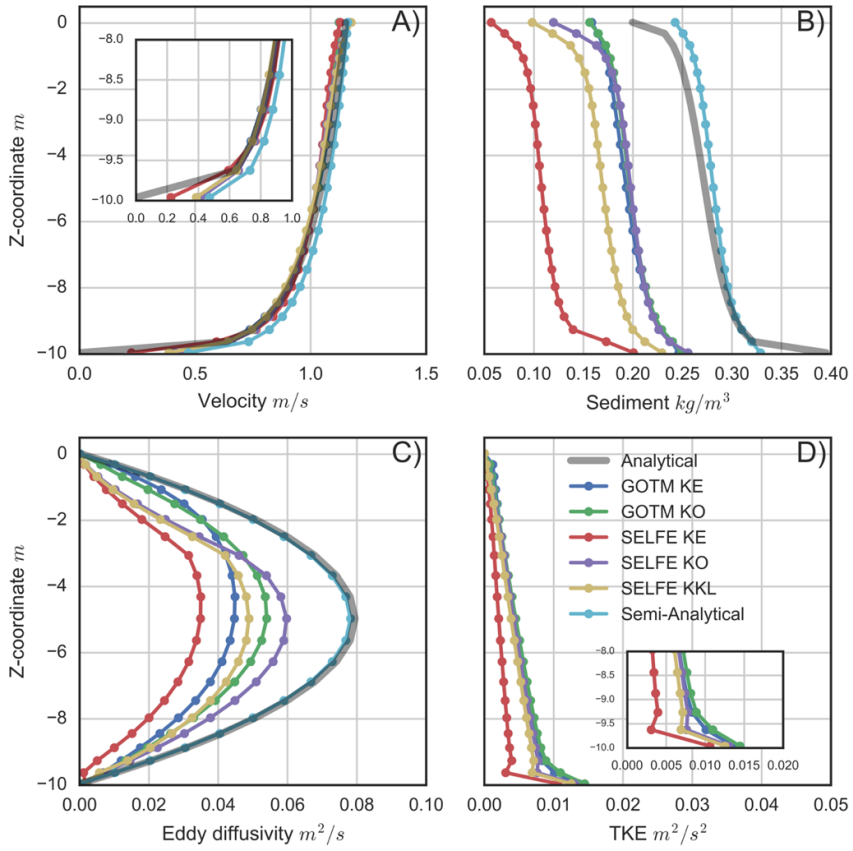

Figure 4 Profiles of model results from the open channel case with a slip bottom boundary condition. Velocity (A), suspended sediment (B), eddy diffusivity (C), and TKE (D).

Comparisons of bottom shear stress (used to calculate erosion), erosion rate, eddy diffusivity, and SSC are shown in Table 2. These results show that skill of SSC requires accurate predictions of eddy diffusivity and is less sensitive to deviations in bottom shear stress. The SELFE GLS implementations produce higher values of eddy diffusivity and, therefore, SSC, but at the cost of producing physically questionable profiles of eddy diffusivity and TKE. In contrast, the GOTM implementation predicts lower values of eddy diffusivity with smooth profiles that better match the shape of the semi-analytical and analytical solution. Given these tradeoffs, we believe that the combined used of the "slip" bottom boundary and GOTM for turbulence closure is the superior choice. We also note that this test highlights the inherent sensitivity of sediment models to model parameterization and numerical implementation, even in highly constrained tests.

Table 2 Description of turbulence closure models used for open channel test case and relevant values for bottom shear stress (τ_b [Pa]), erosional flux (kg/m^2/s), eddy diffusivity (Kh [m^2/s]), and suspended sediment concentrations (SSC [kg/m^3]) taken at one vertical level above the bed.

BBL	Turbulence model	Stability function	τ_b	Erosion	Kh	SSC
No-slip	Calculated Kh & Km	-	3.9062	3.856-e04	0.0104	0.314
No-slip	GOTM K-ε	Canuto-A	2.6797	2.630e-04	0.0092	0.244
No-slip	GOTM K-O	Canuto-A	2.0795	2.029e-04	0.0044	0.214
No-slip	SELFE K-ε	Kantha-Clayson	3.3842	3.334e-04	0.0202	0.294
No-slip	SELFE K-O	Kantha-Clayson	2.8742	2.824e-04	0.0057	0.250
No-slip	SELFE K-KL	Kantha-Clayson	2.9958	2.946e-04	0.0076	0.269
No-slip	Imposed Kh & Km	-	3.7955	3.745e-04	0.0102	0.321
Slip	GOTM K-ε	Canuto-A	3.6835	3.634e-04	0.0069	0.239
Slip	GOTM K-O	Canuto-A	3.9016	3.852e-04	0.0073	0.240
Slip	SELFE K-ε	Kantha-Clayson	3.1728	3.123e-04	0.0011	0.173
Slip	SELFE K-O	Kantha-Clayson	3.8474	3.847e-04	0.0069	0.237
Slip	SELFE K-KL	Kantha-Clayson	3.7432	3.693e-04	0.0059	0.212
Slip	Imposed Kh & Km	-	4.8309	4.781e-04	0.0102	0.320

2.3.2 Bed dynamics: Trench migration

This test is used to validate the implementation of suspended sediment, bed load, and morphology algorithms and is based on the flume experiments described in (van Rijn, 1993). The domain is an open channel (L = 30 m, W = 5 m) with a constant slope of 4.0 x 10^{-4} m m^{-1} featuring a trench cut into the bed. The bed and suspended sediments are comprised of a single non-cohesive class D_{50} = 0.16 mm with the settling velocity derived from the Stokes settling velocity and imposed as a constant value (w_s = 11 mm s^{-1}). The upstream hydrodynamic boundary condition consists of a constant velocity and depth (h_0 = 0.39 m, u_0 = 0.51 m s^{-1}) and suspended sediments are supplied upstream at a constant concentration of 0.14 kg m^{-3} to ameliorate erosion. The model hydrodynamics and suspended sediment are spun up with a fixed bed until the currents and SSC reach a steady state after ~25 minutes. The morphological algorithms are then enabled and the simulation proceeds for 15 h more. A global time step of 0.375 s, corresponding to a CFL (Courant-Friedrichs-Lewy) number of 1.5, was used based on sensitivity analysis (not shown) and is 7.5 times longer than the used in *Pinto et al.* (2012). The parameters were derived from sensitivity analysis to match observations of velocity and suspended sediment as described in *van Rijn* (1986) and to alleviate bed erosion upstream of the trench. We ultimately retained an erosion rate of 0.7 x 10^{-2} kg m^{-2} s^{-1}, compared to the rate of 1.6 x 10^{-2} kg m^{-2} s^{-1} used in *Pinto et al.* (2012), which produced excessive erosion and trench migration in our simulations. A summary of the model parameters is provided in Table 3.

Table 3 Model parameters for trench migration test.

Parameter	Variables	Values
H-Grid	# nodes, # elems	1205, 1920
V-Grid	# S-levels	30
V-Grid	H_c, θ_b, θ_f	7.0, 1.0, 10.0
Time step	dt [s]	0.375
Bottom roughness	Z_{ob} [m]	0.00`5
Initial density profile	[dp/dz]	0
Simulation length	[hours]	15
Settling velocity	w_s [mm/s]	11
Erosion rate	E_o [kg/m^2/s]	0.7 x 10^{-2}
Critical stress	τ_{ce} [N/m^2]	0.11
Porosity	Φ	0.4
Bed slope	S_o	4 x 10^{-4}
Horizontal boundary condition	$\overline{\boldsymbol{u}}$ [m/s]	0.51

Comparisons of profiles of suspended sediment and velocity between estimates of laboratory observations (markers, *van Rijn* (1986)) and model results (lines) are shown in Figure 5. Model profiles of velocity match observations most closely outside of the trench where a clear logarithmic profile is found in both the observations and model results. Stations within the trench show both slight overprediction and underprediction of velocity within a single profile, but are close to observations in magnitude. Profiles of SSC align with observations but have worse skill than the velocity profiles. In particular, the modeled SSC profiles underestimate concentrations near the bed. The underprediction of SSC is likely due to do a combination of underpredicted erosion and eddy diffusivity, as seen in the open channel case. Increasing the erosion rate yields increased SSC but

produces excessive erosion and trench migration. The velocity and SSC skill appears to lag those produced by ROMS (Warner et al., 2008) and Delft3D (Lesser et al., 2004), but are similar to the results in Pinto et al. (2012). The trench migration is very similar to observations and aligns with the previously published results of *Pinto et al.* (2012) and *Warner et al.* (2008) despite using different parameters for erosion rate and critical stress. Skill scores for the trench migration case are shown in Table 4. The difference in the predicted final position of the trench results from underprediction of SSC and likely from underprediction of bedload transport.

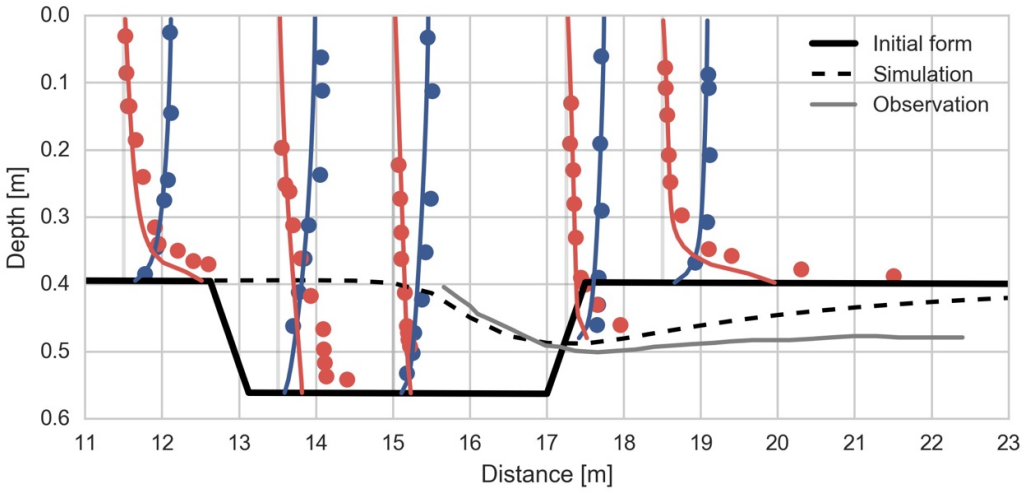

Figure 5 Velocity (blue) and suspended sediment (red) profiles comparing observations (circle markers) with model results (lines). Also depicted are measured and calculated bathymetric profiles of the migrating trench test case.

Calibration simulations (not shown) confirm that the model is very sensitive to erosion rate parameterizations and must be carefully tuned to ensure that the SSC profiles align with observations. As in the open channel case in Section 2.3.1, this highlights the inherent uncertainty in sediment models in even highly constrained cases. However, the trench and open channel cases differ in some important respects. In particular, the calculated TKE in the upstream section of the trench

does not exhibit the near-bed spike as seen in the open channel case, regardless of whether GOTM or SELFE are used for turbulence closure. Additionally, the GOTM eddy diffusivity deviates from a smooth profile near the surface, whereas the SELFE profile is very similar to that found in the open channel case (Figure 6). This likely results from the much higher vertical resolution used in this shallow test case (30 vertical levels in 0.4 m) compared to the open channel case (21 vertical levels in 10 m) which is more representative of the resolution used in realistic scenarios.

Table 4 Model skill for predicted bed depth in the trench migration case.

Variable	Bias	Corr	WS	BSS	RMSE
Bed depth	-0.02	0.41	0.54	0.84	0.02

Another difference is that, unlike in the open channel case (Section 2.3.1), trench migration results are largely insensitive to the selection of turbulence closure, but quite sensitive to the bottom boundary treatment (results not shown). This is because of the dominance of bed dynamics in the trench case whereas the open channel case lacks morphological evolution. Because the erosional flux is determined by near-bed velocities, changes in the treatment of the bottom boundary layer produce proportional changes in the bed evolution. This suggests that accurate simulation of near-bed velocities and bed properties are more important than turbulence closure in systems dominated by bed interactions.

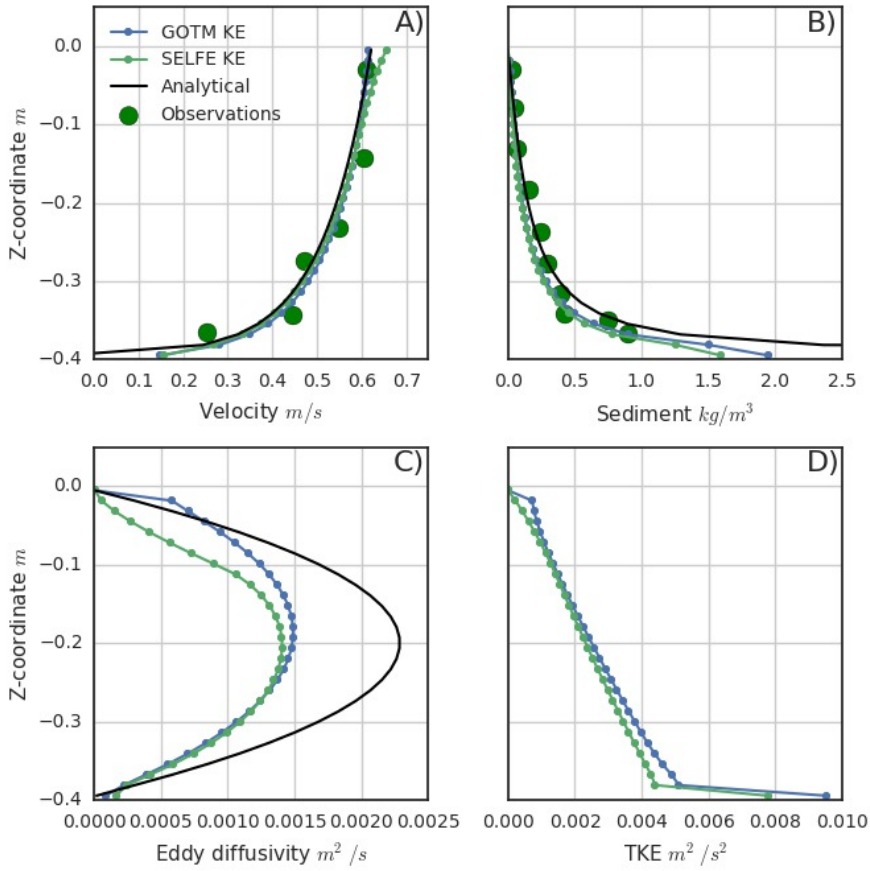

Figure 6 Profiles of model results from the trench migration case with a slip bottom boundary condition taken at the first observation station in the upstream portion of the domain at the end of the spin-up period. Results show for GOTM (blue) and SELFE (green) implementations of GLS equations. Velocity (A), suspended sediment (B), eddy diffusivity (C), and TKE (D).

2.3.3 ETM dynamics: Idealized channel

This test is used to assess the ability of the sediment model to represent processes associated with the generation of an estuarine turbidity maximum (ETM). The test is derived from *Burchard & Baumert* (1998) and *Warner et al.* (2007), who used variations of it to assess the importance of ETM related processes and to describe those processes over tidal time scales. The domain is effectively a two-dimensional open channel 100 km in length and 200 m in width. The domain features a constant sloping bottom starting with a 5 m depth at the upstream boundary and ending with a 10 m depth at the downstream boundary. The ocean boundary is forced with a semi-diurnal displacement of the free surface with an amplitude of

0.4 m and a period of 12 hours and the constant imposition of salinity at 30 psu and temperature at 10 C. The upstream boundary is forced with a constant flux of 80 m^3 s^{-1}, salinity of 0 psu, and temperature of 10 C. The hydrodynamics are allowed to spin-up for 14 days whereupon the initial conditions have been eliminated from the domain and a regular pattern of gravitational circulation has been established. We note that the solution to the problem is highly sensitive to the density forcing at the downstream boundary. Sensitivity tests (not shown) suggest that slight perturbations in the forcing results in both different spin-up period lengths and characteristics of the gravitational circulation patterns including salinity and SSC distribution.

Figure 7 shows tidally averaged salinity, SSC, and along-along channel velocity. The predicted representation of the salt wedge and sediment concentrations are very similar to those described in *Burchard & Baumert* (1998) and *Warner et al.* (2007). Specifically, the distribution of sediment in the channel can be divided into three distinct areas corresponding to the well-mixed upstream fluvial section, a stratified bottom boundary layer corresponding to the salt wedge, and a surface layer above the salt wedge. The well-mixed upstream section features residual downstream velocity and low SSC that steadily increases in proximity to the salt-wedge and the region of convergent currents. The highest velocities in the domain are found in the surface layer above the salt wedge where they are oriented downstream and contain the lowest SSC because the sediment tends to settle through the pycnocline into the salt wedge. Within the salt wedge, the residual velocities are oriented upstream carrying the highest concentrations of SSC in the system. Of particular interest, a localized region of elevated SSC occurs near the toe of the salt wedge, the classical ETM, due to trapping of sediment by the convergent

currents. Finally, the salt wedge region contains SSC above both the riverine and ocean end members sourced from a combination of sediment settling from the upper layer, erosion from the bed, and residual upstream transport.

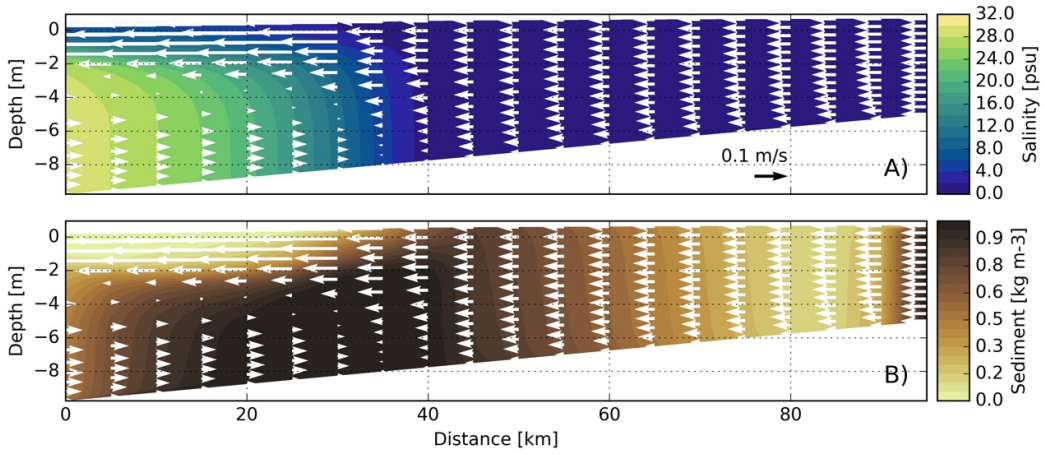

Figure 7 Transects of tidally averaged salinity and suspended sediment concentrations in an idealized 2D channel. Velocity profiles are shown with grey arrows. Three distinct regions are found corresponding to: 1) a fresh, low SSC upstream section; 2) a brackish, low SSC region with downstream focused velocity above the pycnocline; 3) a saline, high SSC section with upstream focused velocity.

While this test case lacks analytical solutions or reference observations, it remains a critical check of a model's ability to represent the coupled circulation and sediment dynamics required to generate elevated turbidity near the upstream limit of salt intrusion in estuaries. Qualitative comparisons with results described in literature (Burchard & Baumert, 1998, Warner et al., 2007) show that SELFE produces similar results for density, SSC dynamics, and magnitude and location of SSC peaks. These similarities suggest the model is capable of representing ETM dynamics, a common sedimentary feature in many tidally driven estuaries.

2.4 Columbia River benchmark

The Columbia River is the largest river to discharge into the North East Pacific Ocean. It has a mean discharge of 8,000 $m^3 s^{-1}$, with a minimum of ~3,000 $m^3 s^{-1}$

during dry autumnal months and over 15,000 $m^3 s^{-1}$ during large spring freshets. The estuary has two main channels separated by broad intertidal shoals and is flanked by four lateral bays (Figure 8). The South Channel receives the majority of the fluvial flux and is regularly dredged for navigation purposes. In contrast, the North Channel is not maintained for transport and receives the majority of the tidal prism (Chawla et al., 2008). The tides in this system are mixed, semi-diurnal with a tidal range that varies from ~2 m for the smallest neap tides to ~3.5 m during the largest spring tides.

2.4.1 Field observations

Two in-situ sensor networks provide nearly continuous observations for model-data comparisons (Figure 8). From the tidal gauge network of the National Oceanic and Atmospheric Administration, we use time series of elevations from the Tongue Point, OR station along the South Channel. From the Center for Coastal Margin Observation & Prediction interdisciplinary SATURN network (Baptista et al., 2015), we use temperature, salinity, and turbidity time series from stations SATURN-03 (in the South Channel) and SATURN-04 (in Cathlamet Bay).

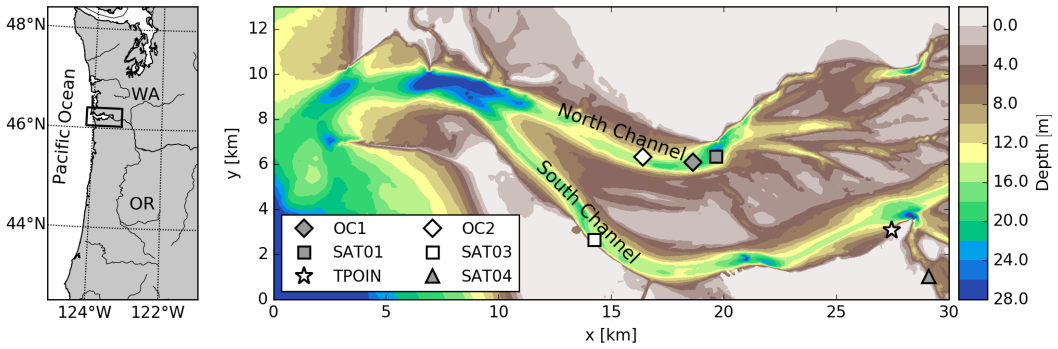

Figure 8 Map of the Columbia River estuary with stations and ship locations where data was collected.

In addition, we make model-data comparisons with a single-vessel research cruise that took place between October 25 and November 3, 2012, aimed at

characterizing ETM dynamics (Sanford et al., 2015). The cruise's geographic scope was the North Channel with anchorages at OC1 and OC2 (Figure 8). Vessel-based instrumentation included a boom mounted acoustic Doppler current profiler (ADCP), a conductivity temperature depth (CTD) package, a flow-through optical backscatter sensor (OBS), and the CMOP Winched Profiler (CMOP-WP). The CMOP-WP is a multi-instrument sensor package comprised of a Seabird SBE 37 CTD, WetLabs EcoPuck, a Sequoia LISST-1000X, Sea-bird μC and μT, and a Sontek acoustic Doppler velocimeter (ADV). Additional details about the CMOP-WP can be found in *Kärnä et al.* (2015). The CMOP-WP continuously profiled the water column for the duration of the cruises. Water samples were collected before, during, and after each passing of the ETM and were processed using the method described by *Reed & Donovan* (1994) using a modified Owen Tube to collected samples that were then filtered, dried, and weighed to determine the amount of suspended sediment. These data were combined with measurements of SSC from the USGS station at Beaver Army Terminal and turbidity measurements from the same instrument type at SATURN-05 (also located at Beaver Army Terminal) to create a predictive model of SSC from NTU measurements. A least squares fit of the observations (Figure 9) yielded the relation

$$SSC = 2.16 \cdot NTU^{1.26} \tag{11}$$

where SSC is the estimated suspended sediment concentration and NTU is the observed turbidity from the optical instrument ($R^2 = 0.76$).

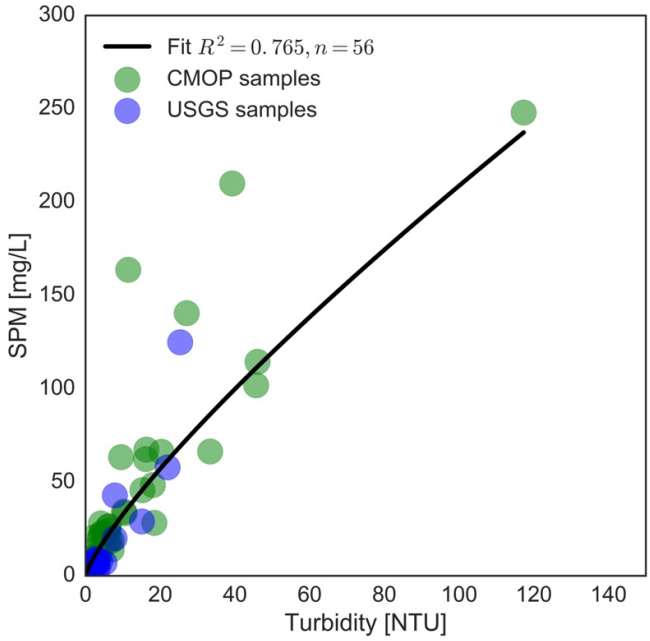

Figure 9 Observations of suspended sediment concentrations and optical turbidity measurements with the least squares fit the log-transformed data.

2.4.2 Model parameterizations

The application of SELFE to the Columbia River estuary benefits from the extensive prior history of sensitivity studies, model parameterization, and validation for SELFE-based circulation simulations in that system. In particular, we use the same numerical choices and hydrodynamic parametrization for SELFE described in *Kärnä et al.* (2015). The numerical methods used for this application are the same as those described in Section 2.2.1. A second-order k-ε model from GOTM is used for turbulence closure which has shown to maximize salinity retention in the estuary in sensitivity studies (not shown). An optimal global time step of 36 s was derived from sensitivity studies, with the time step for the transport equations sub-iterated to avoid CFL violations. River discharge and temperature boundary conditions are imposed at Beaver Army Terminal from observations (USGS #14246900). The top eight tidal constituents from a regional inverse model

(Myers & Baptista, 2001) are imposed along the ocean boundary. Temperature, salinity, and sub-tidal elevations are imposed along the same boundary from Navy Coastal Ocean Model (NCOM) simulations (Barron et al., 2006). In a buffer region (50 km) near the ocean boundary, temperature and salinity fields are nudged toward NCOM values on a time scale of two days. Atmospheric boundary conditions of wind speed, air pressure, and radiative heat flux are forced from the NOAA/NCEP North American Mesoscale Forecast System (Rogers et al., 2009).

Table 5 Sediment model parameters used for simulations of the Columbia River estuary for the simulation in October 2012.

Variable	Wash	Fine Silt	Silt	Sand
Median diameter [mm]	0.01	0.03	0.06	0.125
Settling velocity [mm/s]	0.05	0.05	2.0	10.0
Erosion rate [kg/m^2/s]	1.0 x 10-5	1.0 x 10-4	1.0 x 10-4	1.0 x 10-3
Critical stress [Pa]	0.10	0.15	0.15	0.2
Porosity	0.65	0.60	0.55	0.50
Bed initial conditions [%}	0.05	0.10	0.10	0.75
Boundary conditions [%]	0.05	0.10	0.10	0.75

The horizontal mesh (56K 2D nodes, 109K 2D elements) covers the Columbia River estuary from Beaver Army Terminal 85 km upstream of the mouth through the continental shelf to 300 km off the coast from latitudes 39N to 50N. The domain is highly resolved in the estuary and more coarsely represented in the plume and far-field ocean. The domain includes the river-to-shelf continuum to capture the effects of shelf-scale processes such as upwelling and plume dynamics on estuarine circulation. The flexibility provided by the unstructured mesh used by SELFE is ideally suited to represent fine structures within the estuary, the complicated coastline within and outside of the estuary, and the winding main

channel to the first convenient boundary condition at Beaver Army Terminal. The vertical structure is resolved using 37 stretched S-levels (H_c=30, θ_b=0.7, θ_f=10) in most of the domain with an additional 17 Z-levels in stretches deeper than 100 m. Bottom roughness is imposed with a uniform Z_0 of 0.0001 m, based on calibration runs to optimize model representation of salinity (Kärnä et al., 2015).

The sediment model is parameterized from a combination of observations, literature values, and a set of subsequent calibration simulations (not shown). We use four sediment classes with settling velocities of 0.05, 0.5, 2.0, and 10.0 mm s^{-1} which are representative of the suspended sediment size classes found in the Columbia River estuary (Fain et al., 2001). These classes range from silts to fine sands with details related to median size and settling speed described in Table 5. The initial bed distributions are derived from literature descriptions of the system and are dominated by the sand size class because the bed is almost completely devoid of clay or fluid mud (Fox, et al. 1984; Fain et al., 2001; Sherwood & Creager, 1990). The riverine boundary conditions for sediment concentrations are derived from a rating curve derived from water samples of suspended sediments at Beaver Army Terminal (USGS #14246900). Water samples of SSC and mean daily flow were log-transformed and fit using a least squares method following the methods described in *Warrick* (2014), yielding the relation

$$SSC = e^{-18.6} Q_r^{1.65} \tag{12}$$

where Q_r is the river flux (m^3 s^{-1}) and SSC is suspended sediment (mg L^{-1}) (R^2=0.79). The rating curve predicts SSC concentrations of 0.005 - 0.022 kg m^{-3} for the modeled time period, comparing adequately with available observations of 0.01 - 0.02 kg m^{-3}. The ocean boundary conditions are derived from oceanic (> 30

psu) water samples collected during the cruise described in Section 2.4.1 and were imposed as a constant 0.005 kg m^{-3}. Erosion rate, critical shear stress, and porosity are all derived from literature values for similar size classes (Ralston et al., 2013; Warner et al., 2008) from systems with similarities in sediment composition and characteristics. Erosion rate and critical shear were then calibrated (not shown) using model skill at SATURN stations and anchorages OC1 and OC2 as the metric.

2.4.3 SATURN station comparisons

In this section we compare model results to observations of temperature, salinity, and turbidity measurements at SATURN-03 and SATURN-04, and of elevation at Tongue Point, OR. Estimates of SSC are obtained from an empirical correlation (Equation (**12**)) between water samples from research cruises and stations (USGS #14246900) and optical turbidity measurements (Figure 9).

SATURN-03 is located in the South Channel approximately 23 km upstream of the mouth. Located within the extent of salinity intrusion, this station captures the estuary's strong variability in response to tidal and river forcing. The station is equipped with a pump-based system where water is collected at ports 2.4, 8.2, and 13 m below Mean Sea Level (MSL) in sequence, and piped to a single instrument package where salinity and turbidity are measured. In-water temperature sensors are collocated with each port.

Observations at this station show that the highest SSC occur during spring tides and the lowest during neap tides. The correlation between tidal range and SSC is strongest near the bed and diminishes toward the surface where average SSC and the tidal variability of SSC decrease. The observed SSC is also strongly correlated

with semi-diurnal tidal patterns: the highest concentrations within a tidal day occur during the floods immediately following large ebbs. Model results qualitatively capture tidal day and tidal month patterns of variability as suggested by the average correlation coefficient for the station, Corr = 0.52 (Table 6). The average Willmott Score, WS = 0.64, suggests good skill, but the more rigorous Murphy Score indicates skill worse than the observed mean (MS= -0.91). The simulated tidally averaged SSC also reveal a correlation with tidal range, which observations for this time period also suggest.

Table 6 Model skill from R/V Oceanus anchorages OC1 and OC2 data collected by the Winched Profiler and SATURN-03 at 2.4 m (S), 8.2 m (M), and 13 m (B) depths.

Site	Variable	Bias	Corr	WS	MS	RMSE
OC1	Velocity	-0.13	0.95	0.96	0.77	0.37
OC1	Salt	-3.95	0.87	0.89	0.46	6.64
OC1	Temp	0.17	0.69	0.69	0.25	0.35
OC1	SSC	0.01	0.16	0.41	-0.72	0.02
OC2	Velocity	-0.15	0.96	0.97	0.87	0.32
OC2	Salt	-1.20	0.92	0.95	0.80	4.59
OC2	Temp	0.17	0.67	0.69	0.26	0.54
OC2	SSC	0.02	0.69	0.57	-4.06	0.02
SATURN-03 S	Salt	-1.583	0.947	0.956	0.788	3.426
SATURN-03 M	Salt	0.054	0.961	0.979	0.912	2.386
SATURN-03 B	Salt	-2.185	0.858	0.882	0.504	3.499
SATURN-03 S	Temp	-0.116	0.735	0.844	0.434	0.510
SATURN-03 M	Temp	-0.9097	0.711	0.830	0.452	0.503
SATURN-03 B	Temp	0.143	0.664	0.798	0.361	0.487
SATURN-03 S	SSC	0.002	0.537	0.664	-1.042	0.008
SATURN-03 M	SSC	0.004	0.458	0.609	-1.114	0.011
SATURN-03 B	SSC	0.007	0.554	0.646	-0.808	0.012

SATURN-04 is located near the entrance of Cathlamet Bay south of the South Channel just upstream of Tongue Point. This station remains largely fresh throughout the year, but periodic pulses of brackish water are observed during periods of low and moderate river discharges. Structurally similar to SATURN-03, this station collects data at 0.3 m below the water surface and 8.6 m below MSL. Model skill for SATURN stations is summarized in Table 6.

Fouling of the turbidity sensor limited data availability during the targeted time period. Despite this, Figure 10 shows that available measurements provide context, offer a rough estimate of SSC, and to enable a rough assessment of the model skill in an unstratified region of the estuary. Model results are similar in magnitude to observations and suggest that SSC is lower at this station than at SATURN-03 or at the locations profiled by the CMOP-WP (Section 2.4.4). Model results also suggest reduced spring-neap variability compared to SATURN-03. The comparatively lower values of SSC observed and predicted by the model are consistent with SATURN-04 lying outside the ETM region.

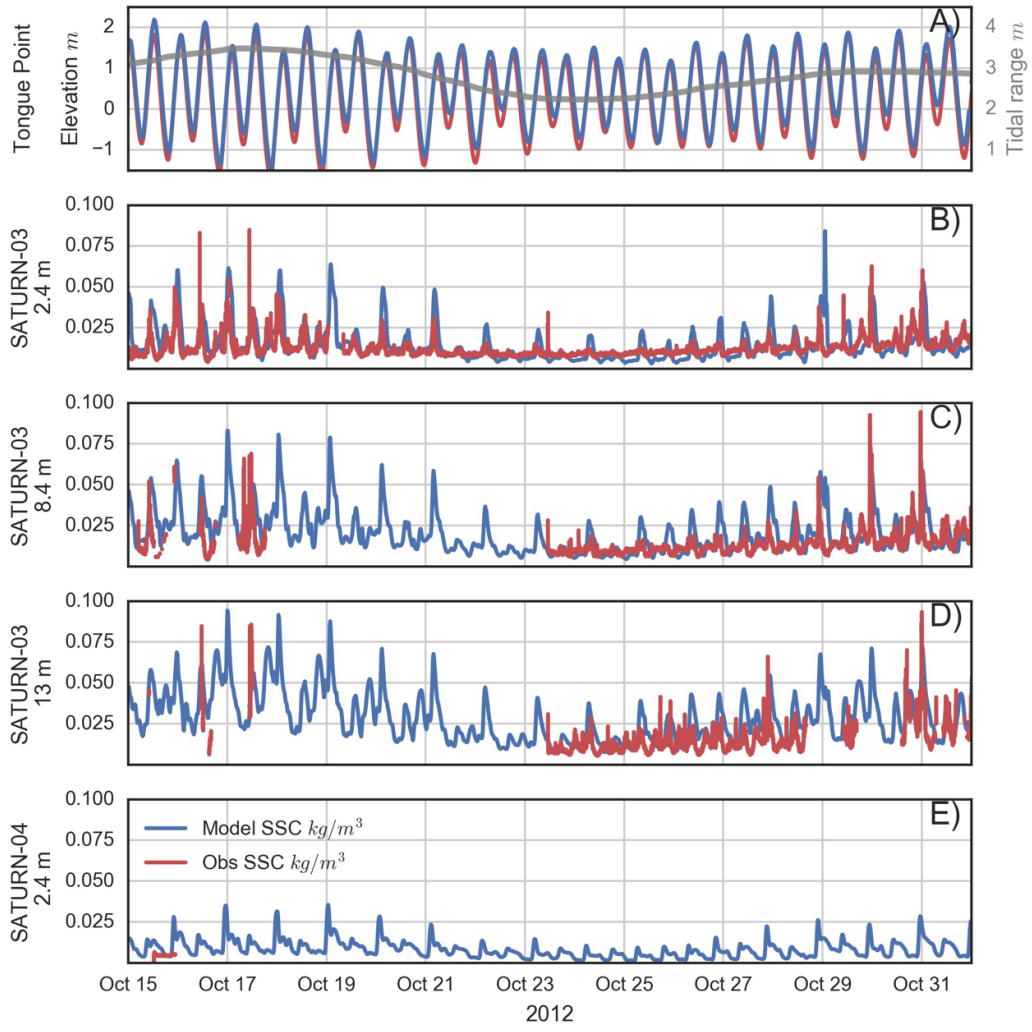

Figure 10 The figure shows a comparison of predicted suspended sediment concentrations at SATURN stations at multiple depths compared against feature observations. Shown are elevation (black) and tidal range (gray) observations from Tongue Point, Oregon (A), model (blue) and observations (red) of SSC at depths of 2.4 m (B), 8.4 m (C), and 13.0 m (D) at SATURN-03, and 0.4 m depth at SATURN-04 (E).

2.4.4 Winched Profiler comparisons

Here we compare model results to the shipborne observations in the North Channel as captured by the CMOP-WP during the fall 2012 cruise (Figure 8). Specifically, we compare temperature, salinity, velocity, and SSC values as measured by the CMOP-WP and model results using the statistical metrics described in Section 2.2.3 (Table 6).

2.4.4.1 Flow field comparisons

The skill of the circulation model has been described in detail in *Kärnä et al.* (2015), but the pertinent points are summarized here for context. Model skill at OC1 (Figure 11) and OC2 (Figure 12) has been calculated separately and is summarized in Table 6. Model skill at OC1, during the transition from neap to spring tides, lags that at OC2, during spring tides, according to all skill metrics except for the MS. Qualitatively, the overprediction of SSC at OC2 (MS = -4.06, WS = 0.57) makes the model results appear to have less skill than those at OC1 (MS = -0.72, WS = 0.41).

At OC1 the shape of the salt wedge and salinity distribution of the major floods is well represented by the model (Figure 11). In both the model and observations, salinities associated with the salt wedge over 20 psu are present in the surface layer and salinities over 30 psu are found in the lower layer. Model skill for all fields diminishes during ebbs, when the model underestimates the retention of salt near the bed, the presence of two distinct layers, and the setup of exchange flow as documented in *Kärnä et al.* (2015). The lack of a two-layer representation at OC1 during ebbs results in an overestimate of seaward velocities throughout the water column, but is most prominent near the bed and is reflected in the bias (-0.13 m/s). Nevertheless, the model captures the tidal variability of along-channel velocities according to all skill metrics (MS=0.77, WS=0.96). Model skill of salinity (MS=0.46, WS=0.89) lags that of velocity due to the underprediction of salinity during ebbs.

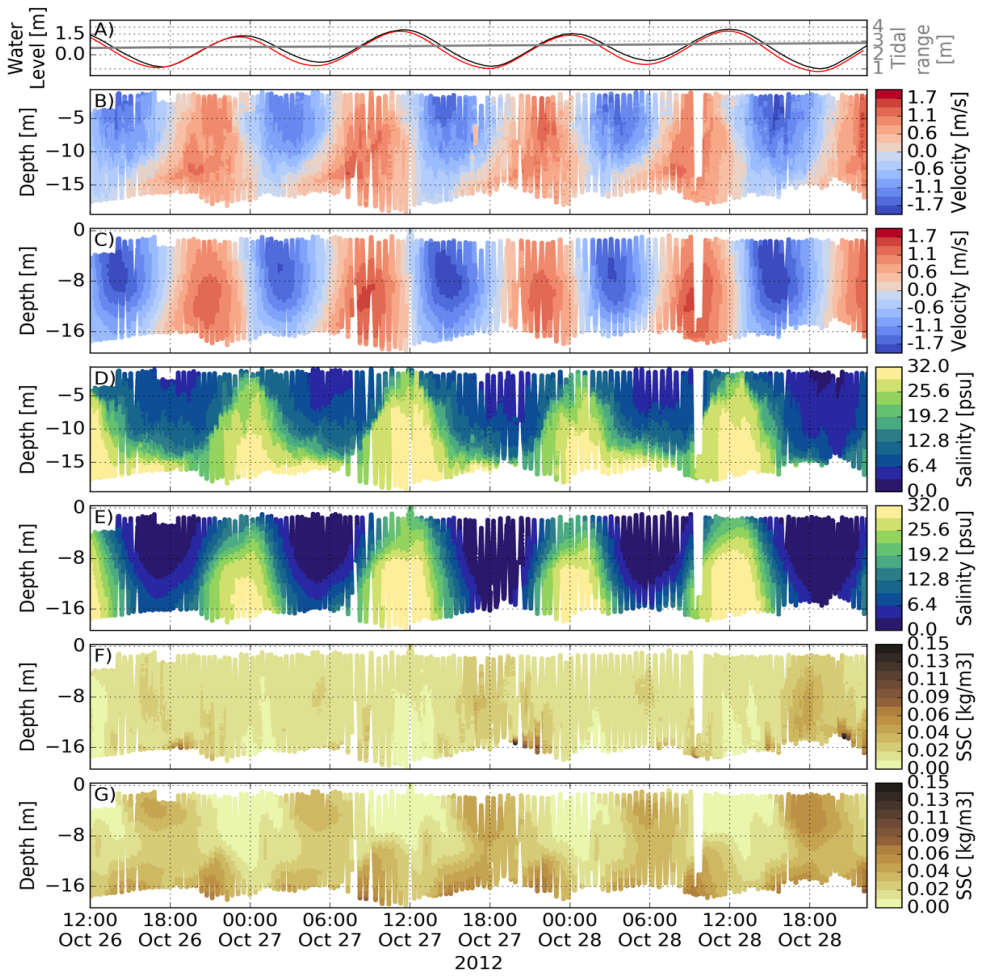

Figure 11 Comparisons of observations and model results at anchorage OC1 from the Winched Profiler for water levels (A), stream-wise velocity (B), modeled stream-wise velocity (C), salinity (D), modeled salinity (E), SSC (F), and modeled SSC (G). The gray line in (A) is the tidal range for the observation period.

At OC2 the model skill is highest during flood and degrades during major ebbs, as was the case at OC1 (Figure 12). For example, the model shows the salt wedge being advected downstream of the station during the major ebb between 10:00 and 18:00 on Oct. 29 leaving the water column nearly fresh. In contrast, observations show that the salt wedge remained at OC2 and that the water column remained stratified. The lack of salinity retention is reflected in the bias (-1.2 psu),

but is not apparent in other metrics (MS=0.80, WS=0.95). In both the observations and model results, the fastest upstream velocities are localized to a region within the pycnocline during minor floods but produce nearly uniform velocities over the entire water column during major floods. The under-predicted salinity intrusion is reflected in the negative bias of the along channel currents (-0.15 m/s), but other skill metrics suggest good overall skill (MS=0.87, WS=0.97).

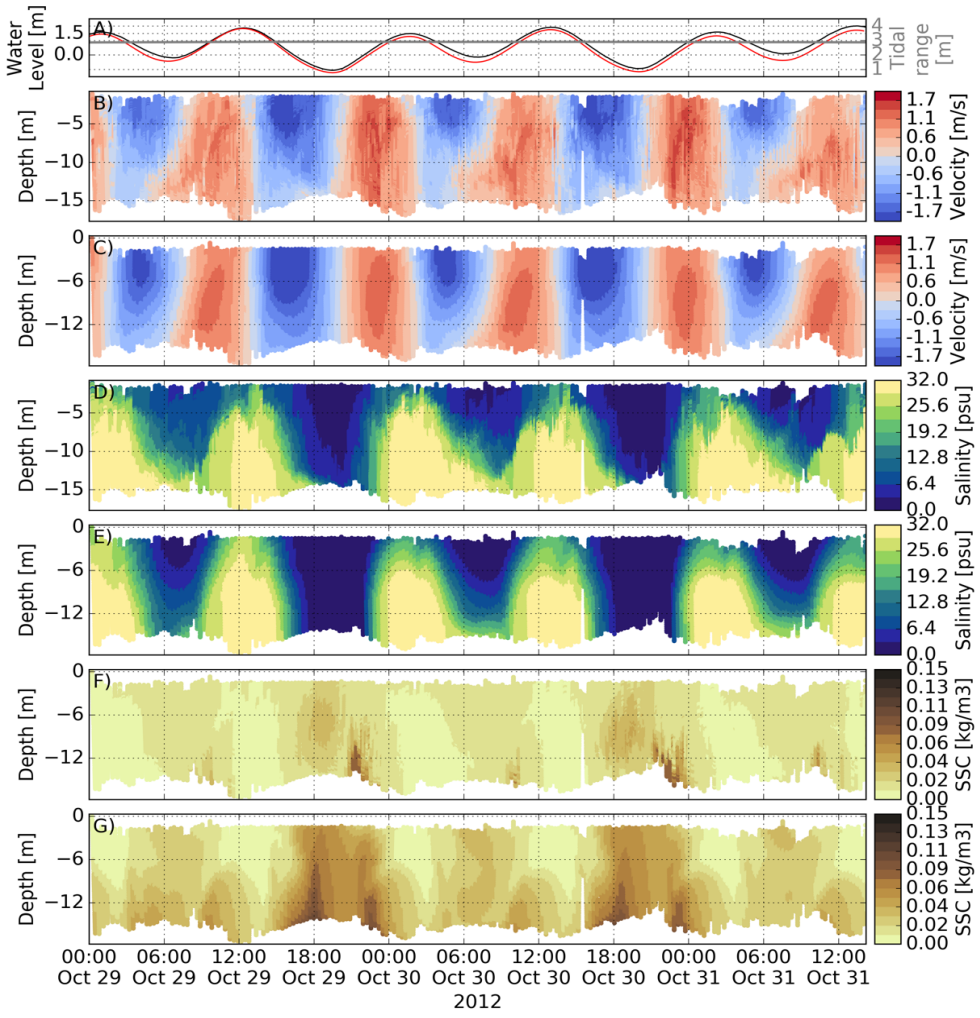

Figure 12 Comparisons of observations and model results at anchorage OC2 from the Winched Profiler for water levels (A), stream-wise velocity (B), modeled stream-wise velocity (C), salinity (D), modeled salinity (E), SSC (F), and modeled SSC (G). The gray line in (A) is the tidal range.

2.4.4.2 Suspended sediment comparisons

A few essential features characterize the observed sediment dynamics observed at OC1 (Figure 11) and OC2 (Figure 12). The lowest SSC are found in high-salinity waters in the salt wedge representative of sediment concentrations of the adjacent coastal area. The highest concentrations of SSC are found near the bed during floods and are associated with ETM dynamics. The concentration of SSC in the flood ETM is dependent on the semi-diurnal tidal range and the change in water elevation during the preceding ebb. During ebbs when the water column remains stratified, a patch of elevated SSC advects over the salt wedge. Concentrations in this patch are correlated with the change in water level during the ebb.

At OC1 the model captures the variability of SSC over the semi-diurnal tidal cycle and represents the salient SSC features described above. Model predicted SSC is lowest in the salt wedge and fresh waters aligning with observations (Figure 11). The dominant SSC feature is a bottom-focused flood ETM increasing in concentration as the tidal range grows following the same pattern found in observations (Figure 11 - See Oct. 26 15:00, Oct. 27 3:00, and Oct. 28 15:00). During ebbs, the near surface SSC concentrations are greater than those below the pycnocline indicating the advection of a patch of sediment over the salt wedge as seen in observations. During large ebbs the model predicts a bottom-focused ebbing ETM trailing the salt wedge. Observations show that the water column remained more stratified than the model suggests and with the highest SSC found in a patch above the pycnocline. Despite representing all of the prominent SSC features at OC1, the model MS is negative (-0.72) suggesting that it has less predictive ability than the mean of observations, whereas other metrics suggest poor (Corr = 0.16) and moderate skill (WS = 0.41) (Table 6).

Model results at OC2 are similar to those at OC1, capturing observed trends well during floods, but less so during major ebbs (Figure 12). As at OC1, the discrepancy between simulations and observations results from the under-prediction of salinity intrusion and retention and the over-prediction of ebbing currents. Under-prediction of salinity intrusion and retention during ebbs leads to the model predicting an ebb ETM (e.g. Oct. 29 10:00 - 18:00). However, observations show that the water column remained stratified and a patch of elevated suspended sediment concentrations passed over the salt-wedge. As at OC1, the effects of ebb tide substantially degrade the MS (-4.06) indicating poor skill, whereas other metrics indicated moderate skill (Corr = 0.69, WS=0.57) (Table 6).

2.4.4.3 Computational performance

We provide performance metrics of SELFE in terms of strong-scaling and time to solution for problem sizes similar to those used for this study to provide an estimate of the computational cost. The location and problem size is site specific, but provides useful insight into performance for this class of model for a realistic application.

We compare the strong-scaling performance of a previous version of the model (SELFE v3.1) documented to lack scalability (Kerr et al., 2013) and the current version (SELFE v4.0) which includes a new treatment for the linear solve for continuity and atmospheric boundary conditions. In this test we run the base hydrodynamics including temperature and salinity, but no additional tracers, on the National Energy Research Scientific Computing Center (NERSC) Edison cluster, a Cray XC30. The mesh (~89K 2D, ~4.5M 3D elements) and model parameters are realistic for a scientifically meaningful representation of estuarine circulation in

the Columbia River estuary and are described in Section 2.4.2 and Table 5. The model is run for 12 simulated hours from a spun-up hotstart state derived from a hindcast simulation. The mean timings for the test on the NERSC Edison system are reported in Table 7. SELFE v3.1 scales nearly linearly up to 64 processes where it then diverges reaching the fastest time to solution using 256 processes (Figure 13). This same limit has been found on larger grids internally and by other researchers (Kerr et al., 2013). In contrast, SELFE v4.0 scales nearly linearly to 128 processes where it begins to diverge, but continues to scale sub-linearly to 1024 processes. Use of 1024 processes is close to the upper bound of the number of processes that can be used for this problem size.

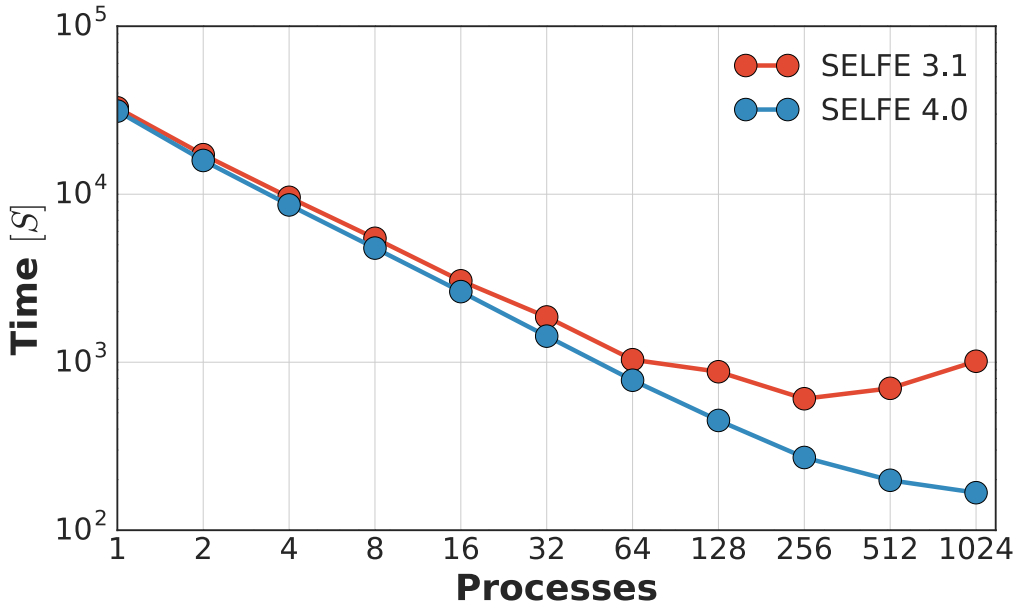

Figure 13 Comparison of strong-scaling of SELFE before computational improvements (SELFE v3.1) and after (SELFE v4.0) using a realistic domain with ~89K nodes and ~4.5 M 3D prisms on the NERSC Edison system. Use of 1024 processes is near the limit of domain decomposition for this problem size.

Comparing the time to solution between SELFE v3.1 and SELFE 4.0, we use the

same grid model parameters as those in strong scaling test (Table 7). Two of the tests include the addition of four passive tracers which act as a proxy for sediment model simulations. Ideally we would have compared the performance using four sediment classes, but the sediment model in SELFE v3.1 was unstable and simulations would not complete. Focusing first on the results using 128 processes, we note that for purely hydro-dynamic simulations (S1 versus S3), SELFE v4.0 is twice as fast as SELFE v3.1. However, for simulations with passive tracers (S4 versus S5), SELFE v4.0 is 4 times as fast. Adding tracers slows the simulations by factor of two (S2 versus S4) for SELFE v4.0, and ≈ 3.4 times as slow for SELFE v3.1 (S1 versus S4).

Table 7 Performance comparison before performance enhancements for SELFE v3.1 (3.1) and after enhancements SELFE v4.0 (4.0) for a realistic hindcast simulation of the Columbia River system. *Total time* refers to wall-clock time for the entire simulation and *Time per day* refers to the wall-clock time per simulated day.

Test	Number of simulated days	Version	Tracers	Number of processes	Total time [minutes]	Time per day [minutes]
S1	14	3.1	T, S	128	534	38
S2	14	4.0	T, S	128	271	19
S3	14	4.0	T, S	1024	92	6
S4	2	3.1	T, S, 4 tracers	128	262	131
S5	2	4.0	T, S, 4 tracers	128	67	32

2.5 Discussion

2.5.1 Idealized tests and implications

We have shown that the SELFE sediment module represents analytical solutions, laboratory data or expected behaviors in a suite of idealized test cases, with a skill qualitatively similar to other published results, but lags the skill of the higher-

order ROMS and Delft3D model in specific tests (Burchard et al., 2003; Lesser et al., 2004; Warner et al., 2008; Pinto et al., 2012).

The open channel test isolates suspended sediment dynamics in an unstratified flow by neglecting bed load transport and morphology. Model results show high sensitivity of SSC to the selection and implementation of the turbulence closure model. The native SELFE implementation of the GLS equations produce spikes in TKE near the bed and a convex profile of eddy diffusivity near the surface when the "no-slip" boundary condition is used for the momentum equation. The same characteristics are not reproduced when using the online coupled GOTM implementation of the GLS suggesting that the differences lie in the numerics and implementation for the GLS equations. As shown in previous work (Pinto et al., 2012; Warner et al., 2008) use of the GLS turbulence closure universally results in underprediction of suspended sediment against a semi-analytical solution assuming a Rouse profile. The analytical Rouse solution significantly under-predicts SSC in the upper water column compared to the semi-analytical solution highlighting uncertainty in the real behavior of sediments. The difference between these solutions is caused by model specific details of numerics and implementation, in addition to the inherent uncertainty associated with the Rouse profile. *Violeau et al.* (2002) found a similar spread in solutions when comparing numerical solutions using different models.

In contrast to the open channel case, the trench migration incorporates suspended sediment, bed load transport, and morphological processes in an unstratified flow. Despite the bed properties being tightly constrained by the parameters stipulated in the flume test, numerical results required extensive sensitivity tests for bottom roughness, critical stress, and erosion rate. The first difficulty encountered was

optimizing the bottom roughness and time step for velocity. Attempts at using the same time step and grid resolution as specified in *Warner et al.*, (2008) and *Pinto et al.*, (2012) resulted in poor representation of velocity. Sensitivity analysis of time step resulted in an optimal time step of 0.375 s compared to 0.05 s used in *Pinto et al.*, (2012). Despite this optimization, qualitative comparisons of velocity profiles between SELFE and ROMS (Warner et al., 2008) and Delft3D (Lesser et al., 2004) suggest that the lower-order SELFE is not as skilled at representing horizontal velocity, particularly within the trench. The effects of the deviation between observed and modeled velocity on SSC are evident in at stations 2, 3, 4. Comparisons between predicted trench migration and observations suggest that SELFE is representing bed load transport and morphodynamics reasonably well. The location of the trench entrance and maximum depth is similar to observations, but the exit of the trench shows a gradual incline not seen in observations as shown in other tests (Lesser et al., 2004; Warner et al., 2008; Pinto et al., 2012). Unlike the open channel case, the SSC and migration of the channel is much less dependent on the selection of the turbulence closure model because interactions between the bed and suspended sediment dominate the variability induced by differing representations of vertical mixing. The implication is that sediment modeling in realistic environments is likely to be dominated by bed dynamics and not selection of turbulence closure. Model skill for the bed, as measure by quantitative error metrics, is poor despite good qualitative agreement. This suggests that: traditional metrics of skill are inadequate to assess the ability of a model to capture sediment related processes and sediment model skill lags that of hydrodynamics.

The idealized tidal estuary with stratification is a critical test of the predictive skill

of estuarine sediment models. A number of studies have shown that density effects substantially alter sediment transport and assessing the ability of a model to represent these interactions is critical in stratified regions (Burchard & Flöser, 2008; Elias et al., 2012). Sensitivity analysis to the imposition of boundary conditions for density suggest a broad solution space, most of which do not result in a stable, periodic solution as has been described in previous studies (Warner et al., 2008). While the model is able to reproduce estuarine circulation and sediment dynamics that adhere to conceptual understanding and theory (K.R. Dyer, 1973), there is no means of quantifying the results although comparison with other published results suggest qualitative agreement (Burchard et al., 2003; Warner et al., 2008). The lack of laboratory observations for a similar test case represents a critical research gap.

2.5.2 Model skill in realistic scenario and limitations

Application of the model to a realistic hindcast scenario reveals that the sediment model is capable of representing sediment dynamics detailed by field instrumentation when optimized for skill against time series observations from the SATURN observatory (Figure 11). From the perspective of observations at these stations and fixed depths, the sediment model is able to capture the variability and concentrations of suspended sediments. Comparisons between model results and field observations over the entire water column reveal limitations of both the hydrodynamics and suspended sediments obfuscated in point-wise time series comparisons (Figure 11 and Figure 12). At the North Channel cruise station OC1, three dominant features in suspended sediment are represented, but concentrations in the upper water column are slightly

overestimated (Figure 11). Elevated SSC in the upper water column corresponding with the growing tidal range indicates that model is accurately representing the increase of SSC in the system resulting from enhanced erosion. Model SSC is overestimated during ebbs near the bed corresponding with underprediction of stratification and overprediction of currents and shear. The underprediction of stratification during ebbs corresponds with the phase difference of the tide in simulations. Analysis of two-dimensional barotropic and three-dimensional baroclinic simulations indicate that baroclinicity substantially affects elevation and that elevation errors are related to the underprediction of the baroclinic pressure gradient (not shown). The implications of underpredicting baroclinicity on suspended sediment dynamics are more apparent at OC2 (Figure 12). During larger ebb tides, the model over-predicts the advection and mixing of the salt wedge resulting in a fresh water column at OC2 distorting the vertical location of suspended sediments. The dichotomy between model skill reflected in fixed station time series and the profiles of the water column exposes the difficulty and limitation of assessing model skill. Comparisons at fixed stations suggest the model captures variability of sediment. Similarly, the tidal variability of SSC are represented with comparisons from shipborne profiles, but show that the model completely misses the vertical distribution of suspended sediment sediments when stratification is not accurately represented during ebb tides. This highlights both the limits of the model and the limits of using fixed depth time series to assess sediment model skill and to describe suspended sediment in a stratified, dynamic estuary.

Sediment skill in our application is similar to studies using other models in other systems. As a stringent recent example, the range of Murphy Score (-4.06 to -0.72)

for SSC at the OC1, OC2, and SATURN stations is similar to those reported by *Ralston et al.* (2013) (-5.8 to 0.39) in the Skagit Bay located within the Puget Sound, USA. In that study 3 out of 5 stations had negative MS. Comparing correlation coefficients for SSC, the values obtained here are only modestly better (0.16 to 0.69) than those found by *Ralston et al.* (2013) (0.12 to 0.4). *de Nijs & Pietrzak* (2012) reported similar Willmott Scores (0.12 to 0.48). Skill for simulations of sediments continues to lag that of simulations of elevation, velocity, or salinity, highlighting the limitations and uncertainty of sediment modeling. Although much lower than skill measurements of elevation, velocity, or salinity, the model skill here is similar to results in other systems with other models, highlighting the limitations and uncertainty of contemporary sediment models especially when evaluated with rigorous skill metrics such as the Murphy Score.

The skill metrics used here are useful in assessing the predictive ability, but fail to comprehensively describe how well the model is representing sediment processes. The Murphy Scores at the fixed stations indicate that the model is no better than taking the mean of observations (the reference used for that metric), but the correlation coefficient and Willmott score suggest that the model is at least moderately skilled (Table 6). Skill metrics for OC1 and OC2 are similar, but the correlation coefficient and the Willmott score counter-intuitively suggest that the model is more skilled at OC2 than OC1. The critical aspect of the uncertainty in the conversion from NTU to SSC is not captured in these metrics. Nor do these metrics measure any form of feature similarity such as wavelets (Saux Picart et al., 2012) or self-organizing maps (Vilibić et al., 2016). Development of a more comprehensive feature-focused assessment of sediment model skill including uncertainty would ameliorate some of the short-comings of the current skill score

assessment methodology.

Specific skill measures aside, missing from the sediment model are a number of processes that may explain lack of sediment skill. The aggregation of fine sediment through flocculation contributes to the variability of the density, size distribution, and settling velocity of material associated with ETM in the Columbia River estuary (Reed & Donovan, 1994). The precise mechanisms leading to flocculation remain uncertain and even the descriptive properties associated with it including constituent material composition and time scales of aggregation and disaggregation remain open questions. A number of mechanisms to incorporate the effects of flocculation on settling velocity have been proposed dependent on local salinity (Lesser et al., 2004) and various representations of SSC and shear (Van Leussen, 1988; Whitehouse et al. 2000; Winterwerp et al., 2006; Baugh & Manning, 2007; Soulsby et al., 2013). Uncertainty in both expected behavior and characteristics of flocs for the Columbia River system discouraged application of these methods in this paper.

Shortwaves have been documented to cause and enhance erosion through a number of processes (Maa & Mehta, 1990; Le Hir et al., 2000) and are known to alter mixing fields (Kularatne & Pattiaratchi, 2008). The mouth and region outside of the Columbia estuary are high energy wave environments, but currents and sediment transport are dominated by mean advection with minor contributions from winds and waves (Elias et al., 2012). Given the minor contribution of waves to sediment transport near the mouth and the focus of this work further upstream in the stratified estuary where wave effects are less intense, we have chosen to neglect wave effects. This choice should be revisited once more important hydrodynamic model limitations, such as regime-dependent underprediction of

salinity intrusion (Kärnä et al., 2015), have been addressed.

2.6 Summary

Using idealized tests, we have validated an unstructured grid sediment model capable of reproducing suspended sediment dynamics, bed load transport, and associated morphodynamics forming a benchmark for three-dimensional sediment models. Despite being relatively well constrained, substantial sensitivity studies were required to find the optimal solution to these tests highlighting the uncertainty associated with sediment modeling. In our experience, critical details to reproduce these tests are frequently missing and we have taken efforts to provide what we believe to be sufficient details to reproduce including making the tests publically available (Lopez & Baptista, 2016b).

We have shown that the sediment model is capable of representing sediment dynamics in the energetic Columbia River estuary. Although the model was tuned to optimize model skill against observations, the model missed the vertical placement of suspended sediment when the hydrodynamics underestimated stratification. The persistent underprediction of stratification in the Columbia River, in spite of substantial prior work, is a recognition that circulation modeling itself has limitations. However, sediment skill lags that of hydrodynamics because inaccuracies in predicted hydrodynamics are compounded with uncertainty from missing processes, process simplification, and parameterization. Despite these limitations, the sediment model reproduces sediment dynamics in the Columbia River estuary. In particular, the model is able to reproduce elevated concentrations of suspended sediments near the bed during flood and ebb tides collocated with the upstream limit of salinity intrusion and captures the patch of

elevated SSC over the salt wedge when stratification is sufficiently represented by the hydrodynamics. In this sense, the model is a useful tool for studying ETM dynamics in the Columbia River estuary. Finally, we note that previously described scalability problems with SELFE have been partially ameliorated with the current version with the model able to scale beyond 256 cores.

3 SEDIMENT DYNAMICS IN THE COLUMBIA RIVER ESTUARY

3.1 Introduction

Many estuaries feature regions of elevated suspended sediment concentration (SSC) at the convergence of fresh and marine waters. Commonly referred to as Estuarine Turbidity Maxima (ETMs), these are often dominant sedimentary and ecological features of meso- and macro-tidal estuaries. From a classical perspective of estuarine processes, the convergence of a fluvial downstream current and a bottom-focused, upstream residual current resulting from gravitational circulation leads to trapping of sediment and organic material (Dyer, 1995). More generally, ETM result from a combination of these convergent currents (Allen et al., 1980; Festa & Hansen, 1978; Gelfenbaum, 1983) and other factors including: tidally generated asymmetry of multiple fields (Burchard & Baumert, 1998; Geyer, 1993; Jay & Musiak, 1994), lateral processes (McSweeney, Chant, & Sommerfield, 2016; Ralston et al., 2012), and, in some systems,

flocculation near the upstream limit of salt intrusion (Van Leussen, 1988). The relative importance of each process depends on the particular system and prevailing estuarine regimes within the system.

The overall complexity of the relevant processes elicited interest in numerical studies of ETM, where processes can be isolated and assessed in a controlled manner. Early ETM models required restrictions on the dimensionality, complexity of the domain, number of sediment classes, and represented processes to render the problem tractable. For example, *Festa & Hansen* (1978) used two-dimensional laterally-averaged model to state that gravitational circulation was sufficient to generate ETM-like features in flat-bottom estuaries. Using a similarly restricted model, *Burchard & Baumert* (1998) determined that gravitational circulation and asymmetry in velocity were both required to generate ETM, and that asymmetry in mixing impacted the suspended sediment concentration (SSC), but was not required for generation of the ETM. Using a depth-averaged two-dimensional and a three-dimensional model, *Brenon & Le Hir* (1999*)* described the formation of the Seine ETM as result of the combination of tidal pumping and density effects. Similarly using a combination of idealized two-dimensional and realistic three-dimensional simulations, *Burchard et al.* (2004) investigated the role of residual gravitational circulation and tidal mixing asymmetry in ETMs (extending *Burchard & Baumert* (1998)) and simulate ETM dynamics in the Elbe system. Using a 3D numerical model, *Lin & Kuo* (2003) located the York River ETM near the null point of the residual bottom flow and identified a secondary turbidity maxima associated with topographic features. *de Nijs & Pietrzak* (2012) used a three-dimensional model to represented multiple ETMs in the stratified Rotterdam Waterway.

ETMs occur in both channels of the Columbia River estuary. These ETMs are advected over tidal excursions of multiple kilometers with the extent and location varying at fortnight and seasonal scales (Gelfenbaum, 1983; Hubbell & Glenn, 1973; Reed & Donovan, 1994). Maximum suspended sediment concentrations similarly vary at tidal, fortnight and seasonal scales (Fain et al., 2001; Fox et al., 1984; Gelfenbaum, 1983; Jay & Smith, 1990; Reed & Donovan, 1994; Sherwood et al., 1990), in response to the seasonal modulation of river sources and the influence of tides and river discharge on ETM processes. The Columbia River ETMs have been largely described as in-channel features with generation attributed to convergent currents (Fox et al., 1984); mixing and stratification-induced internal tidal asymmetry combined with residual circulation (Jay & Musiak, 1994); and a balance between M_4 overtide currents produced by tidal asymmetry and residual salt and sediment exports (Jay & Musiak, 1995). (Jay et al., 2007a) and (Jay et al., 2007b) used non-dimensional numbers to assess the relative importance of advection, settling, aggregation, and trapping efficiency of ETM, and found trapping to be highest near the region where currents are slowest— i.e., near convergence of tidal and downstream currents. Using biological tracers to assess fortnightly variability in ETM trapping behavior, *Small & Prahl* (2004) suggested that ETMs act as traps during neaps tides that release material during springs under moderate summer flows, but not during the high flows of the spring freshet.

Prior work describing generation processes and characteristics of the Columbia River ETM, has been based mostly on observations from short-term and spatially sparse casts from cruises focused on the main channels. But even in the channels of the estuary there are not enough observations to enable a comprehensive spatial and temporal picture of variability. Furthermore, observations are almost

inexistent in the broad intertidal shoals and lateral bays, where potential interactions with the ETM has been hypothesized to be important.

To address these observational gaps, we conducted realistic three-dimensional simulations of the estuary, informed and validated against observations. These yearlong high-resolution simulations are designed to offer insights into the spatial and temporal variability of the ETM structure, and to place it within the broader context of sediment dynamics of the estuary. Section 3.2 introduces the Columbia River estuary and describes the available field observations and the methods used for modeling and analysis. Section 3.3 presents the results of the simulations including model-data comparisons. Section 3.4 presents a process-oriented analysis of along-channel sediment dynamics, identifies dominant sediment pathways, and presents a conceptual model for the Columbia River ETM. Section 3.5 discusses the implications of this work, and places it in context of the ETM literature for the Columbia River and other estuaries.

3.2 Methods

3.2.1 Observations

Data from two endurance observation networks are used in this study. One is the interdisciplinary SATURN network (Baptista et al., 2015), which includes multiple river-to-shelf stations measuring relevant variables including temperature, salinity, turbidity, and velocity. Of particular relevance are: SATURN-01, a vertical profiler located in the North Channel; SATURN-03, a multi-level station located in the South Channel; and SATURN-05, a single level station located in the tidal freshwater. Both SATURN-01 and SATURN-03 will be extensively used for model-data comparison, while SATURN-05 provides upstream boundary conditions for

the modeling. The other endurance network is the US tidal gauge network, multiple stations of which have been used to calibrate and validate the circulation model in separate but supporting studies (Kärnä et al., 2015; Kärnä & Baptista, 2016), and one (Tongue Point) will be referred to in this study. All stations used in this study are found in Figure 14.

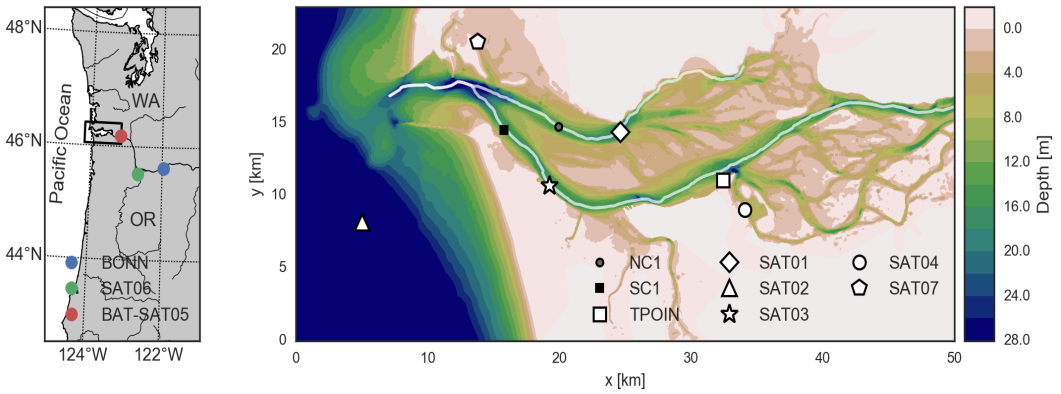

Figure 14 Map of the Pacific Northwest, United States. (a) A map of the states of Oregon and Washington with markers denoting the locations where river flux is measured with the black frame indicating the location of the map in (b). (b) The Columbia River estuary denoting stations used in this paper. The two white lines follow the thalweg in the North and South Channels and are used to define transects throughout the paper.

Optical measurements of turbidity at SATURN stations are made with WET Labs fluorometers that emit a 700 nm light source and are calibrated using a formazine standard. To facilitate observation-model comparisons, we convert optical turbidity measurements (NTU) into suspended sediment concentrations (SSC) using the correlation:

$$\mathrm{SSC} = 2.16\, NTU^{1.26}/1000 \tag{13}$$

derived from a least squares fit ($R^2 = 0.76$). Specifically, *Lopez & Baptista* (2016a) derived this correlation based on results of third-party gravimetric analyses of water samples taken across seasons during research cruises in the estuary, and at

a freshwater station at Beaver Army Terminal (USGS #14246900). The water samples were collected across a range of seasons, river discharge, and salinity conditions providing good coverage of estuarine parameter space and variability in material in the water column.

3.2.2 Numerical model

The numerical model used in this study was the three-dimensional unstructured-grid baroclinic circulation model SELFE (Zhang & Baptista, 2008), augmented with a sediment transport module (Lopez & Baptista, 2016a). SELFE solves the Reynolds-averaged Navier-Stokes equations using the Boussinesq and hydrostatic assumptions in a finite-element framework. The advection of momentum is solved using the semi-Lagrangian Eulerian-Lagrangian Method and scalar transport is solved using an Eulerian finite volume upwind (used here) or TVD scheme. In this study the governing equations are closed with a second-order k-ε turbulence closure model using the Canuto-A stability function from the GOTM library (Umlauf, Bolding, & Burchard, 2011).

The choice of model parameters, summarized here for convenience, was informed by previous studies of the system (Kärnä et al., 2015; Kärnä & Baptista, 2016) and were used previously in *Lopez & Baptista* (2016a). The model domain covered the Northeast Pacific from Vancouver Island (~50° N) south to the coast of Northern California (~40° N) and from ~300 km off the coast (~128° W) into the Columbia River upstream 85 km to the river boundary at Beaver Army Terminal (Figure 14). The vertical grid consisted of 54 vertical levels: 34 S-levels plus 17 Z-levels used in depths greater than 100 m. In depths less than 30 m, most of the estuary, the vertical levels reverted to sigma-layers. A uniform bottom roughness was imposed ($z0 = 0.004$ m) to maximize salinity intrusion based on sensitivity analysis for the

same domain and model parameterization (Kärnä et al., 2015). Atmospheric forcings were imposed from the North American Regional Reanalysis NOAA/NCEP hindcasts (Mesinger et al., 2006). Ocean boundaries were forced with temperature, salinity, and sub-tidal elevations from Navy Coastal Ocean Model (Barron et al., 2006) hindcasts and with 8 tidal constituents (O_1, K_1, Q_1, P_1, K_2, N_2, M_2, S_2) added from a regional inverse model (Myers & Baptista, 2001). River flux and temperature were imposed at Beaver Army Terminal using observations (USGS #14246900).

The sediment module was derived from the Community Sediment Transport Model (CSTM) (Warner et al., 2008) and ported for use with the numerical methods and unstructured grids native to SELFE (Pinto et al., 2012). The sediment model solves for the advection and diffusion of a user-specified number of non-cohesive sediment classes and includes interactions with the bed and dynamic morphology. The sediment model parameterization was the same used to study the Columbia River estuary in *Lopez & Baptista* (2016a)using four non-cohesive sediment classes corresponding to clay, fine silt, silt, and sand sized classes characteristic of the system (Fain et al., 2001; Reed & Donovan, 1994). The initial conditions for the bed were dominated by the sand size class (90%) with minor percentages of the other smaller size classes based on descriptions of the bed composition (Fox et al., 1984; Sherwood et al., 1990). Boundary conditions for SSC were based on a rating curve derived from observations at Beaver Army Terminal (USGS #14246900), as described in *Lopez & Baptista* (2016a) . Model parameterization for the sediment model is detailed in Table 8.

Table 8 Sediment model parameters for Columbia River estuary for the 2012 simulation.

	Sediment classes			
	Wash	**Fine Silt**	**Silt**	**Sand**
Median diameter [mm]	0.01	0.03	0.06	0.125
Settling velocity [mm/s]	0.05	0.5	2.0	10.0
Erosion rate [kg/m^{2}s]	1.0 x 10-5	1.0 x 10-4	1.0 x 10-4	1.0 x 10-3
Critical stress [Pa]	0.10	0.15	0.15	0.2
Porosity [-]	0.65	0.6	0.55	0.50
Bed initial conditions [%]	0.05	0.1	0.1	0.75

3.2.3 Estuarine parameter space

Simulations were conducted and analyzed for a full year, 2012. However, we used the concept of estuarine regimes to inform and focus our analysis, and to provide context for the state of the estuary. Regimes were defined based on the estuarine classification system of *Geyer & MacCready* (2014), which constructs a parameter space based on the non-dimensional freshwater Froude number and a non-dimensional mixing number. The freshwater Froude number, Fr_f, is defined as

$$Fr_f = \frac{U_R}{\sqrt{\beta g s_{ocean} H}} \tag{14}$$

where U_R is the velocity of the river, β is the haline contraction coefficient, g is the gravitational acceleration, s_{ocean} is the maximum marine salinity, and H is the characteristic depth of the estuary. The mixing number, M^2, is defined as

$$M^2 = \frac{C_D U_T^2}{\omega N_0 H^2} \quad (15)$$

where C_d is a characteristic drag coefficient, U_T^2 is the amplitude of the depth-averaged tidal velocity, ω is the tidal frequency, and N_0 is the buoyancy frequency. We calculated Fr_f and M^2 from model results extracted along cross-sections in the lower estuary, using the method of *Kärnä et al.* (2015).

As originally reported by *Kärnä et al.* (2015), and confirmed by *Kärnä & Baptista* (2016) based on seven years of simulation, the Columbia River estuary functions across four estuarine regimes: salt wedge (for larger river discharges and weaker tides), time-dependent salt wedge (larger discharges, stronger tides), highly stratified (weaker discharges, weaker tides) and partially mixed (weaker discharges, stronger tides).

3.2.4 Model skill metrics

Model skill is assessed using the standard root mean square error (RMSE), correlation coefficient (ρ), Willmott skill score (WS), and Murphy score (MS) as in *Lopez & Baptista* (2016a) and described in Section 2.3.4. Despite the admitted flaws in use with the Willmott skill score (Ralston et al., 2013), it is used here as a means to compare with previous studies and to provide a set of skill metrics to provide a holistic appraisal of model skill.

These metrics are used to evaluate the model skill of predicted elevation, velocity, temperature, salinity, and SSC throughout the Columbia River estuary for the entire year and representative months (Table 9). These months were selected to assess model skill in detail over the four estuarine regimes and across the range of river discharge. February is representative of the intermediate-flow winter period which includes the periodic effects of winter storms where the estuary migrates

between strongly stratified (1 February through 7 February 2012) and partially mixed (17 February through 24 February 2012). During the spring freshet the estuary transitions between time-dependent salt wedge (2 May through 9 May 2012) and salt wedge (11 May through 17 May 2012). Results from September are included to highlight dynamics during a period of low river discharge despite occupying the same partially mixed (14 September through 21 September 2012) and strongly stratified (4 September though 11 September 2012) regimes as in February.

Table 9 Description of selected time periods for analysis covering the range of forcing conditions. *Tidal range* is the average tidal range over the period. *Mean discharge* is taken as the sum of the discharge from the Columbia River at Bonneville Dam and the Willamette River at Morrison Bridge in Portland, Oregon averaged over the selected period.

Dates	Regime	Tide	Tidal Range [m]	Mean discharge [m^3/s]
1 Feb. – 7 Feb.	Strongly stratified	Neap	2.5	5,820
17 Feb. – 24 Feb.	Partially mixed	Spring	2.8	5,300
2 May – 9 May	Time-dependent Salt wedge	Spring	3.0	12,700
10 May – 16 May	Salt wedge	Neap	2.3	10,600
4 Sept. – 11 Sept.	Strongly stratified	Neap	2.2	4,300
14 Sept. – 21 Sept.	Partially mixed	Spring	2.9	3,700

3.2.5 Sediment transport and decomposition

To understand dominant transport mechanisms, suspended sediment fluxes were computed from the simulations and were decomposed into tidally-averaged and fluctuating terms. The analysis is similar to that of *Kärnä et al.* (2015) for salt transport in the estuary, but here we use a 36-hour low-pass Butterworth filter to separate the residual transport, Q_a, from the instantaneous transport, Q_t, as

$$\mathrm{Q_a} = \int \bar{\mathrm{u}}(\mathrm{z})\ \overline{\mathrm{SSC}}(\mathrm{z})\mathrm{dz} \tag{16}$$

and

$$Q_t = \int u'(z)\, SSC'(z) dz \quad (17)$$

where $\bar{u}$ is the tidally averaged (filtered) along- or cross-channel velocity, $\overline{SSC}$ is the tidally averaged (filtered) SSC, u' is the instantaneous along- or cross-channel velocity, and SSC' is the instantaneous SSC. Using this decomposition, Q_a represents sediment transport by residual circulation and Q_t represents transport due to tidal pumping as in *Geyer*, [2001], *Scully & Friedrichs* (2007), and *McSweeney et al.* (2016). Following *Kärnä et al.* (2015) and Hamilton (1990) the two terms are referred to as transport due to mean advection and tidal pumping.

3.3 Results

Here we describe the state of the estuary using model results informed by observations, and evaluate model skill using the metrics and selected periods described in Section 3.2.4.

3.3.1 River discharge, tides, and currents

The discharge into the lower estuary as measured at Beaver Army Terminal ranged from a low of 3,000 $m^3\ s^{-1}$ in October to a high of over 16,000 $m^3\ s^{-1}$ during the freshet (Figure 2). A large winter storm and constant rain in January rapidly increased discharge from 6,000 $m^3\ s^{-1}$ to nearly 14,000 $m^3\ s^{-1}$ as the discharge out of the Willamette increased from less than 1,000 $m^3\ s^{-1}$ to over 5,000 $m^3\ s^{-1}$. Storms late in the year during the months of November and December provoked a similar response (Figure 15).

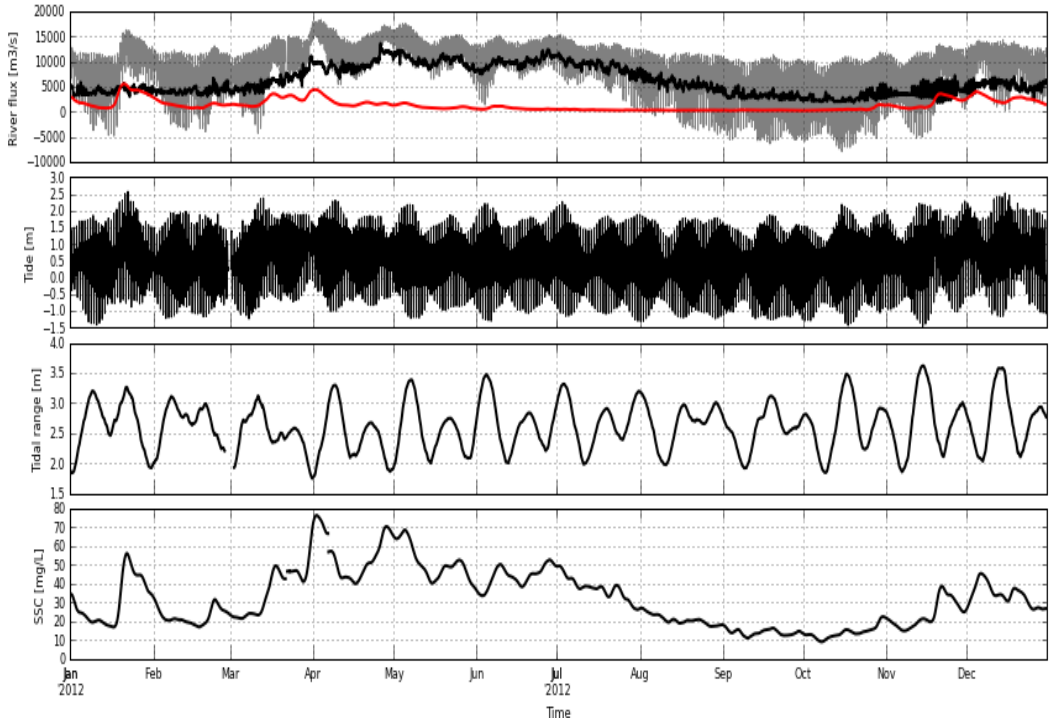

Figure 15 Instantaneous river and tidal conditions for 2012. (a) River discharge at Beaver Army (grey), Bonneville dam (black), and SATURN-06 in the Willamette River (red). (b) Tidal elevation as measured at Tongue Point, Oregon. (c) Tidal range as measure at Tongue Point, Oregon. (d) Estimate of suspended sediment concentration at Beaver Army Terminal, Oregon.

Over the year the tidal range varied from ~2 m to 3.6 m and the model was able to capture both the tidal range and semi-diurnal patterns with high skill as measured near the South Channel inside the estuary at Tongue Point, Oregon (WS = 0.98, MS = 0.93) (Table 10).

Tidal velocities in the main channels ranged from 2 m s^{-1} during floods to 2.5 m s^{-1} during ebbs with substantially slower velocities in lateral bays and shoals. The larger of the diurnal ebb generated much faster velocities (>= 2.5 m s^{-1}) than smaller ebbs (>= 2.0 m s^{-1}). Similarly, currents were much faster during spring tides than neaps, commonly reaching 3 m s^{-1} near the surface during ebbs. Comparing depth-averaged observations and model results at SATURN-01, a

station notoriously difficult to model (Kärnä et al., 2015), the model reproduced the tidal and tidal month variability well. Both the eastward depth-averaged velocity (WS=0.94, MS=0.65) and the northward depth-averaged velocity (WS=0.88, MS=0.73) were represented reasonably well by the model (Table 10).

Table 10 Model skill averaged from all available observations for 2012 across the selected times and regimes (SS - strongly stratified, PM - partially mixed, SW - salt wedge, TDSW - time-dependent salt wedge).

Variable	Period	Bias	ρ	WS	MS	RMSE
Elev	2012	0.145	0.981	0.983	0.933	0.220
Salt	2012	-0.314	0.910	0.953	0.821	4.090
Temp	2012	0.005	0.960	0.980	0.921	1.050
SSC	2012	-0.007	0.037	0.381	-0.569	0.014
Elev	SS	0.132	0.995	0.990	0.958	0.149
Salt	SS	-1.150	0.886	0.934	0.763	3.976
Temp	SS	-0.725	0.912	0.843	0.368	0.848
SSC	SS	-0.012	-0.095	0.189	-39.149	0.013
Elev	PM	0.170	0.997	0.987	0.945	0.201
Salt	PM	-1.000	0.898	0.943	0.792	4.090
Temp	PM	-0.196	0.883	0.927	0.737	0.496
SSC	PM	-0.007	0.447	0.492	-2.776	0.009
Elev	SW	0.259	0.981	0.955	0.818	0.290
Salt	SW	-2.217	0.804	0.874	0.601	6.625
Temp	SW	0.000	0.783	0.864	0.611	0.850
SSC	SW	-0.005	0.480	0.472	-4.941	0.007
Elev	TDSW	0.237	0.985	0.975	0.902	0.286
Salt	TDSW	-1.017	0.830	0.903	0.672	4.804
Temp	TDSW	-0.791	0.830	0.616	-1.806	0.866
SSC	TDSW	0.007	0.000	0.430	0.560	-2.282

3.3.2 Salinity

Salinity varies strongly at tidal and spring-neap scales, and exhibits strong diurnal asymmetry, but similar patterns emerge over regimes with variations in details of salinity intrusion length, stratification, and the horizontal density gradient. Here we will specifically describe salinity in terms of the general behavior of the salt-wedge over a tidal cycle and the effects it has on stratification. Descriptions of SIL and horizontal density gradient will be discussed in Section 3.4.1. Generally, the channels remain stratified through most phases of the tide, except for larger ebbs (Figures 16, 18, 20). During floods, the advance of the salt wedge during floods increases stratification as it migrates up the channel and into the adjacent Desdemona Sands and upstream shoals. During ebbs, the isohalines tilt as fresher water near the surface accelerates downstream, but stratification decreases over the duration of the ebbing tide as the salt wedge is both mixed out by interfacial shear and advected downstream. However, the slower velocities of smaller semi-diurnal ebbs generate low shear and lower rates of mixing frequently leaving the water column stratified.

Model skill for salinity averaged over all available observations and for the entire year was high for the entire system (WS=0.94, MS=0.78) (Table 10). Model skill was highest during low river flow in September when the estuary occupied the partially mixed and strongly stratified regimes (Table 9). Generally, as river discharge increased model skill dropped due to underprediction of salinity retention during ebb tides at difficult to model stations, especially SATURN-01 (Figure 14), as has been described in *Kärnä et al.* (2015).

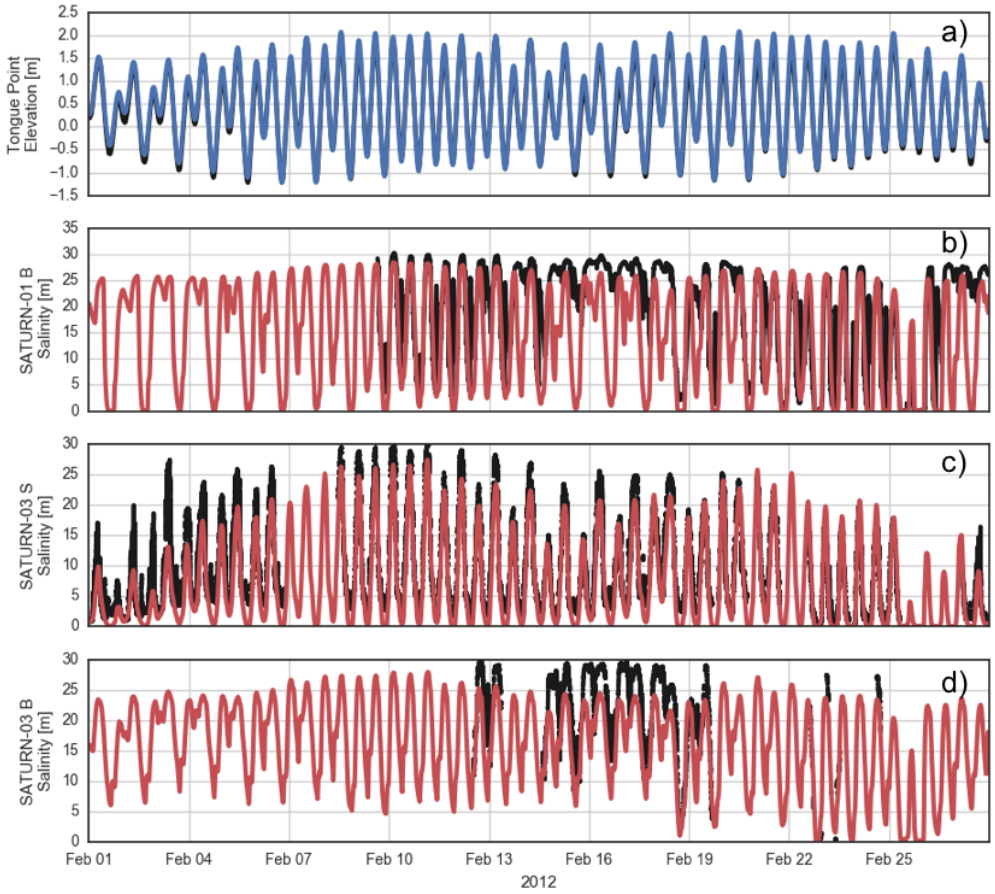

Figure 16 Observations (black) and model results for February 2012 of: (a) Elevation at Tongue Point. (b) Salinity at SATURN-01 15 m depth. (c) Salinity at SATURN-03 2.4 m depth. (d) Salinity at SATURN-03 13.4 m depth.

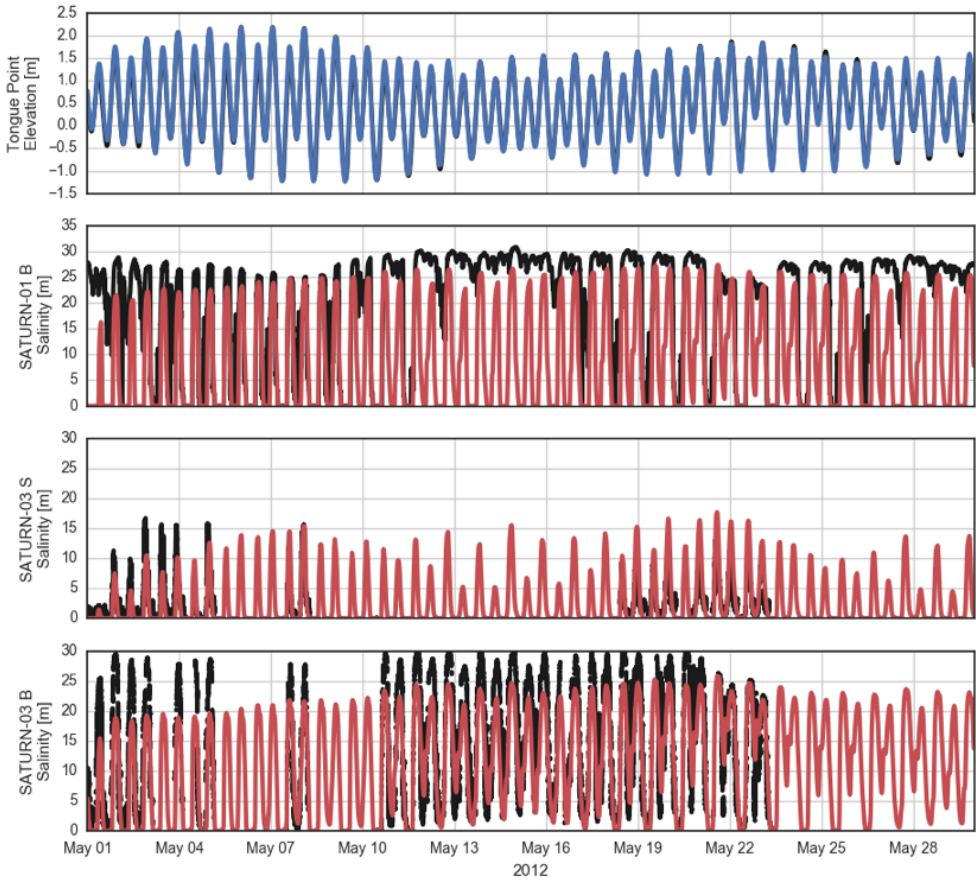

Figure 17 Observations (black) and model results for May 2012 of: (a) Elevation at Tongue Point. (b) Salinity at SATURN-01 15 m depth. (c) Salinity at SATURN-03 2.4 m depth. (d) Salinity at SATURN-03 13.4 m depth.

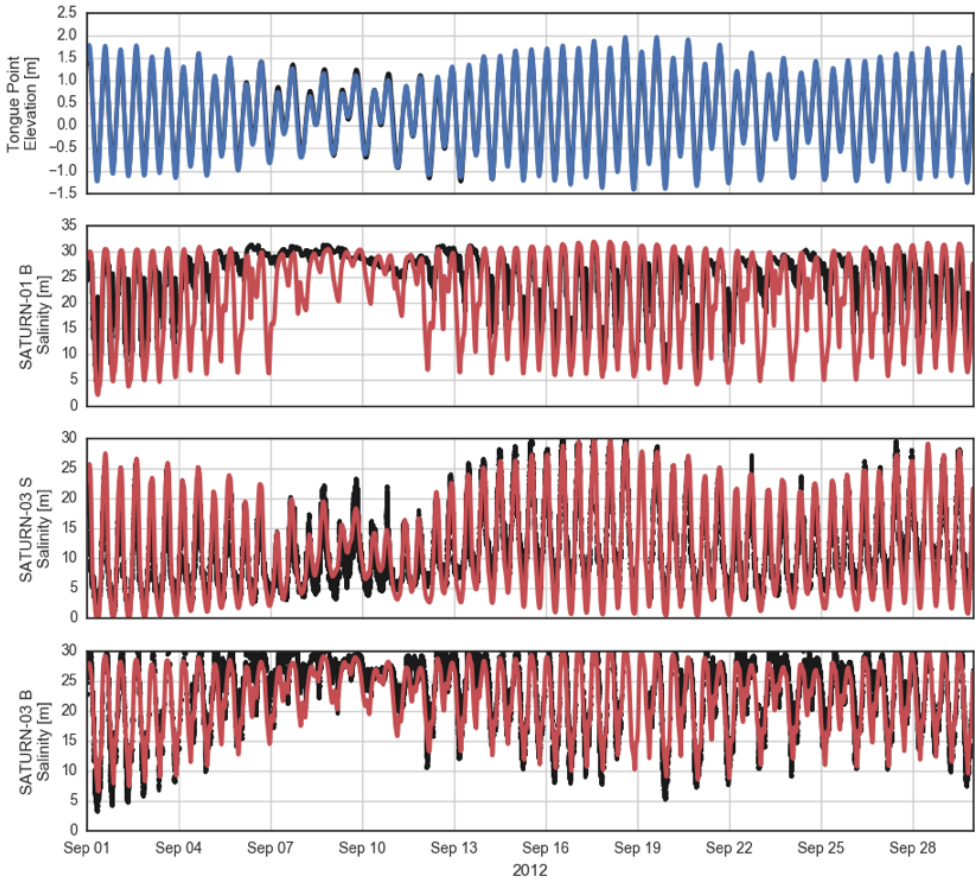

Figure 18 Observations (black) and model results for September 2012 of: (a) Elevation at Tongue Point. (b) Salinity at SATURN-01 15 m depth. (c) Salinity at SATURN-03 2.4 m depth. (d) Salinity at SATURN-03 13.4 m depth.

3.3.3 Suspended Sediment

Like salinity, suspended sediment dynamics varied at tidal and spring-neap scales while exhibiting strong diurnal asymmetry, with common patterns emerging over regimes. Generally, SSC was higher in the North Channel than the South Channel, and SSC was higher in spring tides compared to neaps (Figures 19 through 24). When tidal asymmetry was minimal, as in February during spring tides, the SSC for each semi-diurnal flood was nearly equal. In contrast, when diurnal asymmetry increased as in the February neap period, a strong asymmetry was generated in the SSC generating a daily maximum during the larger flood tide. Generally, the highest SSC was found between the 5 and 20 psu isohalines near the bed - the classical flood ETM. An exception to this was found in May when the highest SSC was found in an ebbing ETM trailing a receding salt wedge (Figures

Figure 21 and 22). The lowest SSC in both the channels is most frequently during ebb tides within the pycnocline where suppressed mixing allows sediment to settle into the salt wedge (Figures 20, 22, 24).

During ebbs in the North Channel when the water column remained stratified, elevated patches of SSC advected downstream passing over salt wedge, a feature we deemed a suspended sediment patch (SSP). Specifically, we define a SSP as any patch of suspended sediment interacting with the salt-wedge, but distinct from the classical bottom focused ETM. This specific patch frequently appeared at SATURN-01 during every ebb of spring tides, but only during the larger ebbs during neaps. The ebbing SSP is infrequently observed in the South Channel suggesting distinct suspended dynamics between the two channels. Another SSP develops in front of the salt wedge in both channels during flood tides. This SSP is distinct from the

classical bottom trapped ETM because it typically has lower concentrations and is not trapped by stratification.

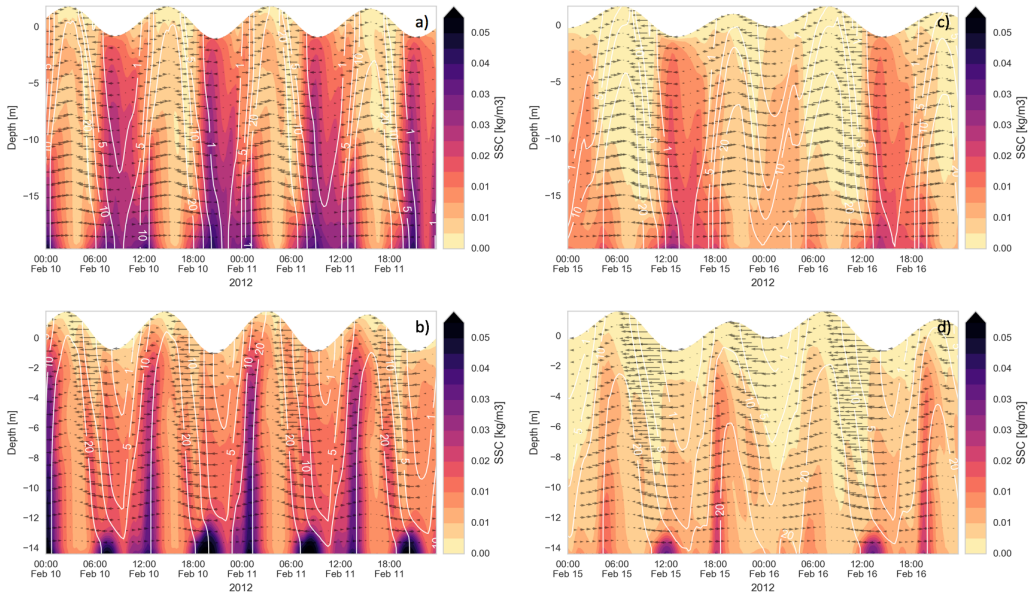

Figure 19 Instantaneous profiles in February 2012. Color indicates SSC, white lines are isohalines, and quivers are along channel velocity. (a) SATURN-01 spring. (b) SATURN-03. (c) SATURN-01 neap. (d) SATURN-03 neap.

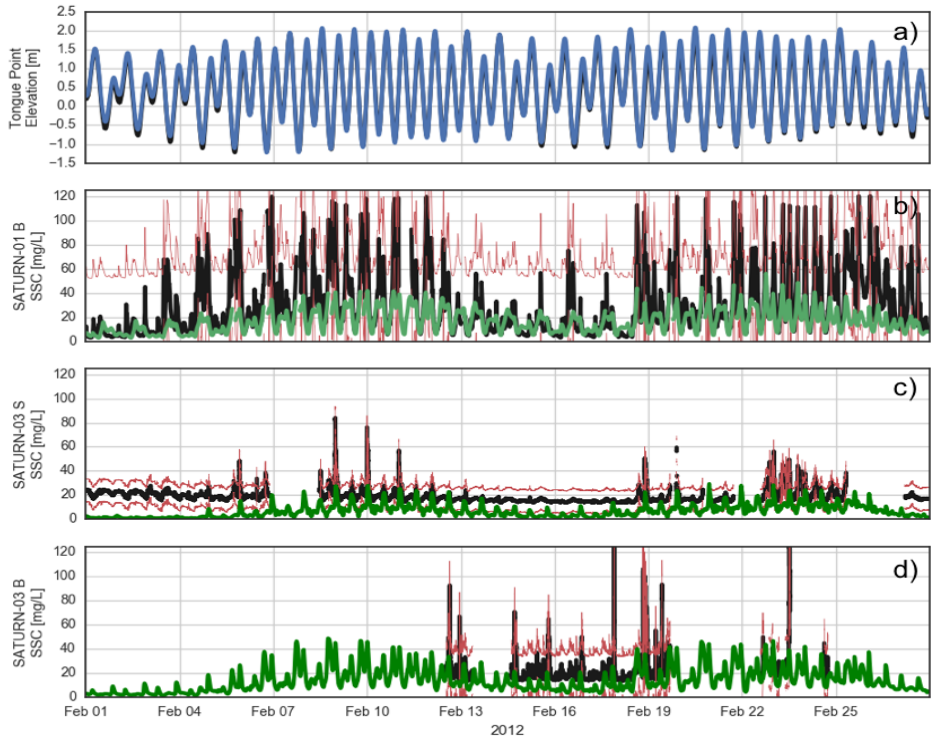

Figure 20 Observations (black) with 95% confidence interval (red) and model (green) results for February 2012 of: (a) Elevation at Tongue Point. (b) SSC at SATURN-01 15 m depth. (c) SSC at SATURN-03 2.4 m depth. (d) SSC at SATURN-03 13.4 m depth.

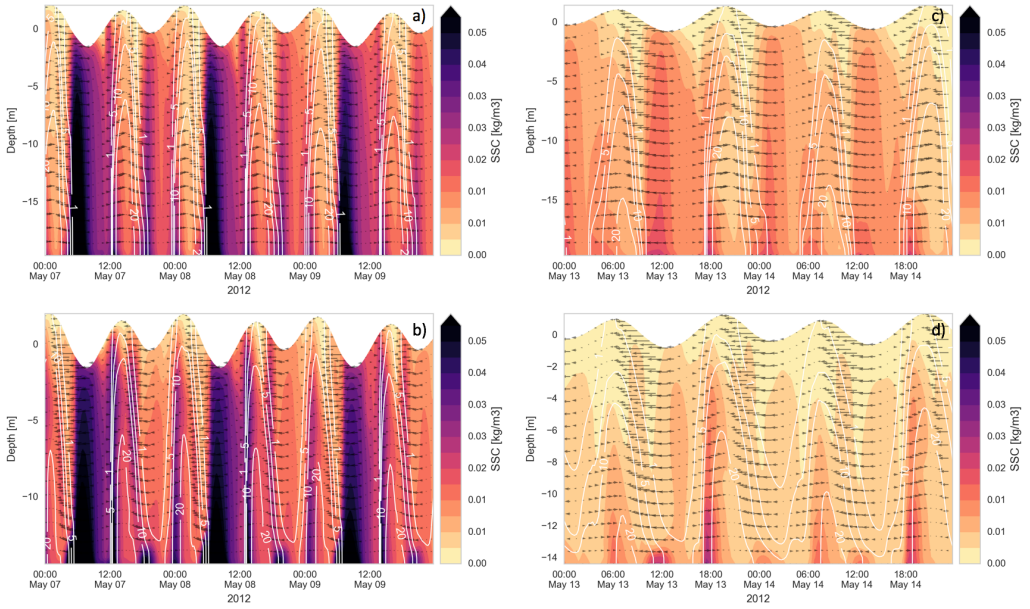

Figure 21 Instantaneous profiles in May 2012. Color indicates SSC, white lines are isohalines, and quivers are along channel velocity. (a) SATURN-01 spring. (b) SATURN-03. (c) SATURN-01 neap. (d) SATURN-03 neap.

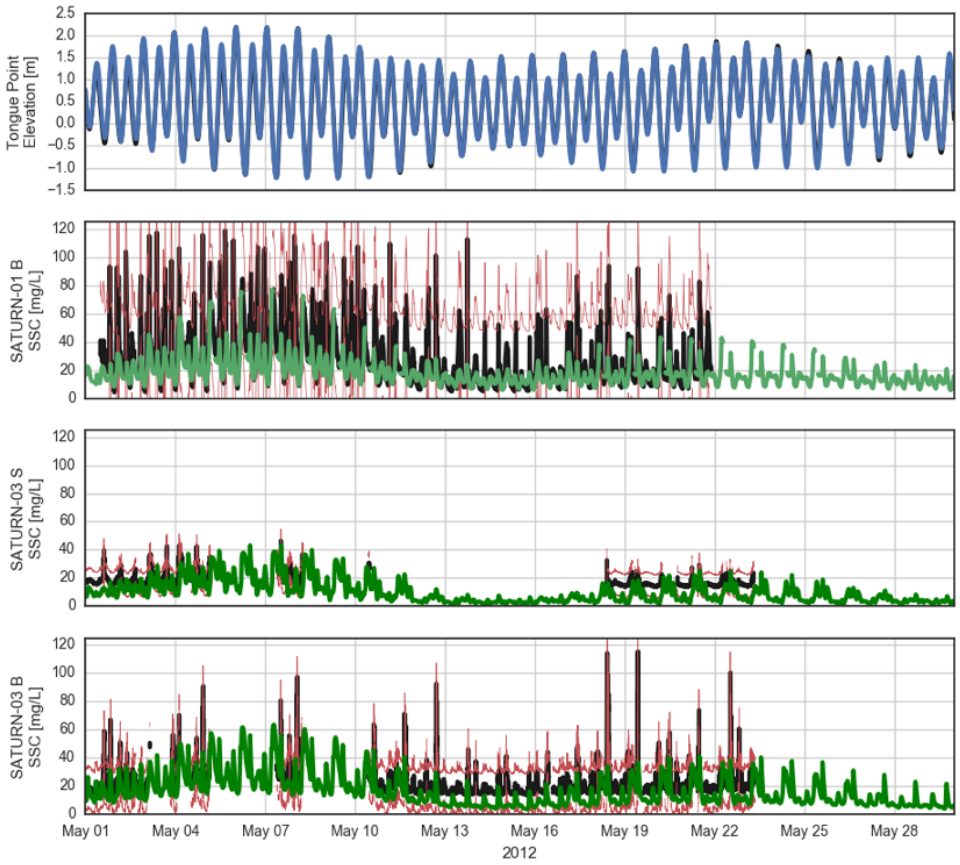

Figure 22 Observations (black) with 95% confidence interval (red) and model (green) results for May 2012 of: (a) Elevation at Tongue Point. (b) SSC at SATURN-01 15 m depth. (c) SSC at SATURN-03 2.4 m depth. (d) SSC at SATURN-03 13.4 m depth.

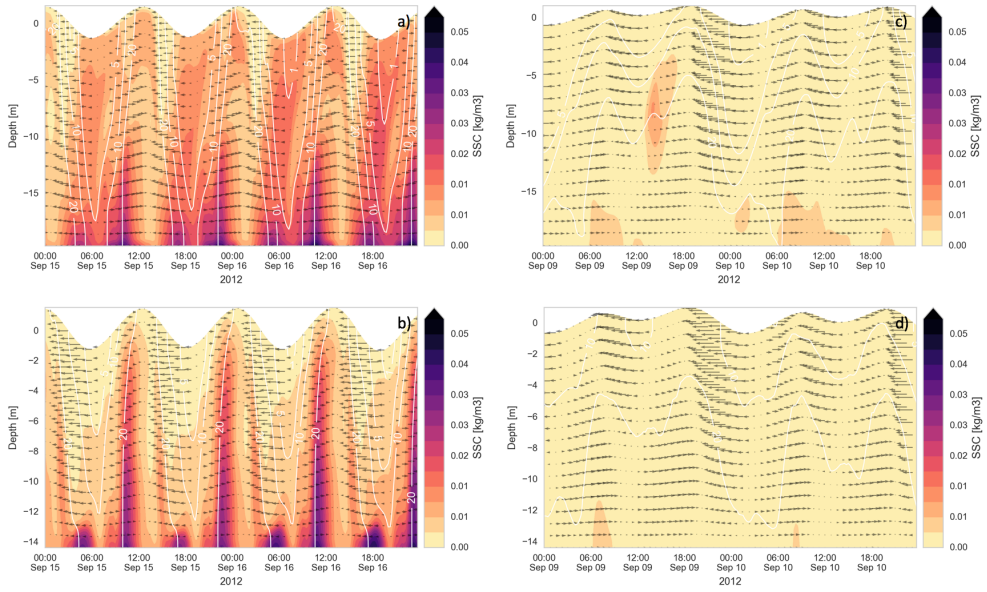

Figure 23 Instantaneous profiles in September 2012. Color indicates SSC, white lines are isohalines, and quivers are along channel velocity. (a) SATURN-01 spring. (b) SATURN-03. (c) SATURN-01 neap. (d) SATURN-03 neap.

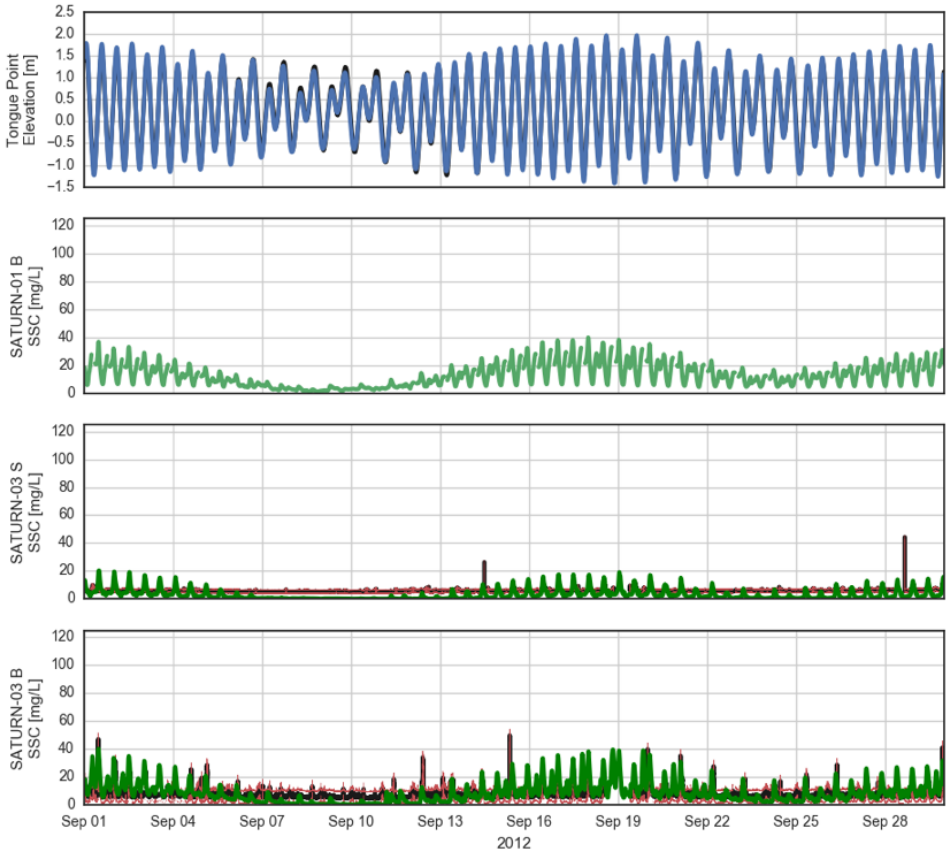

Figure 24 Observations (black) with 95% confidence interval (red) and model (green) results for September 2012 of: (a) Elevation at Tongue Point. (b) SSC at SATURN-01 15 m depth. (c) SSC at SATURN-03 2.4 m depth. (d) SSC at SATURN-03 13.4 m depth. No observations are available at SATURN-01 at this time.

Model skill of suspended sediment is lower than other physical variables (WS=0.38, MS=-0.57). The predicted average and peak SSC were lower than observed (Table 10). However, the model did a reasonable job of reproducing the relative temporal variability observed on tidal day and tidal month periods. The model correctly predicted increases in SSC throughout the system associated with the ETM, but frequently under-predicted the observed values. It also reproduced spring-neap variability, but over-predicted the differences in SSC between the spring and neap periods (Figures 20, 22, 24).

3.4 Analysis

3.4.1 Residual Along-Channel Dynamics

The residual along-channel circulation and sediment dynamics in the North and South Channels are synthesized in Figures 12-14, for February, May and September, respectively. Each figure shows residuals of salinity, velocity and SSC (obtained by 24.8h filtering along channel thalwegs) for the North and South channels, for conditions near maximum spring and near- minimum neap.

In February, the limit of salinity intrusion (as defined by the low-pass filtered 1 psu isohaline) extended ~30 km upstream in both the North and South channels and during both spring and neap tides (Figure 25). While the extent of salt intrusion was largely insensitive to the transition, SSC increased considerably in both channels from neaps to springs. Maximum SSC was higher in the North Channel than in the South Channel, but the region with concentrations above river levels cover a larger area in the South Channel. The highest observed SSC in the North Channel were located between the 15 and 20 psu isohalines near the

convergence of the residual currents. A broader region of SSC elevated above riverine concentrations was observed between the 5 and 20 psu isohalines. In the South Channel, elevated SSC was centered around (including upstream) of the 1 psu isohaline. A patch of elevated SSC followed the 10 psu isohaline (~17 km mark) in the North Channel resulting from the advection of the SSP over the salt wedge during ebbs; this feature was not present in the South Channel. In both channels exchange flow setup in the stratified estuary between river km 0 and ~18 in the North Channel and river km 0 and ~22 in the South Channel.

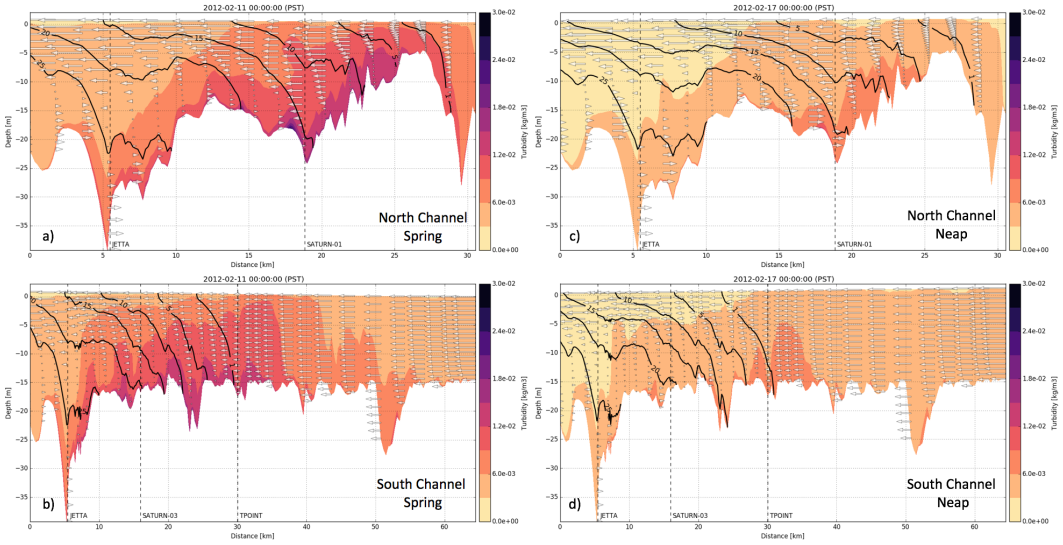

Figure 25 Residual along-channel dynamics along thalwegs in February. (a) North Channel spring. (b) South Channel spring. (c) North Channel neap. (d) South Channel neap.

In May the salinity intrusion length was greater in the North Channel than in the South Channel, a consequence of the large river discharge funneled through the South Channel (Figure 26). As in February, the intrusion length in the North Channel (~25 km) did not vary significantly between springs and neaps. However, the horizontal density gradient in the South Channel expanded and contracted in response to variation in the tidal range. During the spring tide the 1 psu isohaline was located ~21 km upstream of the mouth with $^{dS}/_{dx}$ = 2.5 psu km^{-1} and during

the neap tide the 1 psu isohaline migrated to ~23 km upstream of the mouth and $^{dS}/_{dx}$ adjusted to 1.6 psu km^{-1}. The maximum SSC were located between the 5 and 20 isohalines near the bed in both channels. Presence of the ebbing SSP over the pycnocline was observed in both channels. The North Channel SSP was located near the 15 psu isohaline ~5 km upstream of the mouth. Evidence of the SSP in the South channel was observed in overhang of elevated concentrations along the 5, 10, 15, and 20 psu isohalines between ~7 and 15 km upstream of the mouth. Notably, the highest concentrations in the system in May were located far upstream along the South Channel adjacent to Cathlatmet Bay resulting from the confluence of elevated fluvial SSC and high concentrations exported from the bay. The residual velocity fields during the spring tide were oriented downstream even in the stratified water column except very near the mouth in both channels.

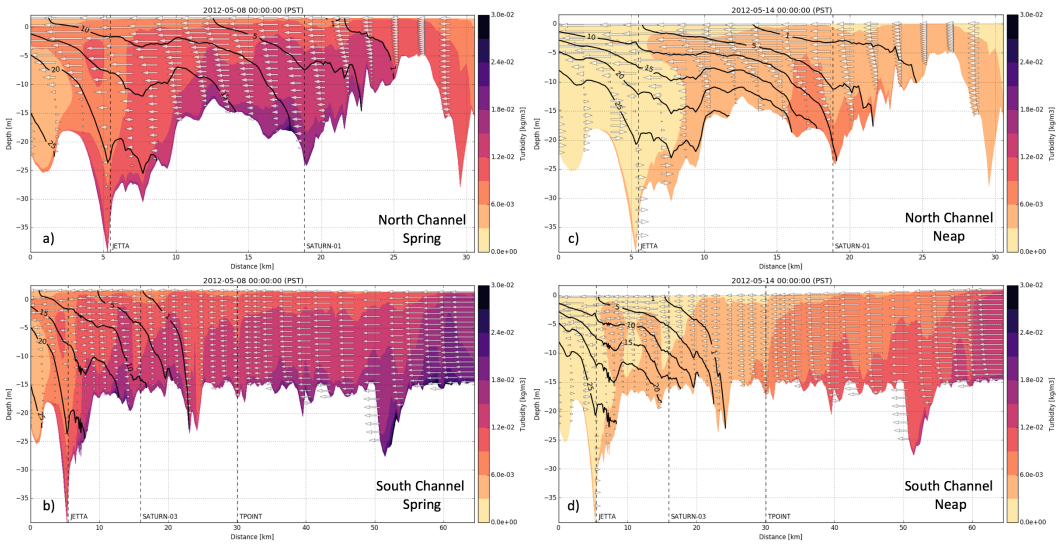

Figure 26 Residual along-channel dynamics along thalwegs in May. (a) North Channel spring. (b) South Channel spring. (c) North Channel neap. (d) South Channel neap.

In September the salt wedge moved further upstream than in both February and May in response to the low river discharge (Figure 27). In the North Channel, the

1 psu isohaline moved upstream past river kilometer 30 km with $^{dS}/_{dx}$ =1.5 psu km^{-1} during the spring tide and decreasing to 2 psu km^{-1} during neap. In the South Channel, SIL was ~30 km upstream of the mouth with $^{dS}/_{dx}$ = 1.6 psu km^{-1} during the spring tide and a salinity intrusion length of almost 40 km during neap with $^{dS}/_{dx}$ contracting slightly to 1.5 psu km^{-1}. The highest concentrations of suspended sediment were again found between the 10 and 15 psu both the North and South Channel for both the spring and neap tides. SSC throughout the system was the lowest observed for the year in September. Residual exchange flow occurred in both channels throughout the entire period in a larger proportion of the estuary due to the greater SIL than other months.

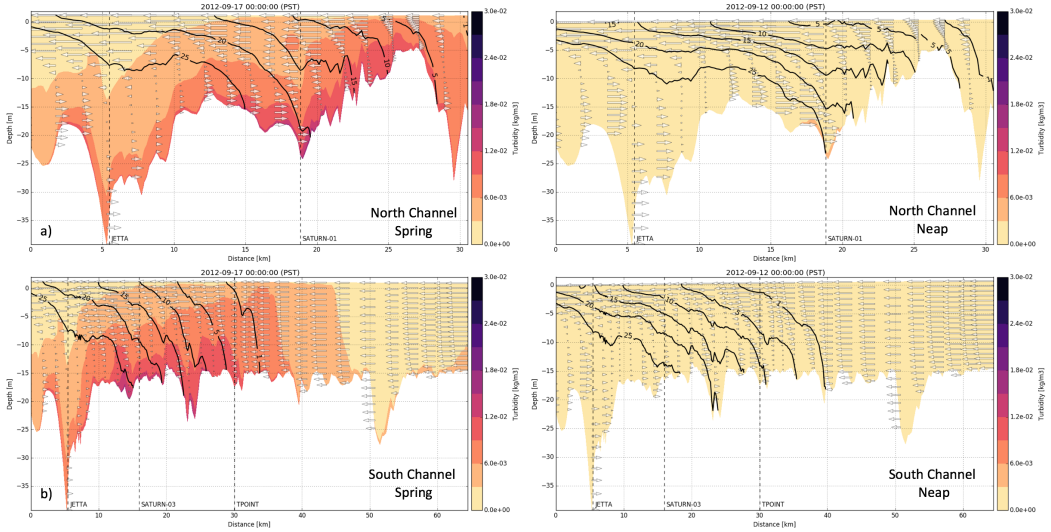

Figure 27 Residual along-channel dynamics along thalwegs in September. (a) North Channel spring. (b) South Channel spring. (c) North Channel neap. (d) South Channel neap.

3.4.2 Transport processes

Using the decomposition of sediment flux defined in Section 2.4, we gain insight into the variability and processes associated with sediment transport along the North and South Channels for 2012 (Figure 16). Mean advection in both the North and South Channels was directed downstream for the entirety of the year at

channel stations. Tidal pumping varied in magnitude far greater than the mean transport and occasionally changed orientation generating upstream transport at specific stations. The highest rate of suspended sediment transport due to tidal pumping occurred in May while the estuary was in a time-dependent salt wedge regime (river discharge: ~15,000 m^3 s^{-1}, tidal range: ~3.5 m). The lowest mean transport and tidal pumping occur during September while the estuary was in a strongly-stratified regime (river discharge ~5,000 m^3 s^{-1}, tidal range ~2 m).

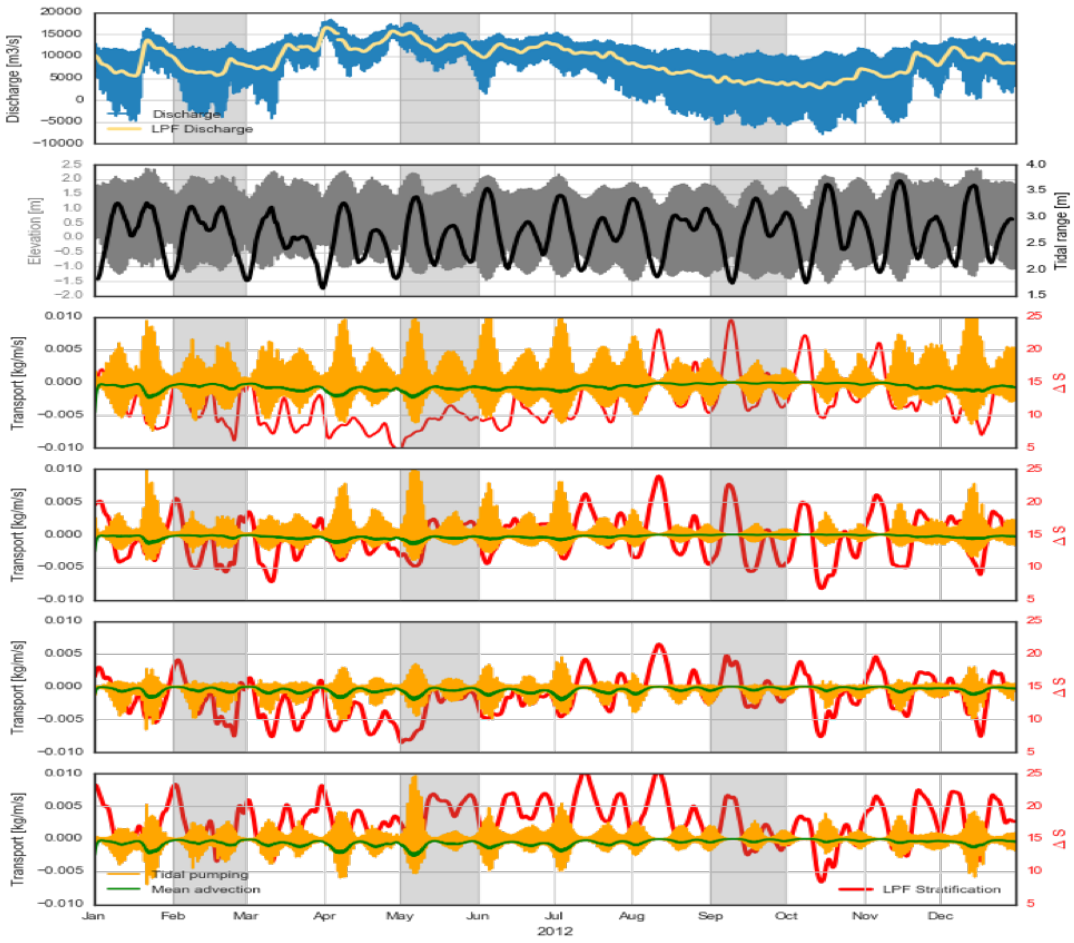

Figure 28 a) Discharge at Beaver Army Terminal, Oregon. (b) Elevation and tidal range at Tongue Point, Oregon. Along channel sediment flux through 2012 by instantaneous tidal pumping (yellow) and mean advection (green) with low-pass filtered stratification for context (red) at: (c) SATURN-01 (d) North Channel Point 1 (NC1) (e) SATURN-03 (f) South Channel Point 1 (SC1).

Throughout the year, but most apparent during the low-flow period, an inverse relationship exists between stratification and sediment transport (Figure 28). During the smaller of the neap tides in early September, when the estuary is in a strongly stratified regime and stratification is high in all stations ($\Delta S > 20$ psu), the suspended sediment transport was nearly zero indicating export near the surface was matched by import near the bed. As the tidal range increased in the transition to spring tides, the stratification decreased below 10 psu at the stations and rates of transport associated with tidal pumping and the mean advection increased. This increase was caused by the advection of the salt wedge and ETM past the stations. In periods where the sites remain stratified, the upstream limit of the salt wedge and the ETM remained upstream of site resulting in lower residual and tidal transport of sediment at those specific sites. This pattern of decreased stratification and increased sediment transport occurred throughout the year across all estuarine regimes.

The patterns of transport in February varied by station, but generally matched those described for the entire year (Figure 29). Total advection was oriented downstream for the vast majority of the month at all stations reaching a maximum during spring tides (partially mixed) and a minimum during neap tides (strongly stratified). Patterns and magnitude of tidal pumping varied by station responding to tidal range and stratification. Higher rates of transport due to tidal pumping were observed at the upstream stations (SATURN-01 and SATURN-03) than the downstream stations (NC01 and SC01) throughout the month, with the highest rates at SATURN-03 during spring tides. Cross-channel transport was small compared to along-channel transport due to the highly channelized morphology of the estuary.

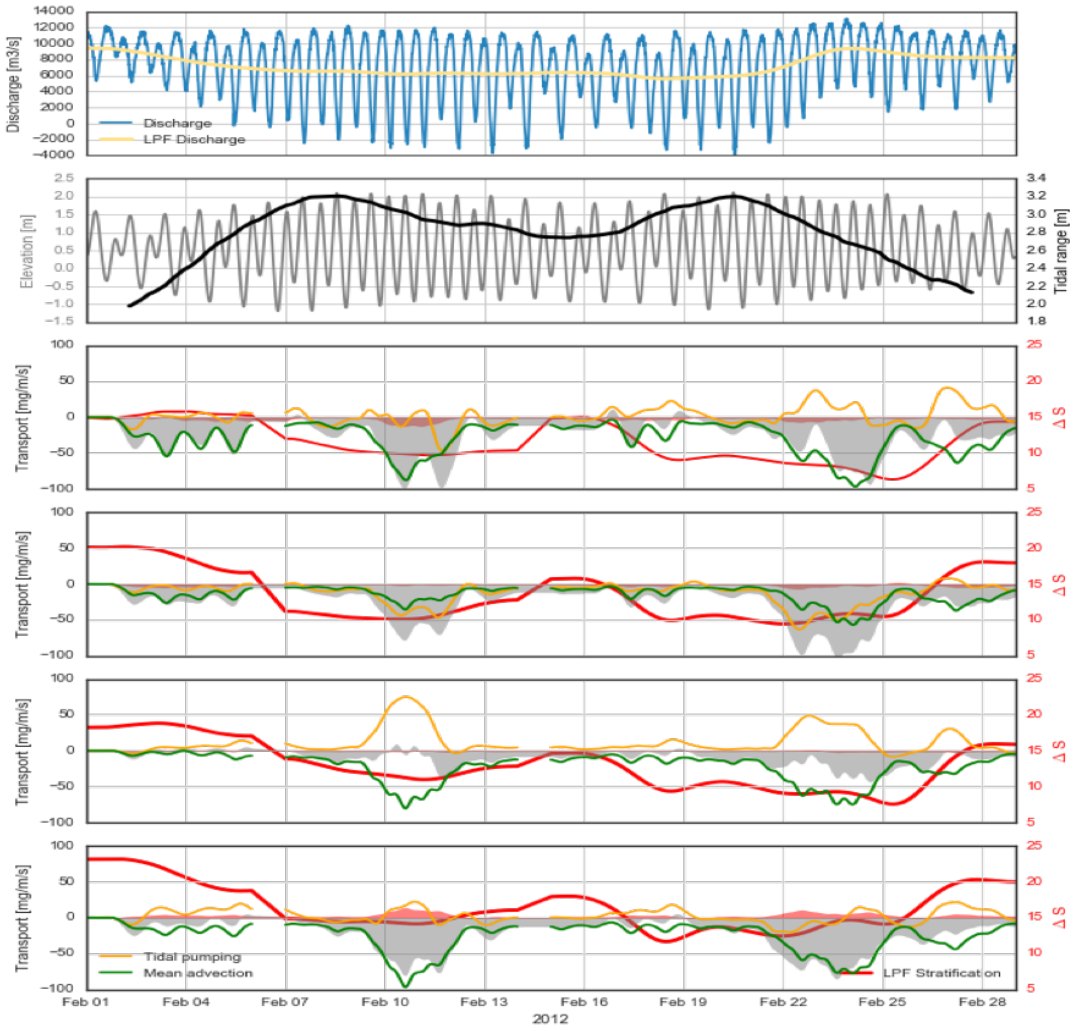

Figure 29 Same as Figure 28 with total along channel sediment flux (gray) and cross-channel flux (red).

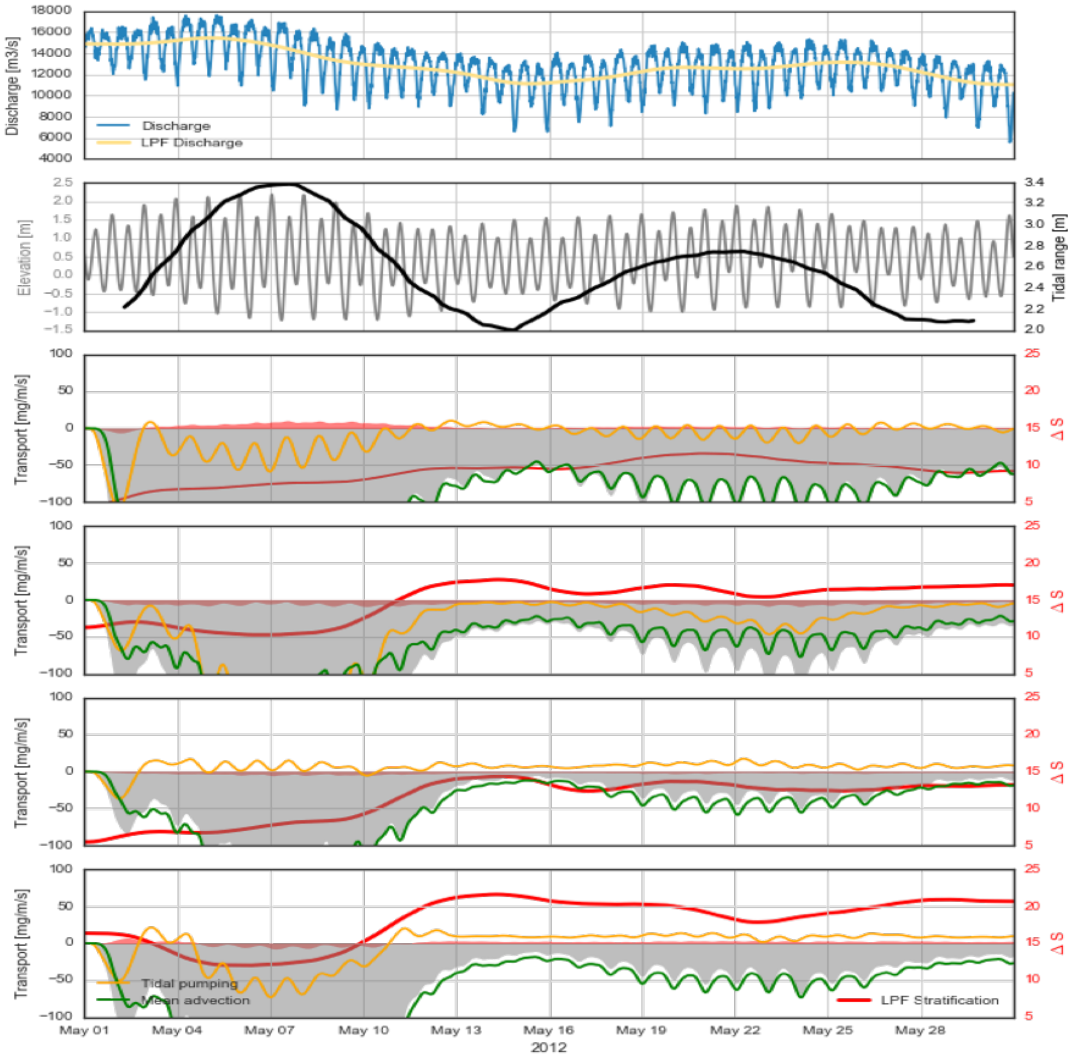

Figure 30 Same as details as in Figure 28 for May.

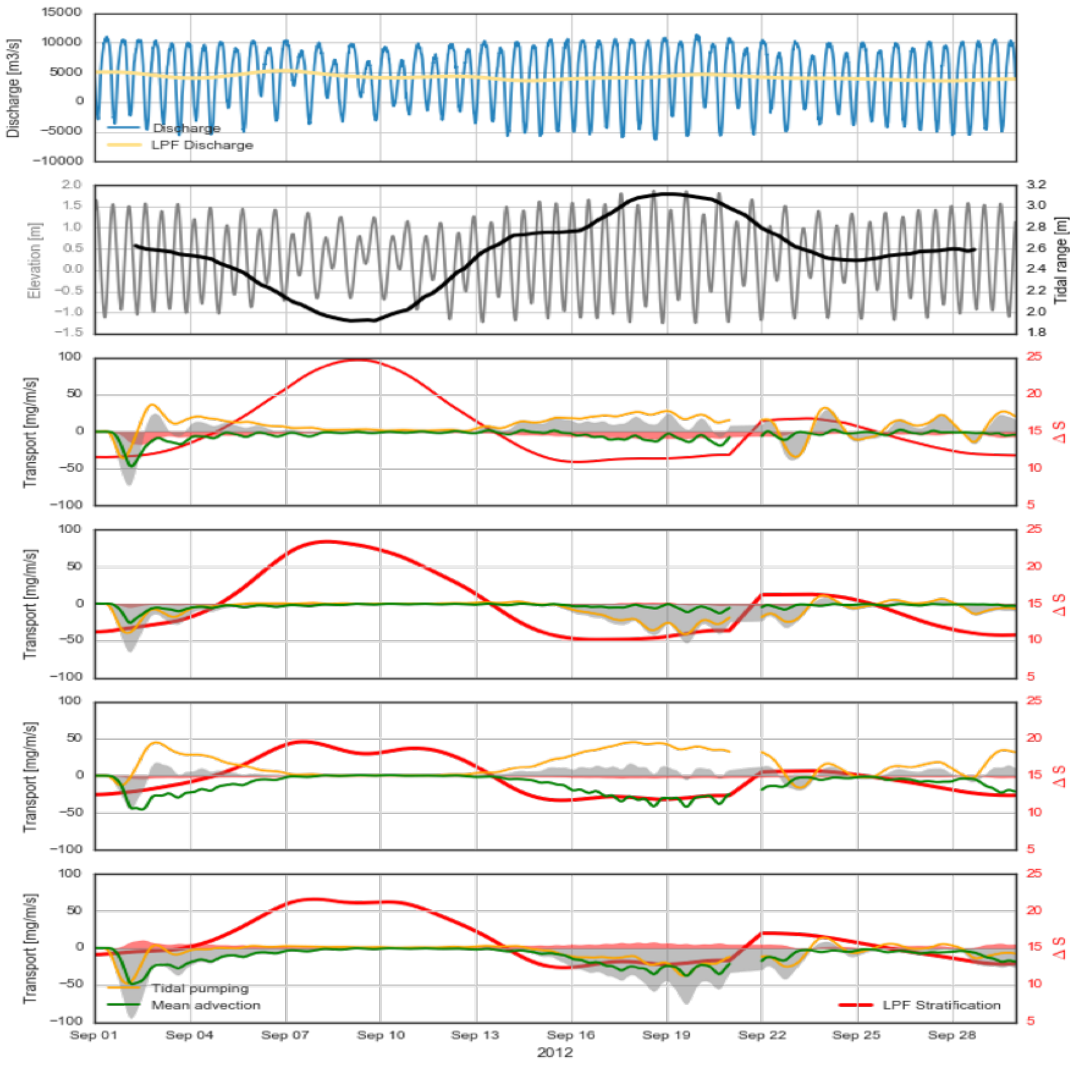

Figure 31 Same as details as in Figure 29 for September.

In May, the high river discharge caused the total transport to reach a maximum for the year exceeding a rate of 150 mg m^{-1} s^{-1} (Figure 30), but still responded to tidal range and stratification in the same manner. In this period, tidal pumping transport in the North and South Channels behaved in distinct manners. Generally, there was higher rates of upstream transport in the South Channel than the North Channel and were oriented upstream for a majority of the time at SC01 and nearly the entire time at SATURN-03. In contrast, tidal pumping at NC01 remained oriented downstream and oscillated in orientation at SATURN-01. During the weaker spring tide, the stratification remained fairly stable even as the tidal range varied. As in the winter period, cross-channel transport was small compared to along-channel transport.

During September, the low river discharge resulted in high stratification throughout the month producing proportional reductions in transport (Figure 31). Total transport reached a minimum at all stations during neap tides when stratification was high. During these periods, there were generally low concentrations of suspended sediment throughout the system and the setup of exchange flow resulted in a near balance of up- and downstream oriented transport. During neap tides, transport was oriented upstream at both upstream stations (SATURN-01 and SATURN-03), but remained oriented downstream at the downstream stations (NC01 and SC01). The upstream orientation of tidal pumping at the upstream stations corresponded with the passing of the ETM on a tidal basis whereas the downstream stations remained in the stratified salt wedge throughout the period.

3.4.3 Sediment transport pathways

The dominant pathways for sediment transport through the estuary are described by region and synthesized in combination with point based fluxes in Figure 32 based on the magnitude of flux through the system integrated over 2012. Although the direction of sediment flux tends to vary in the lower estuary between ebb and flood tides as described in Section 3.4.2, the temporally integrated sediment pathways do not vary by tidal range or river discharge and therefore by estuarine regime. Rather, variations in tidal range and discharge only produce differences in the magnitude of suspended sediment transport.

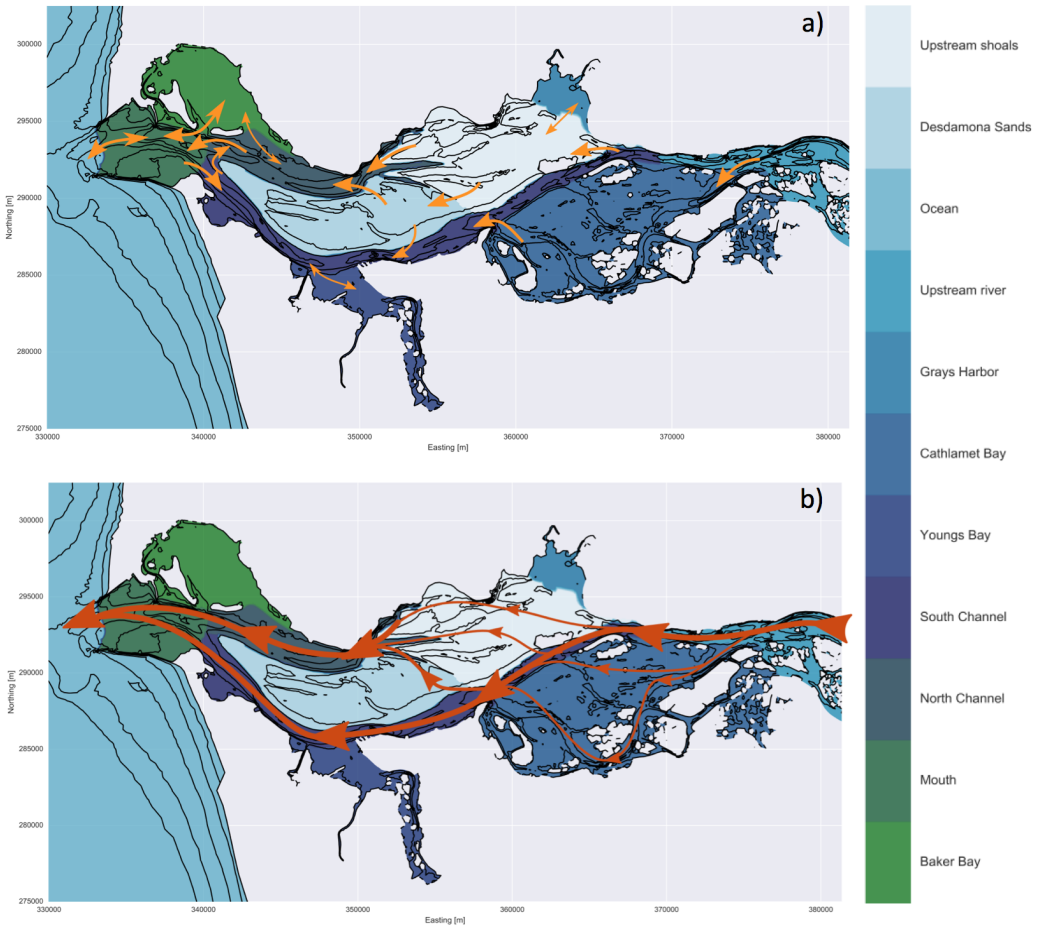

Figure 32 Sediment pathways. (a) Sediment pathways as calculated by flux through entire regions. (b) Dominant sediment pathways synthesized from pointwise flux.

The dominant sediment pathway follows the South Channel through the estuary to the river mouth (~57%) (Figure 32). This pathway has two distinct upstream paths where the fluvial source of suspended sediment is split between the South Channel (~70%) and Cathlamet Bay (~30%). The flux that enters Cathlamet Bay moves through a multitude of channels within the bay eventually rejoining the South Channel.

A secondary pathway traces multiple paths from departing from the South Channel through intertidal shoals to the North Channel and eventually to the mouth (~43%). One such path begins in the South Channel passing through multiple channels in the upstream shoals near Grays Bay before merging into the North Channel. Another pathway follows a series of channels that connect the South Channel and North Channel between Desdemona Sands and upstream shoals (Figure 2). These two paths along with other minor routes converge near SATURN-01 in the North Channel.

Model results suggest moderate infill in Baker Bay and the regular dredging required to maintain the South Channel on the west end of the bay suggests that the model results, at a minimum, reflect the broad deposition patterns in Baker Bay. Similarly, model results in both Youngs Bay and Gray's Bay suggest gradual infill (Figure 32).

3.4.4 The ETM zone

Here the ETM zone is defined as the region of the estuary where ETM pass through in addition to adjacent areas with SSC elevated above fluvial sources. Figure 33 shows the ETM zone as derived from model results from February, May, and September 2012. This region roughly corresponds with maximum intrusion of the

salt wedge, but extends further upstream while the downstream boundary is limited to the area between the jetties near the mouth. Because the ETM zone is linked to salinity intrusion, its size and shape depend on the estuarine regime, and thus on tidal range and river discharge. February and September both occupied partially mixed and strongly stratified regimes, but the ETM zone was larger in September extending further upstream along with the salinity intrusion length due to the low river discharge. In May, during salt wedge and time-dependent salt wedge regimes, the ETM zone was compacted compared to other periods due to the high river discharge.

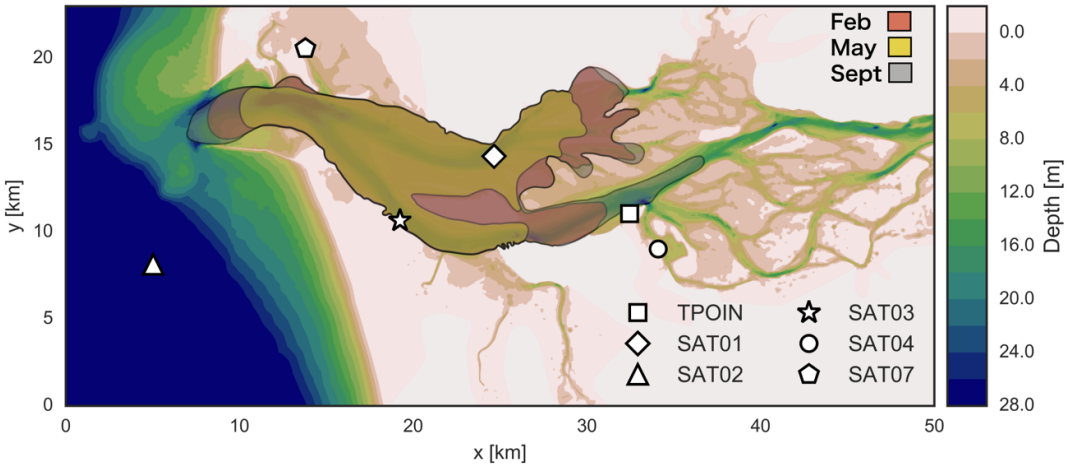

Figure 33 ETM zones, a region of elevated suspended sediment concentrations, by month.

3.4.5 Conceptual model

The previous results and analyses of circulation and sediment dynamics can be synthesized into a new three-dimensional conceptual model of the Columbia River estuary ETM. In this model, we divide the temporal dimension into two high energy periods (ebb and flood tides) and two low energy periods (low and high water slacks) to describe the characteristics and evolution of velocity, mixing, and suspended sediment from plan views of the lower estuary and transects along the channels (Figure 34). Although SSC varies strongly over the year in response to

changes in river discharge, fluvial sediment load and tidal range, the cycle of events represented in this single conceptual model consistently describes sediment and ETM dynamics in the lower estuary from a mechanistic point of view.

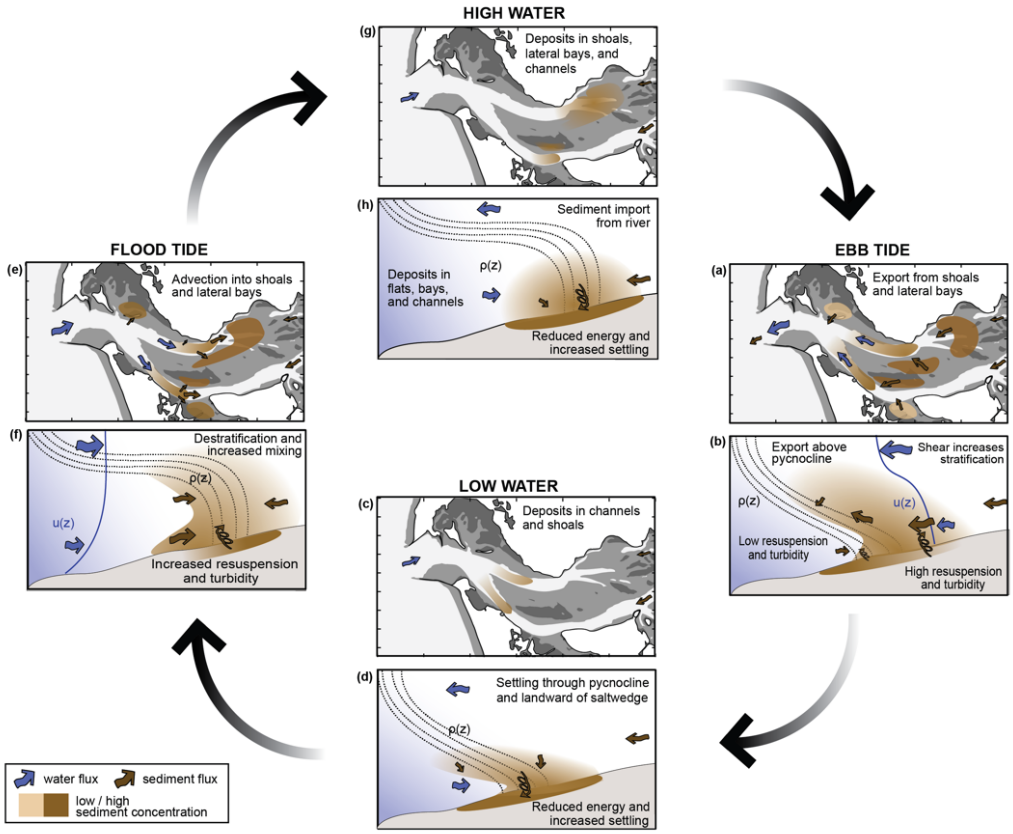

Figure 34 Conceptual diagram of ETM. Plan views of water flux, sediment flux, and suspended sediment concentrations during ebb tides (a), low water stages (c), flood tides (d), and high water stages (g). Idealized transect showing water flux, sediment flux, density isopleths, and velocity along main channels during ebb tides (b), low water stages (d), flood tides (f), and high water (h).

During ebbs, the barotropic pressure gradient overwhelms the baroclinic pressure gradient pushing the salt wedge downstream while generating sufficient shear to progressively mix the water column. The downstream advection of the salt wedge creates three distinct zones: the upstream freshwater zone, the brackish zone above the pycnocline, and the saline zone below the pycnocline in the salt wedge. Currents in the freshwater zone are sufficient to erode bed material along the

entirety of estuary. The eroded bed material joins the fluvial suspended sediments, and the combined materials are advected downstream in concentrations much higher than the fluvial source. Near the upstream limit of salinity intrusion, in the vicinity of the convergence of currents, the majority of water and suspended sediment flows over the pycnocline into the brackish zone above the salt wedge becoming the SSP described in Section 3.3.4. In the North Channel, the convergence of suspended sediment from multiple pathways described in Section 3.4.3 produces higher concentrations of suspended sediment above the pycnocline than within the salt wedge. Due to the suppression of mixing in the pycnocline, the suspended sediment settles out of the surface layer through the pycnocline into the lower saline layer. In this bottom layer, the currents remain directed upstream along the majority of the salt wedge for a large part of the ebb. The sediment that settled through the pycnocline from the upper layer accumulates with newly eroded sediment produced by the upstream oriented currents generating elevated concentrations. As low-water slack approaches, currents in all three zones decrease, limiting shear and mixing, and allowing suspended sediment to deposit into easily erodible bed materials.

As the surface elevation increases from the ocean early in the flood, the barotropic and baroclinic pressure gradients work in unison to generate upstream currents over a substantial part of the water column near the mouth, forcing the intrusion of the salt wedge into the estuary. The incoming currents generate sufficient near-bed stress to erode the sediment that had just deposited during the previous ebb and slack; within the progressing salt wedge, the pycnocline traps the newly eroded material. The sediments trapped below the pycnocline constitute the classical flood ETM. Upstream of the salt wedge, a SSP leads the intrusion of

salinity which spreads towards the surface because it is uninhibited by stratification. The concentrations in the SSP are much lower than those in the ETM, but above fluvial sources. The incoming currents push both the SSP and the ETM upstream along channels and into shoals while simultaneously eroding bed material, thereby adding to the SSC within the patches. The net effect is sediment transport upstream characterized and quantified as tidal pumping in Section 3.4.2. As high water slack approaches and the currents slow, the patches of suspended sediment settle in the channels and shoals becoming easily erodible source material for the SSP during the next ebb.

3.5 Discussion

Within the limits of model skill, our simulations offer insight into the variability of suspended sediment dynamics in the Columbia River estuary. Model results confirm, extend, or contextualize aspects of the SSC variability on a tidal to seasonal basis in response to the currents and density structures generated in the estuary by tidal and river forcing—consistent with prior observational and modeling findings (Fain et al., 2001; Gelfenbaum, 1983; Jay & Musiak, 1995; Jay & Musiak, 1994; Reed & Donovan, 1994; Sherwood et al., 1990). For comparable river discharges, SSC is larger during spring tides, when the tidal range is largest and tidal currents are fastest, and smaller during neap tides, when stratification increases but tidal currents are slower (Fain et al., 2001; Jay & Musiak, 1995; Reed & Donovan, 1994). Over the course of a year, SSC in the estuary, like that at Beaver Army in the upstream portion of the river (Figure 14), is highest during the spring freshet, when river discharges and upstream sediment loads are highest, but can be nearly as high in winter after large storms; by contrast, SSC is lowest during the

low-flow period of the late summer and early autumnal months. From an estuarine regime perspective, highest SSC is found in the time-dependent salt wedge regime (high river discharges and sediment loads, and large tides) and decrease through the salt-wedge, partially mixed, and strongly stratified regimes (i.e., as either or both tidal ranges and river discharges decrease). In contrast to the observations reported by *Sherwood et al.* (1990a), but in agreement with observations from CMOP research cruises, simulations suggest higher SSC in the North Channel than in the South Channel for most of the year; the exception is during the Spring freshet when high SSC upstream of is associated with large river flux in agreement with observations from the CRETM-LMER project (Simenstad et al., 1994).

Within the two main channels of the estuary, suspended sediment dynamics are dominated by ETMs that occur near the upstream limit of the salt-wedge. The tides advect the ETMs up and down the main channels, producing elevated SSC at static locations roughly on a quarter diurnal frequency (Fain et al., 2001; Gelfenbaum, 1983; Reed & Donovan, 1994) . Previous studies established a correlation between observed velocity shear and suspended sediment stratification at the M_4 frequency, and suggested that internal tidal asymmetry was the mechanism that balanced the dominant downstream transport of fluvial sediment, resulting in the maintenance of the ETM (Jay & Musiak, 1995). With the benefit of a synoptic perspective, our simulations suggest that tidal advection of the ETM is the primary mechanism balancing the downstream fluvial transport. Both simulations and observations shown here suggest that tidal-scale variability in stratification is also an essential mechanism in the Columbia River estuarine sediment dynamics, contributing to both the trapping of the flood ETM below the pycnocline and to the

advection of the SSP over the salt wedge, in a manner similar to the dynamics described by *Geyer* (1993) and extended by *de Nijs & Pietrzak* (2012).

The ETM in the North and South channels have similar characteristics, dynamics, and response to changes in forcings. However, the North Channel ETM is influenced by interactions with adjacent shoals and South-North transfers of sediments along a complex network of secondary channels; by contrast, the South Channel ETM results primarily from in-channel dynamics and is more sensitive to variability in river discharge. Both ETMs occur in a region roughly collocated with the maximum excursion of the salt wedge, and inclusive of main and secondary channels as well as intertidal shoals, characterized by concentrations of suspended sediments above riverine source levels. Within the ETM zone, sediments cycle through tidally-controlled phases of erosion, advection, settling, and deposition, and are subject to a multitude of physical processes that result in the trapping of materials as described in a new conceptual ETM/SSP model. The SSP that occur in the North Channel during ebb tides is a prominent feature of the ETM zone, which has been anecdotally observed earlier but was first linked to the ETM in the companion work of *Lopez & Baptista* (2016a). SSC in the ETM zone vary with tidal range and river discharge; but the concentrations are higher and dynamics are strongly influenced by local stratification, topography, tidal phase, and location relative to the upstream limit of salinity intrusion.

Compared to literature in different systems, the conceptual model presented here is similar to that proposed by *de Nijs & Pietrzak* (2012) for the Rotterdam Waterway with notable differences in the relative importance of baroclinic and barotropic currents and asymmetry in each system. As in *de Nijs & Pietrzak* (2012), we find that the trapping of sediment is fundamentally driven by tidal

processes dictating local currents, stratification, and ,therefore, erosion and settling. The decomposition of sediment fluxes in our analysis is similar to that of *Kärnä & Baptista* (2016) for Columbia river salinity fluxes, and to the decomposition of sediment fluxes of *McSweeney et al.* (2016) and *Becherer et al.* (2016). Unlike *McSweeney et al.* (2016) and *Becherer et al.* [2016], though, we find the magnitude of tidal pumping to be much lower than mean advection for the majority of the year; only under certain conditions, particularly when the estuary is in a partially mixed regime as in February and September, is tidal pumping sufficiently strong to generate net upstream flux of suspended sediment. The highly channelized flow in the Columbia River renders along channel processes dominant, in contrast to the findings of *McSweeney et al.* (2016). However, all model results and observations suggest that lateral processes add to the convergence of suspended sediment in the North Channel from adjacent shoals in a manner distinct from the South Channel.

3.6 Conclusions

Suspended sediment concentrations in the Columbia River estuary are modulated at tidal, tidal month, and seasonal scales through interactions between tides, river discharge, and fluvial sediment loads. The transport of sediment through the estuary is dominated by along-channel mean advection, with tidal pumping producing local net upstream transport during partially mixed regimes. The two dominant pathways of suspended sediment transport follow the main channels with secondary pathways through Cathlamet Bay and intertidal shoals that converge in the North Channel. An ETM zone, a region of residually elevated suspended sediment through which two ETMs migrate (and occasionally merge),

is roughly collocated with the limit of salinity intrusion. The ETM zone acts as local source and temporary sink for sediment, and includes, besides the main ETM features, periodic patches of elevated SSC that interact with the salt wedge. Both ETMs and sediment patches result from a repeatable pattern of erosion, transport, settling and deposition, involving the main channels, intertidal shoals, and lateral bays, and occur in response to the phases of the prevailing mixed semi-diurnal tides.

4 LIGHT ATTENUATION MODEL

4.1 1 Introduction

Light attenuation is ecologically important in marine systems, playing major roles in prey-predation relationships (Bottom et al., 2005), photochemistry (Smith & Benner, 2005), primary productivity (Kirk, 1994), and, therefore, ecosystem function (Häder et al., 2006). System-wide characterizations of light attenuation and euphotic zone depth, the depth where photosynthetic available radiation (PAR) is attenuated to 1% of its surface value, are therefore important in describing and understanding estuarine aquatic environments and biogeochemistry. But the comprehensive data required for these characterizations is challenging to collect—and thus relatively rare—in dynamic aquatic systems, especially in highly varying estuaries. The advent of modern endurance observation networks and numerical models, offer new opportunities in this regard. Conversely, improved characterizations of light attenuation and euphotic depth may enable improved modeling of heat balances and biogeochemical cycling.

Four major factors contribute to light attenuation, through either or both

absorption and scattering (Kirk, 1994): The water itself absorbs light (transforming its energy into heat) in the red band of the visible spectrum; suspended inorganic particles (sediments) that often dominate turbidity strongly scatter light, giving the water a brown hue; phytoplankton both strongly scatters light and absorbs it in the green and blue bands; and colored dissolved organic material (CDOM) absorbs light strongly especially in the blue spectrum, giving the water a yellow hue (Davies-Colley & Nagels, 2008).

Through a combination of these factors, light irradiance (the flux of radiant energy per unit area) decreases exponentially with water depth, i.e.:

$$I(z) = I_0 e^{-K_d z} \tag{18}$$

where $I(z)$ is the downwelling irradiance at depth z, I_0 is the downwelling irradiance just below the surface, and K_d is the light attenuation coefficient. This coefficient is defined as:

$$K_d = -\frac{\ln (I_1/I_2)}{\Delta z} \tag{19}$$

where I_1 and I_2 are the irradiance at two depths separated by a vertical distance Δz (Kirk, 1994). The euphotic depth is thus defined as

$$z_{1\%}(K_d) = \frac{-\ln(0.01)}{K_d} \tag{20}$$

where K_d refers in this case only to the light spectrum in the photosynthetically active range (PAR), and is commonly referred to as the diffusive light attenuation coefficient.

These characterizations of light behavior in aquatic environments, coupled with the emergence of increasingly common in-situ measurements of turbidity, chlorophyll *a*, and CDOM, provide a convenient means of describing K_d as a linear

combination of the primary light attenuation factors in the water (Gordon, 1989). Baker & Smith (1982) developed an early model exploring this convenience in the form

$$K_d = K_w + K_P[P] + K_x \quad (21)$$

where K_w is the attenuation coefficient of water, K_p is the attenuation coefficient per unit of concentration of chlorophyll [P], and K_x is the attenuation coefficient due to all other suspended and dissolved materials in the water. *Kirk* (1994) later developed a similar model where K_x was decomposed into two components, leading to

$$K_d = K_w + K_p[P] + K_{SPM}[SPM] + K_C[CDOM] \quad (22)$$

where K_{SPM} is the attenuation coefficient per unit of the concentration of suspended particulate matter ([SPM]) and K_c is the attenuation coefficient per unit of the concentration of CDOM ([CDOM]). With a modeling application in view, *Xu et al.* (2005) developed a model of the form

$$K_d = K_w + K_p[P] + K_{SPM}[SPM] + K_sS \quad (23)$$

where K_s is the attenuation coefficient per unit of salinity (S). Salinity was used in place of CDOM because the two are very highly correlated and salinity is easier to use as a direct output from numerical models.

In this study we describe the development of an empirically derived predictive model for K_d, specifically defined as the diffusive light attenuation coefficient for PAR, from in-situ measurements of CDOM, chlorophyll *a*, turbidity, and PAR from the Columbia River estuary. Outputs of salinity and suspended sediment concentrations from a numerical model of the estuary are then applied to the light attenuation model to provide three-dimensional time-dependent system-wide

estimates of K_d. Estimates of K_d are used to develop system-wide maps identifying spring-neap and seasonal trends of K_d and euphotic depth. Finally, the empirically derived model for K_d is implemented in SELFE. The effects of the temporally and spatially varying K_d in the radiative heat transfer function on circulation are assessed using predicted temperature skill as the evaluating metric.

4.2 Methods and models

4.2.1 Setting: The Columbia River estuary

The Columbia River is the second largest river by discharge in the United States and is the largest single source of fresh water to the Northeast Pacific Ocean. The Columbia River estuary has two main channels (North and South) with characteristic depths of 20 m separated by intertidal shoals and is flanked by four lateral bays. The estuary features tides are mixed, semi-diurnal ranging from less than 2.0 m to over 3.5 m and receives river discharge varying from 3,000 $m^3\ s^{-1}$ during low flow conditions up to 20,000 $m^3 s^{-1}$ during large freshets with an average of 7,000 $m^3\ s^{-1}$ (Chawla et al., 2008). The main stem of the Columbia River and its tributary Willamette River are the two dominant sources of fresh water to the estuary, each with distinct hydrographs and profiles of carried material. The Columbia drains an enormous, mostly arid, stretch of North America whereas the Willamette drains the narrow, wet region west of the Cascades in Northern Oregon. Peak discharge in the Willamette occurs during large winter storms and can exceed 7,000 $m^3\ s^{-1}$ providing a large periodic pulse to the Columbia at a time it typically experiences flows below 4,000 $m^3\ s^{-1}$. The large range of tidal and river forcings causes the Columbia River estuary to migrate in estuarine parameter space from partially-mixed to strongly stratified during low

flow periods and between salt wedge and time-dependent salt wedge during high flows (Kärnä et al., 2015; Stramska & Dickey, 1998).

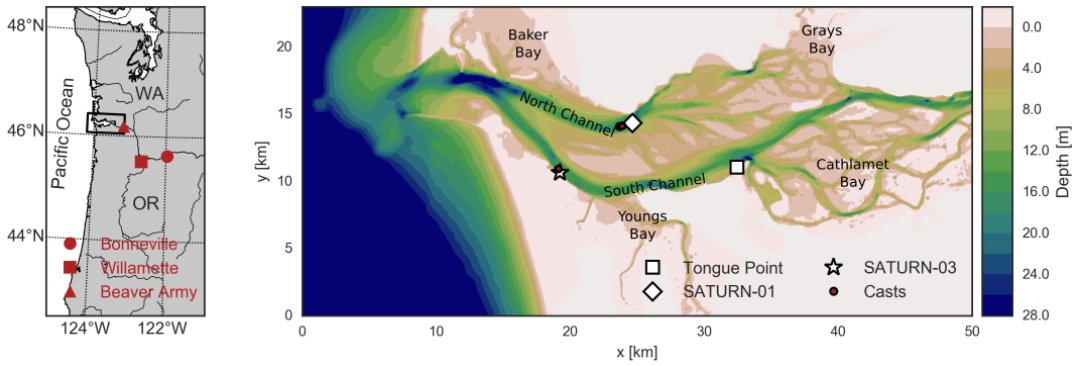

Figure 35. The Columbia River estuary. (A) Location of the Columbia River estuary relative to the Pacific NW, USA. (B) Close up of the estuary with white filled markers indicating permanent moorings and red filled markers indicating locations of cruise casts. Named features (channels and lateral bays) will be referred to in the text.

4.2.2 Empirical estimation of the diffuse light attenuation coefficient

Our goal was to develop an empirical model describing the relationship between the diffuse light extinction coefficient, K_d, and commonly measured water quality variables in the Columbia River estuary. Following a methodology already adopted by several others (e.g. Baker & Smith, 1982; Davies-Colley & Nagels 2008; Gallegos & Moore, 2000; Kirk, 1994; Xu et al. 2005), in-situ measurements of PAR were used to derive K_d and concurrently measured, co-located turbidity, chlorophyll *a*, and CDOM were used to derive the attenuation coefficients for each constituent using linear models.

In-situ measurements were collected from 25 CTD casts from a research cruise aboard the *R/V Oceanus* in the Columbia River between 25 September and 1 October, 2015. Chlorophyll *a* and CDOM were measured with WetLabs ECO fluorometers, turbidity with a WetLabs NTU, and PAR with a Licor LI-193 spherical underwater quantum sensor. Data from each cast was aggregated and processed with calibration coefficients to provide observations in units of mg m^{-3} for

chlorophyll *a* and CDOM, μmol m^{-2} s^{-1} for PAR, and NTU for turbidity.

K_d was calculated over the euphotic zone using the relation described by *Kirk* (1994)

$$K_d = \frac{\ln\left(\frac{PAR_{ed}}{PAR_{sur}}\right)}{z_{1\%} - z_{sur}} \tag{24}$$

where PAR_{ed} is the PAR at the euphotic depth ($z_{1\%}$) and PAR_{sur} is the PAR at the surface (z_{sur}). For each cast, PAR_{sur} was estimated from an average of the observed PAR over the minute immediately preceding the cast. Equation (3) was then used to calculate $z_{1\%}$ for the cast, and PAR_{ed} was computed at that depth by interpolation of neighboring observations.

Figure 36 maps K_d against estimates of chlorophyll *a*, CDOM, turbidity and salinity obtained by averaging the observations collected for the cast throughout the euphotic zone. Correlations of K_d with linear combinations of these primary variables explored using dependencies developed by other researchers: with turbidity and CDOM (Davies-Colley & Nagels, 2008); turbidity, CDOM and chlorophyll *a* (Kirk, 1994); and turbidity, chlorophyll *a*, and salinity (as a surrogate for CDOM) (Xu et al., 2005).

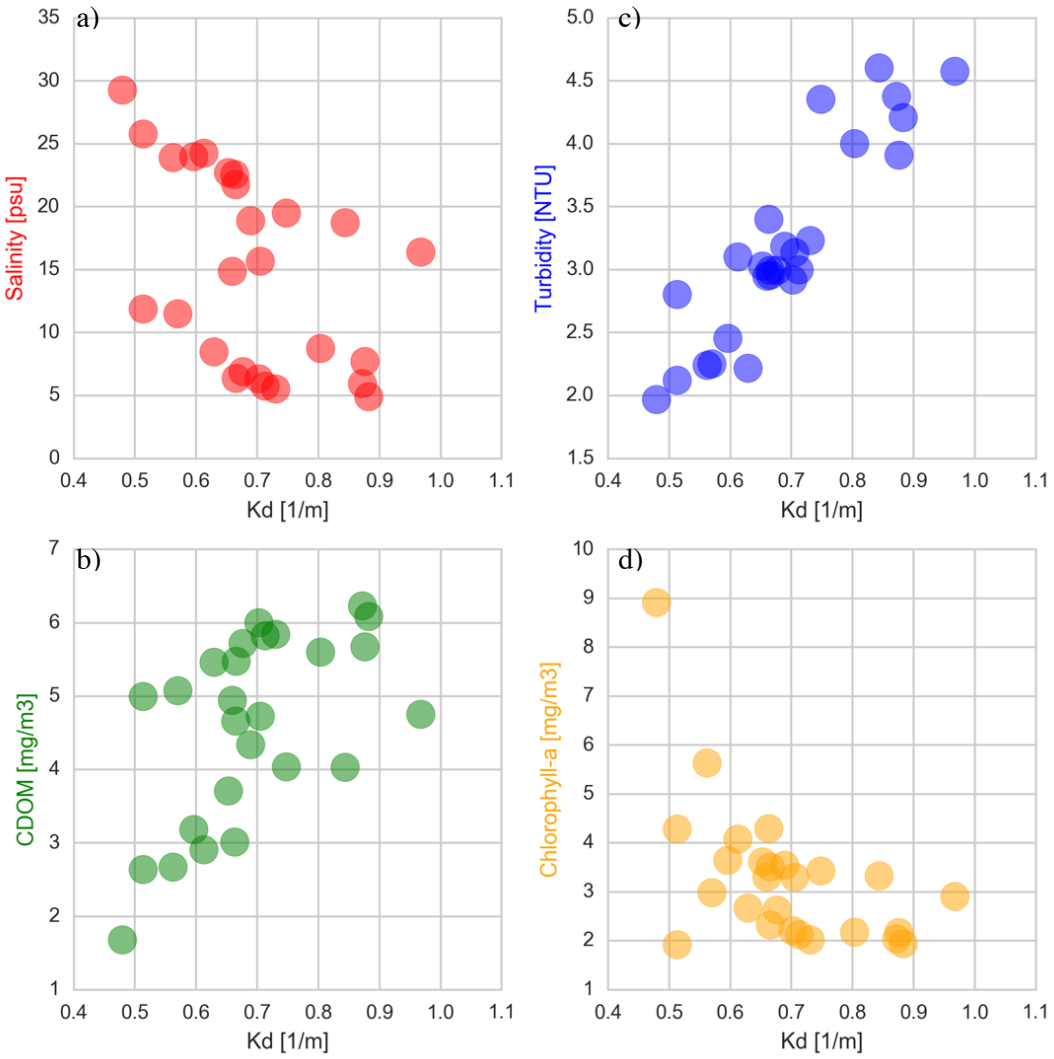

Figure 36 Plots of *Kd* versus independent variables used in model development. (A) Salinity, (B) turbidity, (C) CDOM, and (D) chlorophyll *a* were averaged over photic zone during cast.

In addition, we also explore a correlation of K_d with just turbidity and salinity, i.e.

$$K_d = K_w + K_t NTU + K_{Salt} S \tag{25}$$

using the hypotheses that for the Columbia River estuary (a) salinity can serve as a surrogate for CDOM (as in Xu et al. (2005)), and (b) chlorophyll *a* has a second order effect relative to turbidity and CDOM (as in Davies-Colley & Nagels (2008)). In this equation, K_t is the attenuation coefficient for turbidity (NTU), and K_{Salt} is the attenuation coefficient for salinity.

4.2.3 Numerical model

The model used in this study is the three-dimensional unstructured-grid model SELFE (Lopez & Baptista, 2016a; Zhang & Baptista, 2008). The model solves the Reynolds-averaged Navier-Stokes equations using Boussinesq and hydrostatic assumptions in a finite-element framework. The semi-Lagrangian Eulerian-Lagrangian Method is used to solve for momentum and transport is solve d using a finite volume upwind method. The governing equations are closed using the *k-ε* turbulence closure model from the GOTM library (Umlauf & Burchard, 2005).

Model grid and circulation parameters have been developed and tested in *Kärnä & Baptista* (2016) and *Kärnä et al.* (2015) and match the choices of *Lopez & Baptista* (2016). The model domain included the Pacific Ocean from Vancouver Island (~50° N) to the coast of Northern California (~40° N) stretching approximately 300 m off the coast (~128° W) and focused most of the grid resolution in the Columbia River estuary, where the domain extends 85 km upstream from the mouth to the Beaver Army Terminal (Figure 35). The vertical grid consisted of 54 vertical levels, 17 Z-levels used in depths greater than 100 m and 34 S-levels in shallower depths. In reaches of the domain less than 30 m deep, which includes the vast majority of the estuary, the vertical levels reverted to sigma-layers. Downward irradiation was attenuated using a static uniform Jerlov parameterization (R=0.8, λ_1=0.9, λ_2=2.1) of the *Paulson & Simpson* (1977) formulation

$$I(\mathrm{z})=\mathrm{I_o}R\left(\mathrm{e}^{-\frac{\mathrm{z}}{\lambda_1}}\right)+(1-R)\left(\mathrm{e}^{-\frac{\mathrm{z}}{\lambda_2}}\right) \tag{26}$$

where R is the fraction of irradiance that does not penetrate the thin surface layer of water, and λ_1 and λ_2 are extinction depths corresponding to Jerlov water type parameterization. The first term corresponds to the rapid attenuation of red light

near the surface and the second term corresponds to the attenuation of blue and green light below the surface layer (Paulson & Simpson, 1977).

A uniform bottom roughness (z_0 = 0.0001 m) was applied to maximize salinity intrusion based on previous sensitivity analysis (Kärnä et al., 2015). Atmospheric boundary conditions were imposed from NARR hindcasts (Mesinger et al., 2006). Ocean boundaries were forced with temperature, salinity, and sub-tidal elevations from NCOM hindcasts (Barron et al., 2006) and by tides defined from eight tidal constituents (O_1, K_1, Q_1, P_1, K_2, N_2, M_2, S_2) obtained from a regional inverse model (Myers & Baptista, 2001). River discharge (Figure 37) and temperature were imposed from USGS observations at Beaver Army Terminal (USGS #14246900).

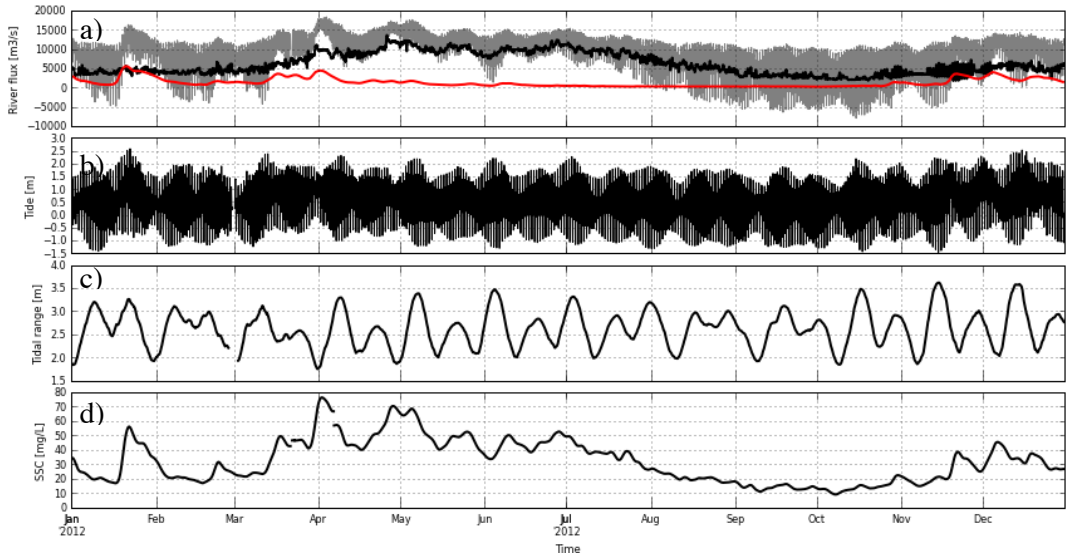

Figure 37 River forcing and tides for the Columbia River estuary in 2012. (A) River discharge at Beaver Army Terminal (grey), Bonneville Dam (black), and Willamette River (red). (B) Tidal elevation at Tongue Point. (C) Tidal range at Tongue Point. (D) Estimate of SSC [mg/L] from rating curve based on low-pass filtered discharge at Beaver Army Terminal.

The sediment model was parameterized as in *Lopez & Baptista* (2016). The parameterization included four non-cohesive sediment classes corresponding to clay, fine silt, silt, and sand sized classes based on observations (Fain et al., 2001; Reed & Donovan, 1994). The bed prescription is dominated by the sand size class

(>= 90%) with minor percentages of the other smaller classes based on previous descriptions of the bed composition (Fox et al.,1984; Sherwood et al.,1990). Boundary conditions for suspended sediment concentrations are based on a rating curve derived from observations of turbidity from the SATURN Observatory (Baptista et al., 2015) and water samples of suspended sediments by the USGS at Beaver Army Terminal (USGS #14246900). Additional details are described in Table 11.

Table 11 Sediment model parameters used for simulations of the Columbia River Estuary.

Variable	Wash	Fine Silt	Silt	Sand
Median diameter [mm]	0.01	0.03	0.06	0.125
Settling velocity [mm/s]	0.05	0.05	2.0	10.0
Erosion rate [kg/m^2/s]	1.0 x 10-5	1.0 x 10-4	1.0 x 10-4	1.0 x 10-3
Critical stress [Pa]	0.10	0.15	0.15	0.2
Porosity	0.65	0.60	0.55	0.50
Bed initial conditions [%}	0.05	0.10	0.10	0.75
Boundary conditions [%]	0.10	0.20	0.20	0.50

4.2.4 Hybrid model

To create system-wide, time-dependent estimates of K_d we combined SELFE outputs with the light extinction empirical model in a four-step process: [1] simulations of circulation and sediments conducted by *Lopez & Baptista* (2016) were used to create system-wide descriptions of salinity and suspended sediment concentration (SSC) for 1 January through 31 December 2012; [2] SSC was

transformed to turbidity using an empirical correlation (see below); [3] Equation 8, fitted for the Columbia River (Section 3.1), was used to transform salinity and sediment fields into model derived three-dimensional system-wide and time dependent K_d fields; and [4] Equation 3 was then used to estimate the euphotic depth throughout the estuary.

For step [2], suspended sediment in kg m^{-3} were transformed to turbidity (NTU) units using the correlation ($R^2 = 0.72$):

$$SSC = 2.16\ NTU^{1.26} \tag{27}$$

which was developed from observational data for the Columbia River (Lopez & Baptista, 2016a).

4.3 Results

4.3.1 Selection of empirical K_d model

Of the large number of linear models to predict K_d that were explored. Table 2 defines eight and shows their calculated coefficients and R^2 values. Single variable correlations (models A-D) highlight the dominance of turbidity ($R^2 = 0.82$, versus R^2 below 0.32 for each of the other variables) in explaining K_d. All multi-variable correlations (models E-H) have R^2 in the 0.85-0.87 range, consistently outperforming published results with similar approaches for the Chesapeake ($R^2 = 0.58$ in Xu et al., 2005) and underperforming those developed for New Zealand rivers ($R^2 = 0.96$ in Davies-Colley & Nagels, 2008).

The part of the variability of K_d. that remains unexplained by the various multi-variable models is likely due to a combination of factors that we could not integrate in the analysis. For instance, the distribution and composition of

suspended particulate material in the Columbia River estuary shifts substantially based on tidal range between phases of the tide (Fain et al., 2001; Reed & Donovan, 1994). Specifically, the organic component of suspended particulate material increases and the relative amount of fine inorganic sediments decreases during flood tides presumably due to flocculation. During ebb tides inorganic particle grain size increases and particle aggregation decreases (Reed & Donovan, 1994). Adding additional complexity, optically derived estimates of turbidity vary based on particle composition and shape (Davies-Colley & Nagels, 2008).

Table 12. Linear models developed to predict Kd.

Model	Model Form	R^2
A	$K_d = 0.21 + 0.15*NTU$	0.82
B	$K_d = 0.41 + 0.06*[CDOM]$	0.32
C	$K_d = 0.83 - 0.04*[P]$	0.29
D	$K_d = 0.80 - 0.008*S$	0.23
E: Based on Kirk (2004)	$K_d = 0.025 + 0.015*[P] + 0.14*NTU + 0.04*[CDOM]$	0.87
F: Based on Xu et al. (2005)	$K_d = 0.2804 + 0.006[P] + 0.143*NTU - 0.004*S$	0.86
G: Based on Davies-Colley and Nagels (2008)	$\log_{10}(K_d) = -1.25 + 0.595*NTU + 0.13*[CDOM]$	0.85
H: Equation (25)	$K_d = 0.322 + 0.133*NTU - 0.004*S$	0.86

Of the multi-variable empirical models in Table 2, three are adapted from other researchers' work. Of those, model E (based on *Kirk* (1994)) using turbidity, chlorophyll *a*, and CDOM has the highest R^2 (0.87) and thus describes the most variability of K_d. However, replacing CDOM by salinity (model F, based on *Davies-Colley & Nagels* (2008)) or ignoring chlorophyll *a* (model G, based on (Xu et al., 2005)) introduce only a minor skill penalty (R^2 of 0.86 and 0.85, respectively). Furthermore, model H (Equation (25) where the independent variables include only turbidity and salinity describes variability with similar skill ($R^2 = 0.86$).

Relative to the intended use of the empirical K_d model in combination of SELFE, model H is the most convenient, and will be adopted here. For this model, the only

conversion needed from the SELFE's native variables is SSC into turbidity, a conversion that is relatively well established for the Columbia River ((27). The other models require in addition either or both empirical relations between: 1) salinity and CDOM, and 2) salinity and chlorophyll *a*. While salinity and CDOM are tightly correlated, the relationship between salinity and chlorophyll *a* is very non-linear. Even when transforming both independent and dependent variables, $R^2 = 0.72$ is the best skill we could develop; more problematic is that even in this case high concentrations of chlorophyll *a* are poorly captured at high values of salinity.

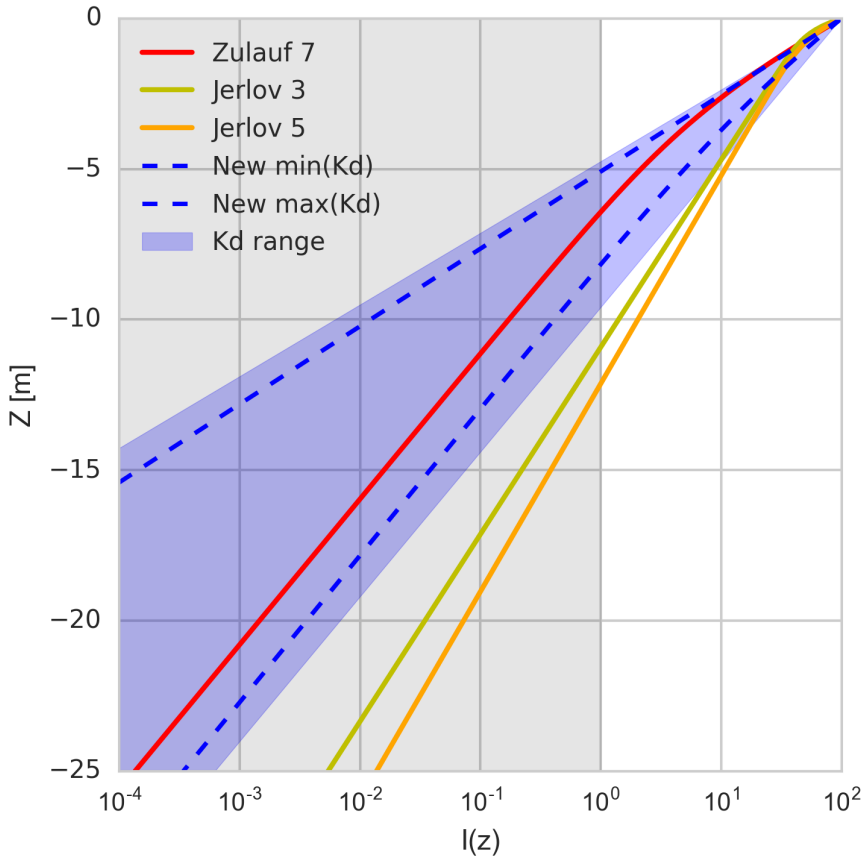

Figure 38. Comparison of different treatments of light attenuation, over a depth range commonly found in the main channels of the Columbia River. Light attenuation for parameterizations of the Paulson & Simpson (1976) algorithms are referred to as Zulauf 7, Jerlov 3 and Jerlov 5 (see text for details), and are represented by single lines. Light attenuation from observations (Kd range) and from Model H (New min(Kd) and New max(Kd)) are expressed as ranges.

4.3.2 System-wide K_d fields

The three-dimensional K_d estuarine turbidity maxima (ETM), a dominant sedimentary feature which has long been recognized in the Columbia River estuary (Jay & Musiak, 1994) and which has recently been simulated in detail by Lopez and Baptista. The largest attenuation coefficients occur at the ETM, creating a local vertical stratification with largest K_d near the bottom. But stratification of light attenuation in the channels is also driven by the intrusion of less turbid ocean water during flood tide, resulting in this case in smaller K_d values near the bottom.

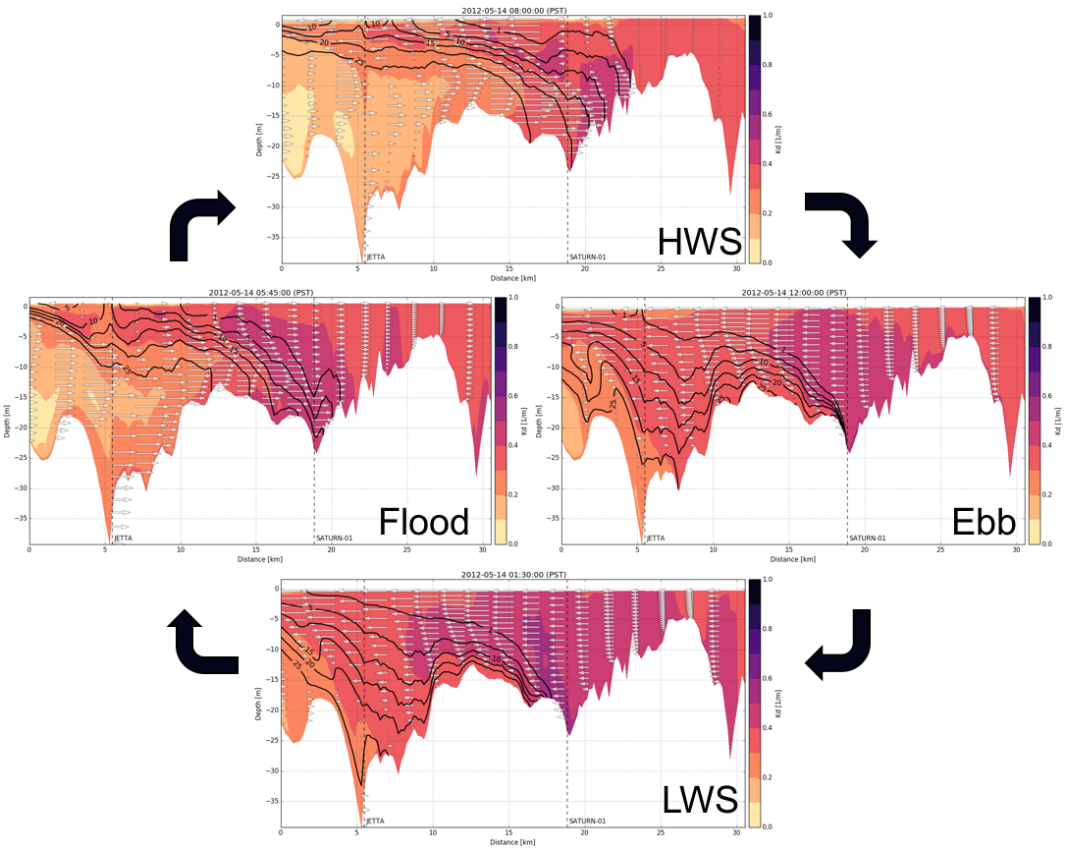

Figure 39. Vertical distribution of Kd along the thalweg of the North Channel over a tidal cycle during May.

Integrating K_d over the depth of the euphotic zone and over specific tidal cycles across different discharge conditions offers important system-wide perspectives on variability, and identifies regions of distinct light attenuation behavior (Figure

40). The figure specifically shows the averaged K_d for selected spring and neap tides in February, May and September of 2012. The different months correspond to high (May), moderate (February), and low (September) river discharges and fluvial sources of suspended sediment concentration (Figure 37). The K_d fields respond strongly to both river forcing and tidal range, which drive the system-wide distributions of suspended sediments and salinity (Kärnä & Baptista, 2016; Lopez & Baptista, 2016a).

Outside the influence of the plume, the coastal region has values of K_d close to pure seawater (~0.3 m^{-1}), consistent with the prevailing low concentrations of suspended sediment. By contrast, in the plume-affected region just outside the mouth, the values of K_d are higher (~0.4 m^{-1}), reflecting the export of estuarine sediment and CDOM via the plume. The highest values of K_d ($\geq$ 0.6 m^{-1}) are found in the extensive and turbid intertidal shoals of the main stem estuary, which are major suppliers of sediment to the ETM. The estuary's mouth and the North and South Channels, which are periodically exposed to intruding high salinity and low sediment ocean waters, stand out as slivers of lower K_d within the main stem (~0.18 – ~0.8 m^{-1}), despite being the loci of the highly mobile ETM. The brackish bays closest to the mouth (Baker Bay and Youngs Bay) have higher K_d values ($\geq$ 0.4 m^{-1}) than the mouth and main channels. The mostly freshwater and often more turbid bays further upstream (Grays Bay and Cathlamet Bay) have generally higher values of K_d ($\geq$ 0.4 m^{-1}), although lower than those for the intertidal shoals of the main stem. However, parts of the western edge of Cathlamet Bay have the lowest values of K_d (near 0.3 m^{-1}) in the estuary, reflecting low concentrations of suspended sediment.

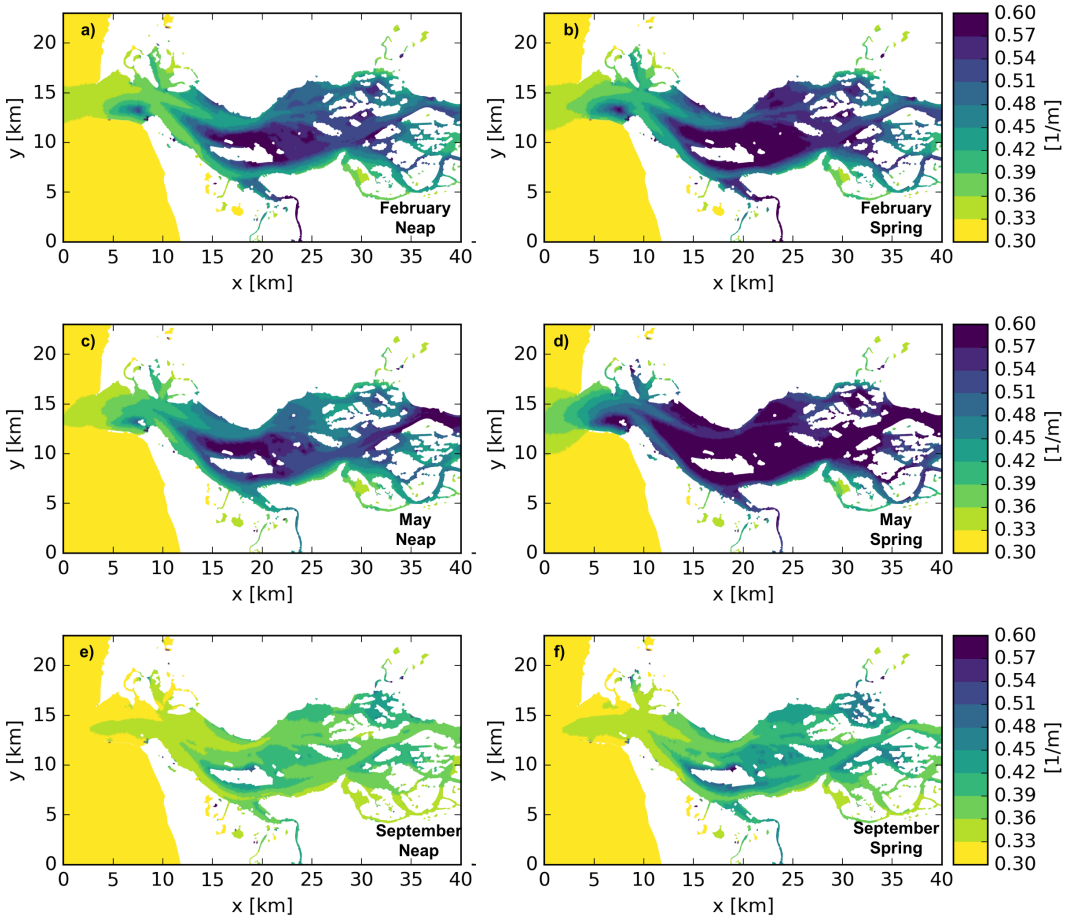

Figure 40. K_d averaged over the euphotic depth and a tidal cycle. (a) February (neap tide), (b) February (spring tide), (c) May (neap tide), (d) May (spring tide), (e) September (neap tide), and (f) September (spring tide).

For similar discharges, K_d is higher for spring than neap tides, as shown by comparing the right (springs) and left (neap) panels in Figure 40. The larger range of spring tides generates faster currents, increased bed stress, increased bed erosion, and thus higher concentration of suspended sediment (Lopez & Baptista, 2016a), leading to stronger light attenuation. Also, the salinity intrusion length tends to increase for neap tides, due to less vertical mixing, enabling deeper penetration into the estuary of ocean waters with characteristically low concentrations of suspended sediment (Kärnä, et al., 2015; Lopez & Baptista, 2016).

For the periods analyzed, the highest river discharges (above 10,000 $m^3\ s^{-1}$) and associated highest SSC concentrations at Beaver Army (~70 mg L^{-1}) occur in May, during the spring freshet; for these conditions, the vast majority of the estuary reaches values of K_d of at least 0.6 m^{-1} during spring tides, and ranging from 0.40 m^{-1} to 0.6 m^{-1} during neaps. By contrast, in September—with river discharges close to 3,500 $m^3\ s^{-1}$ and SST at Beaver Army in the 10-20 mg L^{-1} range—dominant values of K_d in the estuary are in the 0.35-0.45 $m^3 s^{-1}$ range. In February—with river discharges around 8,000 $m^3\ s^{-1}$ and SST at Beaver Army in the 20-30 mg L^{-1} range—values of K_d in the estuary are in the 0.40 m^{-1} to 0.6 m^{-1}, thus close the neap conditions in May. While neap-spring asymmetries of K_d are present in both February and September, they are much less pronounced than in May.

These results suggest that the seasonal variability of K_d in the estuary is primarily responsive to fluctuations in river discharge (which determine the extent of penetration in the estuary of low-sediment oceanic waters), and secondarily responsive to fluctuations of the fluvial source of sediment. This is consistent with the findings in Section 4.3.2, which suggest that concentration of suspended sediment in the estuary is typically greater than the fluvial concentrations due to tidally driven erosion, transport, and deposition cycles.

4.3.3 Estimates of euphotic depth

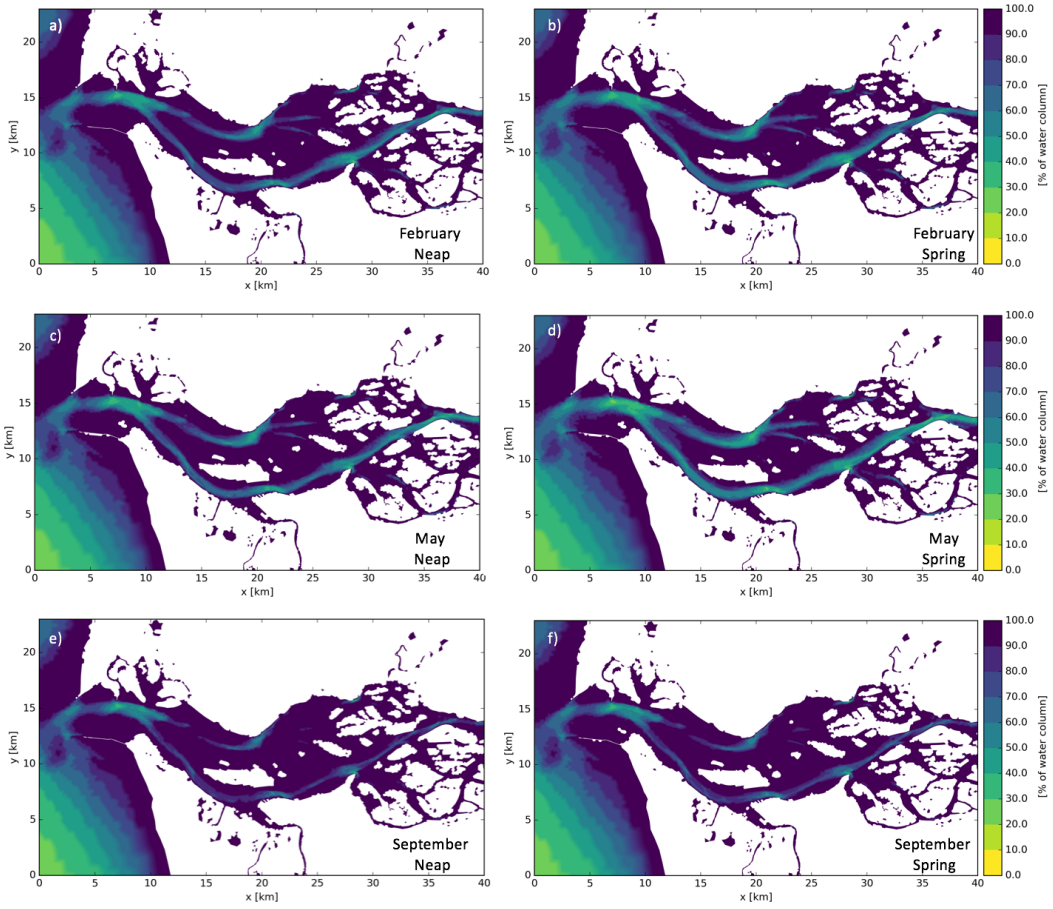

Figure 41 Estimates of the photic depth as a percentage of the water column for 2012. The time and tidal conditions are the same as those in Figure 40.

Tidally-averaged estimates of euphotic depth, described as a percentage of the water column, are shown in for the same select neap and spring tides in February, May and September discussed in Section 4.3.2. Except for the channels, the vast majority of the estuary remains entirely within the euphotic zone throughout the entire year. In the channels, seasonal variations of euphotic depth are modest; however, a larger percentage of the channels area is fully in the euphotic zone in September than in February and especially in May. Differences between spring and neap conditions are often negligible, but in May more of the channels are fully in the euphotic zone for neap than for spring tides.

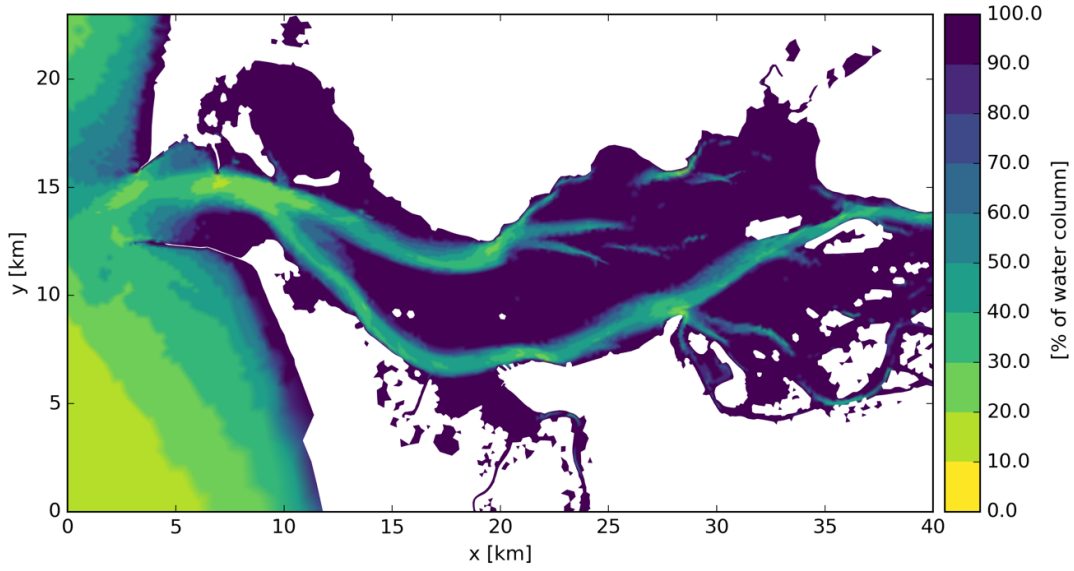

Figure 42 Euphotic depth as percent of the water column. Euphotic depth calculated using the static *Zulauf 7* parameterization of the Paulson & Simpson (1977) algorithms developed for the Columbia River estuary.

4.3.4 Comparison against Jerlov parameterizations

To assess the impact of the temporally- and spatially-varying K_d on circulation modeling, we compare SELFE results using the standard Jerlov static parameterization and the new parameterization dependent on K_d (model H, Equation 8). To incorporate model H, the second term in the Paulson & Simpson (1977) ((26) is replaced with $(1 - R)(e^{-zk_d})$ as was similarly done in *Wu et al.* (2007). That is, the blue-green extinction factor term is replaced with the temporally and spatially varying light extinction coefficient K_d calculated using Equation 7 and with K_d calculated within the sediment module of SELFE.

The euphotic depth for the system derived from the static Jerlov parameterization referred earlier as Zulauf 7 is shown in Figure 42. This parameterization broadly estimates of the euphotic depth similarly to the calculation derived from the modeled K_d ((24) resulting in the same light regions described in Section 4.3.3. The static Jerlov parameterization generally predicts less light penetration, particularly in the near shore region outside of the estuary and along the main

channels of the estuary. This suggests that the static Jerlov method is over-estimating attenuation of downward irradiance, which would lead to a low bias in temperature, however no such effect has been found (Kärnä et al., 2015).

We then compare circulation simulations for 2012 using both approaches for downward irradiation attenuation. The reference simulations, the result of an extensive calibration using the Jerlov parameterization, tend to over-predict temperatures in the estuary as described in (Kärnä et al., 2015). Elevation, salinity, and velocity results are indistinguishable between the two simulations. However, temperatures are generally higher than the reference model when variable K_d fields are used. These results suggest that simulations calibrated with a Jerlov parameterization do not benefit from the introduction of variable K_d, losing skill in temperature representation while making no difference in the representation of density stratification (which is mostly controlled by salinity fields). However, the results also suggest that the temperature fields are sensitive enough to the use of variable K_d to calculate light attenuation that a recalibration of the heat balance component of the circulation model might be worth considering.

4.4 Synthesis and Conclusions

Using observations of PAR and of water quality variables, we developed for the Columbia River estuary a correlation equation expressing the diffusive light attenuation coefficient, K_d as a function of turbidity and (as a surrogate for CDOM) salinity. The correlation has high skill ($R^2 = 0.86$), in the same form and with similar skill to the expression described by Xu et al. (2005) for the Chesapeake Bay. The coefficients and significant terms in the model suggest that light limitation is almost entirely caused by sediment-caused turbidity in the Columbia

River estuary.

Coupling this correlation with a circulation and sediment transport model, we estimated system-wide three-dimensional distributions of K_d for the full year of 2012. Analysis of these distributions shows that various regions of different light attenuation characteristics exist in the estuary and nearby ocean. Temporal variations of K_d are observed in the estuary, with light attenuation increasing with river discharge and with tidal range (both factors that contribute to a more turbid estuary). All these results are consistent with the system-wide distribution of salinity and suspended sediment concentrations.

Most of the estuary remains in the euphotic zone for the entire year except for the deepest parts of the main channels. These results, while not immediately obvious in an estuary known for its high turbidity, are consistent with historical findings based on observations (Lara-Lara et al., 1990) and are a consequence of the shallow depths that prevail throughout most of the estuary. In annual average, the euphotic depth calculated with our approach is not drastically different from what can be obtaining with an appropriate Jerlov parameterization of water types. However, the temporal variability unveiled by our approach might be useful for biogeochemical studies and modeling. Implications of spatially and temporally variable light attenuation (relative to the static Jerlov formulation) for circulation modeling are negligible for all variables but temperature. While outside the scope of this study, a re-calibration of the heat balance part of existing circulation models might be a useful future exercise.

The system-wide characterizations of K_d and euphotic depth presented here are affected by errors inherent to our circulation models, which affect the skill of salinity and sediment fields and have been discussed in (Kärnä et al., 2015; Kärnä

& Baptista, 2016; Lopez & Baptista, 2016a). More fundamentally, though, the skill of (and confidence in) our approach would be improved by (primarily) a more extensive observational set for PAR and (secondarily) by refining the vertical integration strategies for all variables used in deriving the correlation between K_d and salinity and turbidity. The emergence of biogeochemical models for the Columbia River estuary might also allow the use of a more skilled correlation where K_d is explained through CDOM and chlorophyll *a*, in addition to turbidity and instead of salinity; however, we did not find Chlorophyll *a* to substantially improve the predictive skill of the correlation, and salinity appears to be a very good surrogate for CDOM.

5 SUMMARY AND CONCLUSIONS

The purpose of this research was to advance the characterization of suspended sediment dynamics and of the aquatic light field in the Columbia River estuary using a realistic, three-dimensional numerical model informed and skill assessed against observations from fixed stations and research cruises.

This work included improvements in the computational efficiency and strong-scaling of the hydrodynamic model SELFE and enhancements to the numerical stability of the sediment model. The work demonstrated that scalable preconditioners and algorithms for the linear solve of the coupled continuity-momentum equations are essential for scalability in coastal ocean models. The work also showed that careful treatment of I/O is critical for efficient run-time and scaling even when using massive parallel file systems.

A set of idealized standard test cases and a realistic application to the Columbia River estuary were used to validate and skill assess the sediment model and were made publically available as a benchmark. Sediment model results in all test cases are extremely sensitive to the implementation of the bottom boundary layer and

parameterizations for critical stress and erosion rate. Extensive sensitivity studies were required to reproduce expected results in even highly constrained idealized test cases. Realistic applications to the Columbia River estuary required a considerable number of sensitivity studies for bed properties and settling speed to optimize model skill of suspended sediment. Despite the extensive sensitivity tests, sediment model skill lagged that of prognostic variables, frequently underestimating suspended sediment concentrations. Uncertainty in the sediment model implementation and sub-optimal model parameterization limited model skill which was exacerbated by defects in hydrodynamics, most prominently, the underprediction of salinity. These results indicate that highly skilled estuarine sediment models require accurate representations of density, and currents *and* optimal sediment model parameterization beyond what is capable with the current model.

Yearlong simulations of the Columbia River estuary provided an unprecedented synoptic view of suspended sediment dynamics through the entire system over sub-tidal to seasonal time scales. Model results show that the vast majority of suspended sediment is transported in the main channels with secondary pathways through Cathlamet Bay and the channels in the upstream shoals. Mean advection is the primary suspended sediment transport process through the estuary. When the estuary is in a partially mixed regime, tidal pumping is sufficient to generate residual upstream transport at mid-estuary stations including SATURN-01 and SATURN-03, but not at downstream locations that remain stratified through the tidal cycle. Lateral transport of suspended sediment is minor compared to the along-channel component, but periodic pulses of lateral transport are observed in field observations and model results particularly in the North Channel near

SATURN-01 where multiple upstream channels converge. Model results and observations indicate that the Columbia River ETM exist as part of a larger system of sedimentary processes in a broad region roughly collocated with the extent of the salt wedge – the ETM zone. In this region, the erosion, deposition, settling, and transport of suspended sediments is modulated by stratification and driven by the tidal dynamics. Specifically, the tides induce a four-stage cycle where sediment is eroded and transported during ebbs and floods and deposited during the low energy slack tides. Within this cycle, sediment circulates through three regions: the stratified section of the salt wedge, the toe of the salt wedge, and the vertically mixed region upstream of the salt wedge. The classical ETM exists near the toe of the salt wedge throughout the tidal cycle, but is influenced by the dynamics in the other sections.

A predictive light attenuation model derived from the commonly measured water quality variables salinity and turbidity was developed to describe the diffusive light attenuation coefficient of PAR. Observations and the empirical light model indicate that suspended sediment is the largest contributing factor to light attenuation in the Columbia apart from water itself. Application of suspended sediment and salinity from the three-dimensional numerical sediment model to the light attenuation model show that the majority of the Columbia River Estuary remains in the photic zone, defined as the depth at which one percent of surface PAR penetrates, except for the turbid, deep main channels. Implementation of the empirical light attenuation model in SELFE to calculate the attenuation factor for blue-green spectral component in *Paulson & Simpson* (1977) model of downward irradiance did not produce hydrodynamic results that differed significantly from the standard, static Jerlov based scheme. The lack effect on hydrodynamics and

temperature is likely due to the short residence time of the system.

This work produced a computationally efficient and scalable hydrodynamic and sediment model calibrated for the Columbia River estuary with practical model skill for suspended sediment equal to, or better, than similar models in other systems. The validation of the model provided the community with an open benchmark in an effort to push open standards and the general improvement in sediment model predictive ability and utility. Processes studies of sediment dynamics using this model in the Columbia have advanced the characterization of sedimentary processes and the variability of suspended sediment in the system over time scales and in detail that were not previously possible due to computational limitations and lack of data. The application of the system-specific description of the diffusive light attenuation coefficient is new for the Columbia, providing unprecedented detail of light availability and describing the variability over forcing conditions. As such, this work has produced both efficient, ready to use tools for this system in addition to advancing fundamental descriptions and analysis of sediment dynamics, suspended sediment variability, and the impacts of sediment on the aquatic light environment.

Despite the advances in the characterization of suspended sediment dynamics and their influence on the light environment in the Columbia River estuary, the approach taken here has a number of limitations. Fundamental problems in the underlying hydrodynamics results in under-predicted salinity intrusion and retention in the estuary inducing bias in the sediment model, particularly with respect to location of the ETM. A less diffusive hydrodynamic model is likely to be required to address this issue.

The approach to sediment modeling is limited by missing physical processes and

reliance on best-available, but coarsely defined parameterizations. First among these is the uncertainty associated with bed dynamics in the system. Although the bed composition in this study was derived from published observations of the system, the lack of recent detailed data of bed layers prevented use of more than a single layer. Also, the model did not include flocculation, which is known to affect suspended particulate matter composition and settling velocity on tidal time scales. Flocculation mechanisms were surveyed and implemented in the numerical model, but were not used in these studies due to a lack of validation data. The Columbia River estuary is subject to substantial shortwave activity near the mouth which may lead to periodic pulses in sediment erosion. We did not include a wave model with the justification that circulation in the Columbia River estuary is dominated by mean advection. However, waves may play a larger role in localized regions in the lateral bays and intertidal shoals between the main channels. Finally, with respect to sediment modeling, the skill metrics used here are standard, but simplistic, and do not account for or propagate uncertainty.

The light attenuation model was derived from observations of single research cruise along the main channels and therefore does not reflect potential seasonal fluctuations in the collected djatasets. A more robust model would include observations across longer time scales and would include more regions of the estuary including lateral bays and the extensive intertidal sand bars.

We recognize these as research limitations and hope that future work will resolve these issues.

6 BIBLIOGRAPHY

Allen, G. P., Salomon, J. C., Bassoullet, P., Du Penhoat, Y., & de Grandpré, C. (1980). Effects of tides on mixing and suspended sediment transport in macrotidal estuaries. *Sedimentary Geology*, *26*(1–3), 69–90. http://doi.org/http://dx.doi.org/10.1016/0037-0738(80)90006-8

Baker, K. S., & Smith, R. C. (1982). Bio-optical classification and model of natural waters. *Limnology and Oceanography*, *27*(3), 500–509. http://doi.org/10.4319/lo.1982.27.3.0500

Banas, N., Maccready, P., & Hickey, B. (2009). The Columbia River plume as cross-shelf exporter and along-coast barrier. *Continental Shelf Research*, *29*(1), 292–301. http://doi.org/10.1016/j.csr.2008.03.011

Banas, N. S., Lessard, E. J., Kudela, R. M., MacCready, P., Peterson, T. D., Hickey, B. M., & Frame, E. (2009). Planktonic growth and grazing in the Columbia River plume region: A biophysical model study. *Journal of Geophysical Research*, *114*, 1–21. http://doi.org/10.1029/2008JC004993

Baptista, A., Howe, B., Freire, J., Maier, D., & Silva, C. (2008). Scientific exploration in the era of ocean observatories. *Computing in Science and Engineering*, *10*(3), 53–58.

Baptista, A., Seaton, C., Wilkin, M., Riseman, S., Turner, P., Karna, T., … Megler, V. (2015). Infrastructure for collaborative estuarine science and societal applications in the Columbia River, United States. *Frontiers of Earth Science*, *9*(4), 659–682. http://doi.org/10.1007/s11707-015-0540-5

Barnes, C., Duxbury, A., & Morse, B. (1972). Circulation and selected properties of the Columbia River effluent at sea. In D. L. Alverson & A. T. Pruter (Eds.), *The Columbia River Estuary and adjacent waters. Bioenvironmental studies* (pp. 41–80). University of Washington Press.

Baross, J. A., Crump, B. C., & Simenstad, C. (1994). Elevated microbial loop activities in the Columbia River estuarine turbidity maximum. In *Changes in fluxes in estuaries; implications from science to management* (p. 459).

Barron, C. N., Kara, A. B., Martin, P. J., Rhodes, R. C., & Smedstad, L. F. (2006). Formulation, implementation and examination of vertical coordinate choices in the Global Navy Coastal Ocean Model (NCOM). *Ocean Modelling*, *11*(3–4), 347–375. http://doi.org/10.1016/j.ocemod.2005.01.004

Baugh, J. V, & Manning, A. J. (2007). An assessment of a new settling velocity parameterisation for cohesive sediment transport modeling. *Continental Shelf Research*, *27*(13), 1835–1855. http://doi.org/10.1016/j.csr.2007.03.003

Becherer, J., Floser, G., Umlauf, L., & Burchard, H. (2016). Estuarine circulation versus tidal pumping: Sediment transport in a well-mixed tidal inlet. *Journal of Geophysical Research: Oceans*, *121*(8), 6251–6270. http://doi.org/10.1002/2016JC011640

Bottom, D. L., Simenstad, C. A., Burke, J., Baptista, A. M., Jay, D. A., Jones, K. K., … Schiewe, M. H. (2005). *Salmon at River's End: The Role of the Estuary in the Decline and Recovery of Columbia River Salmon*. U.S. Department of Commerce.

Brenon, I., & Le Hir, P. (1999). Modelling the Turbidity Maximum in the Seine Estuary (France): Identification of Formation. *Estuarine, Coastal and Shelf Science*, *49*(4), 525–544. http://doi.org/10.1006/ecss.1999.0514

Burchard, H., & Baumert, H. (1998). The formation of estuarine turbidity maxima due to density effects in the salt wedge. A hydrodynamic process study. *Journal of Physical Oceanography*, *28*(2), 309–321. http://doi.org/10.1175/1520-0485(1998)028<0309:TFOETM>2.0.CO;2

Burchard, H., Bolding, K., & Villarreal, M. R. (2004). Three-dimensional modelling of estuarine turbidity maxima in a tidal estuary. *Ocean Dynamics*, *54*(2), 250–265. http://doi.org/10.1007/s10236-003-0073-4

Burchard, H., Floser, G., Staneva, J. V, Badewien, T. H., & Riethmuller, R. (2008). Impact of density gradients on net sediment transport into the Wadden Sea. *Journal of Physical Oceanography*, *38*(3), 566–587. http://doi.org/10.1175/2007jpo3796.1

Casulli, V., & Cheng, R. T. (1992). Semi-implicit finite difference methods for three-dimensional shallow water flow. *International Journal for Numerical Methods in Fluids*, *15*(6), 629–648. http://doi.org/10.1002/fld.1650150602

Chawla, A., Jay, D. A., Baptista, A. M., Wilkin, M., & Seaton, C. (2008). Seasonal Variability and Estuary–Shelf Interactions in Circulation Dynamics of a River-dominated Estuary. *Estuaries and Coasts*, *31*(2), 269–288. http://doi.org/10.1007/s12237-007-9022-7

Chen, C., Liu, H., & Beardsley, R. C. (2003). An unstructured grid, finite-volume, three-dimensional, primitive equations ocean model: Application to coastal ocean and estuaries. *Journal of Atmospheric and Oceanic Technology*, *20*(1), 159–186. http://doi.org/10.1175/1520-0426(2003)020<0159:AUGFVT>2.0.CO;2

Conomos, T., Gross, M., A, B. C., & Richards, F. A. (1972). River-ocean nutrient relations in summer. In D. L. Alverson & A. T. Pruter (Eds.), *The Columbia*

River Estuary and adjacent waters. Bioenvironmental studies (pp. 151–175). University of Washington Press.

Conomos, T. J., & Gross, M. G. (1972). River-ocean suspended particulate matter relations in summer. In D. L. Alverson & A. T. Pruter (Eds.), *The Columbia River Estuary and adjacent waters. Bioenvironmental studies* (pp. 254–265). University of Washington Press.

Crump, B. C., Armbrust, E. V., & Baross, J. A. (1999). Phylogenetic Analysis of Particle-Attached and Free-Living Bacterial Communities in the Columbia River, Its Estuary, and the Adjacent Coastal Ocean. *Applied and Environmental Microbiology*, *65*(7), 3192–3204.

Davies-Colley, R. J., & Nagels, J. W. (2008). Predicting light penetration into river waters. *Journal of Geophysical Research: Biogeosciences*, *113*(3), 1–9. http://doi.org/10.1029/2008JG000722

de Nijs, M. J., & Pietrzak, J. D. (2012). Saltwater intrusion and ETM dynamics in a tidally-energetic stratified estuary. *Ocean Modelling*, *49*, 60–85. http://doi.org/10.1016/j.ocemod.2012.03.004

Dyer, K. R. (1973). *Estuaries: A physical introduction*. *Estuarine and Coastal Marine Science* (2nd ed., Vol. 1). John Wiley & Sons. http://doi.org/10.1016/0302-3524(73)90042-X

Dyer, K. R. (1995). Sediment transport processes in estuaries. *Geomorphology and Sedimentology of Estuaries*, *53*, 423–449.

Elias, E. P. L., Gelfenbaum, G., & Van der Westhuysen, A. J. (2012). Validation of a coupled wave-flow model in a high-energy setting: The mouth of the Columbia River. *Journal of Geophysical Research: Oceans*, *117*(9), 1–21. http://doi.org/10.1029/2012JC008105

Fain, A. M. V., Jay, D. A., Wilson, D. J., Orton, P. M., & Baptista, A. M. (2001). Seasonal and Tidal Monthly Patterns of Particulate Matter Dynamics in the Columbia River Estuary. *Estuaries*, *24*(5), 770. http://doi.org/10.2307/1352884

Ferguson, C. M., Coote, B. G., Ashbolt, N. J., & Stevenson, I. M. (1996). Relationships between indicators, pathogens and water quality in an estuarine system. *Water Research*, *30*(9), 2045–2054. http://doi.org/10.1016/0043-1354(96)00079-6

Festa, J. F., & Hansen, D. V. (1978). Turbidity maxima in partially mixed estuaries: A two-dimensional numerical model. *Estuarine and Coastal Marine Science*, *7*(4), 347–359. http://doi.org/10.1016/0302-3524(78)90087-7

Fortunato, A. B., & Oliveira, A. (2004). A modeling system for tidally driven long-term morphodynamics. *Journal of Hydraulic Research*, *42*(4), 426–434. http://doi.org/10.1080/00221686.2004.9641210

Fortunato, C. S., & Crump, B. C. (2011). Bacterioplankton Community Variation Across River to Ocean Environmental Gradients. *Microbial Ecology*, *62*(2), 374–382. http://doi.org/10.1007/s00248-011-9805-z

Fortunato, C. S., & Crump, B. C. (2015). Microbial gene abundance and expression patterns across a river to ocean salinity gradient. *PLoS ONE*, *10*(11), 1–22. http://doi.org/10.1371/journal.pone.0140578

Fortunato, C. S., Eiler, A., Herfort, L., Needoba, J. A., Peterson, T. D., Crump, B. C., … BC, C. (2013). Determining indicator taxa across spatial and seasonal gradients in the Columbia River coastal margin. *Isme J*, *7*(10), 1899–1911. http://doi.org/10.1038/ismej.2013.79

Fox, D., Bell, S., Nehlsen, W., & Damron, J. (1984). Atlas of Physical and Biological Characteristics of the Columbia River Estuary. *Columbia River Estuary Data Development Program*.

Frame, E. R., & Lessard, E. J. (2009). Does the Columbia River plume influence phytoplankton community structure along the Washington and Oregon coasts? *Journal of Geophysical Research: Oceans*, *114*(7), 1–13. http://doi.org/10.1029/2008JC004999

Fringer, O. B., Gerritsen, M., & Street, R. L. (2006). An unstructured-grid, finite-volume, nonhydrostatic, parallel coastal ocean simulator. *Ocean Modelling*, *14*(3–4), 139–173. http://doi.org/10.1016/j.ocemod.2006.03.006

Gallegos, C. L., Correll, D. L., & Pierce, J. W. (1990). Modeling spectral diffuse attenuation, absorption, and scattering coefficients in a turbid estuary. *Limnology and Oceanography*. http://doi.org/10.4319/lo.1990.35.7.1486

Gelfenbaum, G. (1983). Suspended-sediment response to semidiurnal and fortnightly tidal variations in a mesotidal estuary: Columbia River, U.S.A. *Marine Geology*, *52*(1), 39–57. http://doi.org/10.1016/0025-3227(83)90020-8

Gelfenbaum, G., & Kaminsky, G. M. (2010). Large-scale coastal change in the Columbia River littoral cell: An overview. *Marine Geology*, *273*(1–4), 1–10. http://doi.org/10.1016/j.margeo.2010.02.007

Gelfenbaum, G., Sherwood, C. R., Peterson, C. D., Kaminsky, G. M., Buijsman, M., Twichell, D. C., … Reed, C. (1999). The Columbia River Littoral Cell: A sediment budget overview. *Coastal Sediments '99 Proceedings of the 4th International Conference on Coastal Engineering and Coastal Sediment Processes*, 1–19.

Geyer, W. R. (1993). The Importance of Suppression of Turbulence by Stratification on the Estuarine Turbidity Maximum. *Estuaries*, *16*(1), 113. http://doi.org/10.2307/1352769

Geyer, W. R., & MacCready, P. (2014). The Estuarine Circulation. *Annual Review of Fluid Mechanics*, *46*(1), 175–197. http://doi.org/10.1146/annurev-fluid-010313-141302

Gordon, H. R. (1989). Can the Lambert-Beer law be applied to the diffuse attenuation coefficient of ocean water? *Limnology and Oceanography*, *34*(8), 1389–1409.

Häder, D., Kumar, H. D., Smith, R. C., & Worrest, R. C. (2006). Effects of solar UV radiation on aquatic ecosystems and interactions with climate change. *Photochemical & Photobiological Sciences*, *6*(3), 95–134. http://doi.org/10.1039/b700020k

Hamilton, P. (1990). Modeling salinity and circulation for the Columbia River estuary. *Progress in Oceanography*, *25*(1–4), 113–156. http://doi.org/dx.doi.org/10.1016/0079-6611(90)90005-M

Hansen, D. V, & Rattray, J. M. (1966). New dimensions in estuary clasification. *Limnology and Oceanography*, *11*(3), 319–326.

Harris, C. K., & Wiberg, P. L. (2001). A two-dimensional, time-dependent model of suspended sediment transport and bed reworking for continental shelves. *Computers and Geosciences*, *27*(6), 675–690. http://doi.org/10.1016/S0098-3004(00)00122-9

Herfort, L., Peterson, T. D., Campbell, V., Futrell, S., & Zuber, P. (2011). Myrionecta rubra (Mesodinium rubrum) bloom initiation in the Columbia River estuary. *Estuarine, Coastal and Shelf Science*, *95*(4), 440–446. http://doi.org/10.1016/j.ecss.2011.10.015

Herfort, L., Peterson, T. D., McCue, L. A., Crump, B. C., Prahl, F. G., Baptista, A. M., … Zuber, P. (2011). Myrionecta rubra population genetic diversity and its cryptophyte chloroplast specificity in recurrent red tides in the Columbia River estuary. *Aquatic Microbial Ecology*, *62*(1), 85–97. http://doi.org/10.3354/ame01460

Herfort, L., Peterson, T. D., McCue, L. A., & Zuber, P. (2011). Protist 18S rRNA gene sequence analysis reveals multiple sources of organic matter contributing to turbidity maxima of the Columbia River estuary. *Marine Ecology-Progress Series*, *438*, 19–31. http://doi.org/10.3354/meps09303

Hickey, B. M., Kudela, R. M., Nash, J. D., Bruland, K. W., Peterson, W. T., MacCready, P., … Lohan, M. C. (2010). River Influences on Shelf Ecosystems: Introduction and synthesis. *Journal of Geophysical Research: Oceans*, *115*(2), 1–26. http://doi.org/10.1029/2009JC005452

Horner-Devine, A. R. (2009). The bulge circulation in the Columbia River plume. *Continental Shelf Research*, *29*(1), 234–251. http://doi.org/10.1016/j.csr.2007.12.012

Hubbell, D. W., & Glenn, J. L. (1973). Distribution of Radionuclides in Bottom Sediments of the Columbia River Estuary Distribution of Radionuclides in Bottom Sediments of the Columbia River Estuary. Washington, D.C.

Hughes, F. W., & Rattray, M. (1980). Salt flux and mixing in the Columbia River Estuary. *Estuarine and Coastal Marine Science*, *10*(5), 479–493. http://doi.org/10.1016/S0302-3524(80)80070-3

Jay, D. A. (1984). Circulatory processes in the Columbia River estuary. *Astoria, OR: Columbia River Estuary Data Development Program*.

Jay, D. A., Dungan Smith, J., & Smith, J. D. (1990). Circulation, density distribution and neap-spring transitions in the Columbia River Estuary. *Progress in Oceanography*, *25*(1–4), 81–112. http://doi.org/10.1016/0079-6611(90)90004-L

Jay, D. A., & Musiak, J. D. (1994). Particle trapping in estuarine tidal flows. *Journal of Geophysical Research*, *99*(C10), 20445. http://doi.org/10.1029/94JC00971

Jay, D. A., & Musiak, J. D. (1995). Internal Tidal Asymmetry in Channel Flows: Origins and Consequences. *Mixing in Estuaries and Coastal Seas*, *50*, 211–249. http://doi.org/10.1029/CE050p0211

Jay, D. A., Orton, P. M., Chisholm, T., & Wilson, D. J. (2007). Particle Trapping in Stratified Estuaries : Consequences of Mass Conservation. *Estuaries and Coasts*, *30*(6), 1095–1105.

Jay, D. A., Orton, P. M., Chisholm, T., Wilson, D. J., Annika, M., Fain, V., … Wilson, J. (2007). Particle Trapping in Stratified Estuaries : Application to Observations Particle Trapping in Stratified Estuaries : Application to Observations. *Estuaries and Coasts*, *30*(6), 1106–1125.

Kärnä, T., & Baptista, A. M. (2016). Evaluation of a long-term hindcast simulation for the Columbia River estuary. *Ocean Modelling*, *99*, 1–14. http://doi.org/10.1016/j.ocemod.2015.12.007

Kärnä, T., Baptista, A. M., Lopez, J. E., Turner, P. J., Mcneil, C., & Sanford, T. B. (2015). Numerical modeling of circulation in high-energy estuaries: A Columbia River estuary benchmark. *Ocean Modelling*, *88*, 54–71. http://doi.org/10.1016/j.ocemod.2015.01.001

Kerr, P. C., Donahue, A. S., Westerink, J. J., Luettich, R. A., Zheng, L. Y., Weisberg, R. H., … Cox, A. T. (2013). U.S. IOOS coastal and ocean modeling testbed: Inter-model evaluation of tides, waves, and hurricane surge in the Gulf of Mexico. *Journal of Geophysical Research: Oceans*, *118*(10), 5129–5172. http://doi.org/10.1002/jgrc.20376

Kilcher, L. F., & Nash, J. D. (2010). Structure and dynamics of the Columbia River tidal plume front. *Journal of Geophysical Research: Oceans*, *115*(5), 1–20. http://doi.org/10.1029/2009JC006066

Kirk, J. T. O. (1994). *Light and photosynthesis in aquatic ecosystems*. Cambridge University Press.

Kudela, R. M., & Peterson, T. D. (2009). Influence of a buoyant river plume on phytoplankton nutrient dynamics: What controls standing stocks and productivity? *Journal of Geophysical Research*, *114*(7), 1–15. http://doi.org/10.1029/2008JC004913

Kularatne, S., & Pattiaratchi, C. (2008). Turbulent kinetic energy and sediment resuspension due to wave groups. *Continental Shelf Research*, *28*(6), 726–736. http://doi.org/10.1016/j.csr.2007.12.007

Lara-Lara, J. R., Frey, B. E., & Small, L. F. (1990). Primary Production in the Columbia River Estuary:Spatial and Temporal Variability of Properties. *Pacific Science*, *44*(1), 17–37.

Lara-Lara, J. R., Frey, B. E., & Small, L. F. (1990). Primary production in the Columbia River estuary. II. Grazing losses transport and phytoplankton carbon budget. *Pacific Science*, *44*(1), 38–50.

Le Hir, P., Roberts, W., Cazaillet, O., Christie, M., Bassoullet, P., & Bacher, C. (2000). Characterization of intertidal flat hydrodynamics. *Continental Shelf Research*, *20*(12–13), 1433–1459. http://doi.org/10.1016/S0278-4343(00)00031-5

Lesser, G. R., Roelvink, J. A., Kester, J. A. T. M. Van, & Stelling, G. S. (2004). Development and validation of a three-dimensional morphological model, *51*, 883–915. http://doi.org/10.1016/j.coastaleng.2004.07.014

Lin, J., & Kuo, A. Y. (2003). A model study of turbidity maxima in the York River estuary, Virginia. *Estuaries*, *26*(5), 1269–1280. http://doi.org/10.1007/BF02803629

Lopez, J. E., & Baptista, A. M. (2016a). Benchmarking an unstructured grid sediment model. *Ocean Modelling*, *110*, 32–48. http://doi.org/10.1016/j.ocemod.2016.12.006

Lopez, J. E., & Baptista, A. M. (2016b). SELFE sediment model benchmark in the Columbia River estuary. http://doi.org/10.5281/zenodo.60071

Lutz, G. A., Hubbell, D. W., & Stevens, H. . (1971). Discharge and flow distribution, Columbia River estuary. USGS Numbered Series (Vol. 433).

Maa, J. P.-Y., & Mehta, A. J. (1990). Soft Mud Response to Water Waves. *Journal of Waterway, Port, Coastal, and Ocean Engineering*, *116*(5), 634–650. http://doi.org/10.1061/(ASCE)0733-950X(1990)116:5(634)

MacCready, P., Banas, N., Hickey, B., Dever, E., & Liu, Y. (2009). A model study of tide- and wind-induced mixing in the Columbia River Estuary and plume. *Continental Shelf Research*, *29*(1), 278–291. http://doi.org/10.1016/j.csr.2008.03.015

McSweeney, J. M., Chant, R. J., & Sommerfield, C. K. (2016). Lateral variability of sediment transport in the Delaware Estuary. *Journal of Geophysical Research: Oceans*, *121*(1), 725–744. http://doi.org/10.1002/2015JC010974

Meade, R. H. (1972). Transport and Deposition of Sediments in Estuaries. *Geological Society of America Memoirs*, *133*, 91–120. http://doi.org/10.1130/MEM133-p91

Mesinger, F., DiMego, G., Kalnay, E., Mitchell, K., Shafran, P. C., Ebisuzaki, W., … Shi, W. (2006). North American regional reanalysis. *Bulletin of the American Meteorological Society*, *87*(3), 343–360. http://doi.org/10.1175/BAMS-87-3-343

Meyer-Peter, E., & Müller, R. (1948). Formulas for Bed-Load Transport. *Proceedings of the 2nd Meeting of the International Association of Hydraulic Research*, 39–64. http://doi.org/1948-06-07

Morgan, C. A., Cordell, J. R., & Simenstad, C. A. (1997). Sink or swim? Copepod population maintenance in the Columbia River estuarine turbidity-maxima region. *Marine Biology*, *129*(2), 309–317. http://doi.org/10.1007/s002270050171

Myers, E. P., & Baptista, A. M. (2001). Inversion for tides in the Eastern North Pacific Ocean. *Advances in Water Resources*, *24*(5), 505–519. http://doi.org/10.1016/S0309-1708(00)00041-5

Nash, J. D., Kilcher, L. F., & Moum, J. N. (2009). Structure and composition of a strongly stratified, tidally pulsed river plume. *Journal of Geophysical Research: Oceans*, *114*(8), 1–16. http://doi.org/10.1029/2008JC005036

Neal, V. . (1965). A Calculation of Flushing Times and Pollution Contribution for the Columbia River Estuary. Oregon State.

O'Brien, M. P. (1972). Field and Laboratory Studies; Navigation Channels of the Columbia River Estuary. *International Conference on Coastal Engineering Proceedings*, *1*(13).

Pan, J., & Jay, D. A. (2009). Effects of ambient velocity shear on nonlinear internal wave associated mixing at the Columbia River plume front. *Journal of Geophysical Research*, *114*(June), 1–13. http://doi.org/10.1029/2008JC004988

Paulson, C. A., & Simpson, J. J. (1977). Irradiance measurements in the upper ocean. *Journal of Physical Oceanography*, *7*, 952–956. http://doi.org/10.1175/1520-0485(1977)007<0952:IMITUO>2.0.CO;2

Perkins, R. W., Nelson, J. L., & Haushild, W. L. (1966). Behavior and transport of radionuclides in the Columbia River between Hanford and Vancouver, Washington. *Limnology and Oceanography*, *11*(2), 235–248. http://doi.org/10.4319/lo.1966.11.2.0235

Peterson, J. O., & Peterson, W. T. (2009). Influence of the Columbia River plume on cross-shelf transport of zooplankton. *Journal of Geophysical Research: Oceans*, *114*(7), 1–11. http://doi.org/10.1029/2008JC004965

Pfeiffer-Herbert, A. S., Prahl, F. G., Hales, B., Lerczak, J. A., Pierce, S. D., & Levine, M. D. (2016). High resolution sampling of methane transport in the Columbia River near-field plume: Implications for sources and sinks in a river-dominated estuary. *Limnology and Oceanography*, *61*, S204–S220. http://doi.org/10.1002/lno.10221

Pinto, L., Fortunato, A. B., Zhang, Y., Oliveira, A., & Sancho, F. E. P. (2012). Development and validation of a three-dimensional morphodynamic modelling system for non-cohesive sediments. *Ocean Modelling*. http://doi.org/10.1016/j.ocemod.2012.08.005

Prahl, F., Small, L., & Eversmeyer, B. (1997). Biogeochemical characterization of suspended particulate matter in the Columbia River estuary. *Marine Ecology Progress Series*, *160*, 173–184. http://doi.org/10.3354/meps160173

Ralston, D. K., Geyer, W. R., Lerczak, J. A., & Scully, M. (2010). Turbulent mixing in a strongly forced salt wedge estuary. *Journal of Geophysical Research: Oceans*, *115*(12), 1–21. http://doi.org/10.1029/2009JC006061

Ralston, D. K., Geyer, W. R., Traykovski, P. A., & Nidzieko, N. J. (2013). Effects of estuarine and fluvial processes on sediment transport over deltaic tidal flats. *Continental Shelf Research*, *60*, S40–S57. http://doi.org/10.1016/j.csr.2012.02.004

Ralston, D. K., Geyer, W. R., & Warner, J. C. (2012). Bathymetric controls on sediment transport in the Hudson River estuary: Lateral asymmetry and frontal trapping. *Journal of Geophysical Research*, *117*(C10), C10013. http://doi.org/10.1029/2012JC008124

Reed, D. J., & Donovan, J. (1994). The character and composition of the Columbia River estuarine turbidity maximum. *Changes in Fluxes in Estuaries; Implications from Science to Management*, 445–450. http://doi.org/10.1161/01.HYP.7.3_Pt_2.I49

Rogers, E., DiMego, G., Black, T., Ek, M., Ferrier, B., Gayno, G., … Wu, W. (2009). The NCEP North American Mesoscale Modeling System: Recent Changes and Future Plans. In *23rd Conference on Weather Analysis and Forecasting/19th Conference on Numerical Weather Prediction*. Omaha, Nebraska.

Ruggiero, P., Kaminsky, G. M., Gelfenbaum, G., & Voigt, B. (2005). Seasonal to Interannual Morphodynamics along a High-Energy Dissipative Littoral Cell. *Journal of Coastal Research*, *21*(3), 553–578. http://doi.org/10.2112/03-0029.1

Sanford, T. B., McNeil, C., Shcherbina, A. Y., Litchendorf, T. M., Karna, T., Lopez, J. E., & Baptista, A. M. (2015, February). CMOP 2012 AUV-WP Columbia River estuary benchmark data set. http://doi.org/10.5281/zenodo.13782

Saux Picart, S., Butenschén, M., & Shutler, J. D. (2012). Wavelet-based spatial comparison technique for analysing and evaluating two-dimensional geophysical model fields. *Geoscientific Model Development*, *5*(1), 223–230. http://doi.org/10.5194/gmd-5-223-2012

Scully, M. E., & Friedrichs, C. T. (2007). Sediment pumping by tidal asymmetry in a partially mixed estuary. *Journal of Geophysical Research*, *112*(C7), C07028. http://doi.org/10.1029/2006JC003784

Sherwood, C. R., & Creager, J. S. (1990). Sedimentary geology of the Columbia River Estuary. *Progress in Oceanography*. http://doi.org/10.1016/0079-6611(90)90003-K

Sherwood, C. R., Jay, D. A., Bradford Harvey, R., Hamilton, P., & Simenstad, C. A. (1990, January). Historical changes in the Columbia River Estuary. *Progress in Oceanography*. http://doi.org/10.1016/0079-6611(90)90011-P

Simenstad, C. A., Reed, D., Jay, D. A., Baross, J. A., Prahl, F. G., & Small, L. F. (1994). Land-margin ecosystem research in the Columbia River estuary: an interdisciplinary approach to investigating couplings between hydrological, geochemical and ecological processes within estuarine turbidity maxima. *Changes in Fluxes in Estuaries: Implications from Science to Management. Olsen & Olsen: Fredensborg*, 437–444.

Simenstad, C. A., Small, L. F., David McIntire, C., Jay, D. A., & Sherwood, C. (1990). Columbia river estuary studies: An introduction to the estuary, a brief history, and prior studies. *Progress in Oceanography*, *25*(1–4), 1–13. http://doi.org/10.1016/0079-6611(90)90002-J

Small, L. L. F., & Prahl, F. G. (2004). A Particle Conveyor Belt Process in the Columbia River Estuary : Evidence from Chlorophyll a and Particulate Organic Carbon. *Estuaries*, *27*(6), 2004.

Smith, E. M., & Benner, R. (2005). Photochemical transformations of riverine dissolved organic matter: Effects on estuarine bacterial metabolism and nutrient demand. *Aquatic Microbial Ecology*, *40*(1), 37–50. http://doi.org/10.3354/ame040037

Smith, M. W., Davis, R. E., Youngblut, N. D., Kärnä, T., Herfort, L., Whitaker, R. J., … Simon, H. M. (2015). Metagenomic evidence for reciprocal particle exchange between the mainstem estuary and lateral bay sediments of the

lower Columbia River. *Frontiers in Microbiology*, *6*(OCT), 1–20. http://doi.org/10.3389/fmicb.2015.01074

Smith, M. W., Herfort, L., Tyrol, K., Suciu, D., Campbell, V., Crump, B. C., … Simon, H. M. (2010). Seasonal changes in bacterial and archaeal gene expression patterns across salinity gradients in the Columbia River coastal margin. *PLoS ONE*, *5*(10). http://doi.org/10.1371/journal.pone.0013312

Smith, M. W., Zeigler Allen, L., Allen, A. E., Herfort, L., & Simon, H. M. (2013). Contrasting genomic properties of free-living and particle-attached microbial assemblages within a coastal ecosystem. *Frontiers in Microbiology*, *4*(May), 120. http://doi.org/10.3389/fmicb.2013.00120

Soulsby, R. L., Manning, A. J., Spearman, J., & Whitehouse, R. J. S. (2013). Settling velocity and mass settling flux of flocculated estuarine sediments. *Marine Geology*, *339*, 1–12. http://doi.org/10.1016/j.margeo.2013.04.006

Spahn, E. Y., Horner-Devine, A. R., Nash, J. D., Jay, D. A., & Kilcher, L. (2009). Particle resuspension in the Columbia River plume near field. *Journal of Geophysical Research*, *114*(May 2006), 1–16. http://doi.org/10.1029/2008JC004986

Sternberg, R., Creager, J., Glassley, W., & Johnson, J. (1977). Aquatic Disposal Field Investigations, Columbia River disposal site, Oregon. Appendix A. Investigation of the hydraulic regime and physical nature of bottom sedimentation. (Vol. U.S. Army). Vicksburg, Mississippi.

Stramska, M., & Dickey, T. D. (1998). Short-term variability of the underwater light field in the oligothrophic ocean in response to surface waves and clouds. *Deep-Sea Research Part I*, *45*, 1393–1410. http://doi.org/10.1016/S0967-0637(98)00020-X

Sutherland, J., Peet, A. H., & Soulsby, R. L. (2004). Evaluating the performance of morphological models. *Coastal Engineering*, *51*(8–9), 917–939. http://doi.org/10.1016/j.coastaleng.2004.07.015

Umlauf, L., Bolding, K., & Burchard, H. (2011). GOTM: Scientific Documentation, (Version 4.2), 346.

Umlauf, L., & Burchard, H. (2005). Second-order turbulence closure models for geophysical boundary layers. A review of recent work. *Continental Shelf Research*, *25*(7–8 SPEC. ISS.), 795–827. http://doi.org/10.1016/j.csr.2004.08.004

Van Leussen, W. (1988). Aggregation of particles, settling velocity of mud flocs a review. In *Physical processes in estuaries* (pp. 347–403). Springer. http://doi.org/10.1007/978-3-642-73691-9_19

van Rijn, L. (1993). Principles of Sediment Transport in Rivers, Estuaries and Coastal Seas. *Principles of Sediment Transport in Rivers , Estuaries and Coastal Seas*.

van Rijn, L. C. (1986). Mathematical modeling of suspended sediment in nonuniform flows. *Journal of Hydraulic Engineering*, *112*(6), 433–455. http://doi.org/10.1061/(ASCE)0733-9429(1986)112:6(433)

van Rijn, L. C., Walstra, D.-J. R., & van Ormondt, M. (2007). Unified View of Sediment Transport by Currents and Waves. IV: Application of

Morphodynamic Model. *Journal of Hydraulic Engineering*, *133*(7), 776–793. http://doi.org/10.1061/(ASCE)0733-9429(2007)133:7(776)

Vilibić, I., Šepić, J., Mihanović, H., Kalinić, H., Cosoli, S., Janeković, I., … Ivanković, D. (2016). Self-Organizing Maps-based ocean currents forecasting system. *Scientific Reports*, *6*, 22924. http://doi.org/10.1038/srep22924

Violeau, D., Bourban, S., Cheviet, C., Markofsky, M., Petersen, O., Roberts, W., … Weilbeer, H. (2002). Numerical simulation of cohesive sediment transport : intercomparison of several numerical models. *Fine Sediment Dynamics in the Marine Environment*, 75–89. http://doi.org/10.1016/S1568-2692(02)80009-2

Warner, J. C., Sherwood, C. R., & Geyer, W. R. (2007). Sensitivity of estuarine turbidity maximum to settling velocity, tidal mixing, and sediment supply. *Proceedings in Marine Science*, *8*, 355–376. http://doi.org/10.1016/S1568-2692(07)80022-2

Warner, J. C., Sherwood, C. R., Signell, R. P., Harris, K., Arango, H. G., Harris, C. K., … Arango, H. G. (2008). Development of a three-dimensional, regional, coupled wave, current, and sediment-transport model. *Computers & Geosciences*, *34*(10), 1284–1306. http://doi.org/10.1016/j.cageo.2008.02.012

Warrick, J. A. (2015). Trend analyses with river sediment rating curves. *Hydrological Processes*, *29*(6), 936–949. http://doi.org/10.1002/hyp.10198

Whitehouse, R., Richard, S., Roberts, W., & Mitchener, H. (2000). *Dynamics of estuarine muds*. Thomas Telford. http://doi.org/10.1680/doem.28647

Willmott, C. J. (1981). On the validation of models. *Physical Geography*, *2*(2), 184–194. http://doi.org/10.1080/02723646.1981.10642213

Winterwerp, J. C., Manning, a. J., Martens, C., de Mulder, T., & Vanlede, J. (2006). A heuristic formula for turbulence-induced flocculation of cohesive sediment. *Estuarine, Coastal and Shelf Science*, *68*(1–2), 195–207. http://doi.org/10.1016/j.ecss.2006.02.003

Wu, Y., Tang, C. C. L., Sathyendranath, S., & Platt, T. (2007). The impact of bio-optical heating on the properties of the upper ocean A sensitivity study using a 3-D circulation model for the Labrador Sea. *Deep Sea Research Part II: Topical Studies in Oceanography*, *54*(23), 2630–2642. http://doi.org/10.1016/j.dsr2.2007.08.019

Xu, J., Hood, R. R., & Chao, S.-Y. (2005). A Simple Empirical Optical Model for Simulating Light Attenuation Variability in a Partially Mixed Estuary. *Estuaries*, *28*(4), 572–580. http://doi.org/10.1007/BF02696068

Zhang, Y., & Baptista, A. M. (2008). SELFE: A semi-implicit Eulerian-Lagrangian finite-element model for cross-scale ocean circulation. *Ocean Modelling*, *21*(3), 71–96. http://doi.org/10.1016/j.ocemod.2007.11.005

Zhang, Y. J., Ye, F., Stanev, E. V, & Grashorn, S. (2016). Seamless cross-scale modeling with SCHISM. *Ocean Modelling*, *102*, 64–81. http://doi.org/10.1016/j.ocemod.2016.05.002

7 APPENDICES

APPENDIX A ANALYTICAL SOLUTION TO OPEN CHANNEL CASE

The semi-analytical solutions to the open channel case in Section 2.3.1 are derived below and are based on Warner et al (2007) and extended to analytical solutions (J.Paul Rinehimer, personal communication).

The key to deriving analytical and semi-analytical solutions to the open channel test case is to assume that the eddy viscosity profile has a parabolic shape:

$$K_{M(z)} = \kappa u_* z \left(1 - \frac{z}{D}\right) \tag{28}$$

where u_* is the friction velocity, z is the height above the bed, and H is the height of the water column.

By assuming a Prandlt number of 0.8 that is reasonable for the flow conditions, the eddy diffusivity is imposed as a constant where $K_H\ K_M/0.8 = 0.49$.

The analytical velocity profile is derived from the logarithmic velocity profile

$$u(z) = \frac{1}{\kappa}\left(\frac{z}{z}\right) u_* \tag{29}$$

where $\bar{u}$ is the depth average velocity in m s^{-1}, u(z) is the velocity at z m above the bed, $\kappa = 0.41$ is the von Karman constant, $z_0 = 0.0053$ is the bottom roughness, and $u_* = 0.0625$ is the friction velocity.

Because the channel is assumed to be in a steady state, the suspended sediment concentrations can be predicted assuming a Rouse profile with the Rouse parameter, P, given by

$$P = \frac{w_s}{\alpha \kappa u_*} \tag{30}$$

where w_s is the sediment settling velocity, α is the Prandlt number, κ is the von

Karman constant, and u_* is the friction velocity.

Applying the eddy diffusivity, K_H, the prescribed erosion rate, E, and settling velocity for the suspended sediment, w_s we can solve for the suspended sediment concentration

$$C(z) = \frac{E}{w_s}\left[\frac{z\,(H - z_0}{z_0(H - z)}\right]^{-P} \tag{31}$$

at height z above the bed with reference $z_0 = 0.0053$ for the test case.

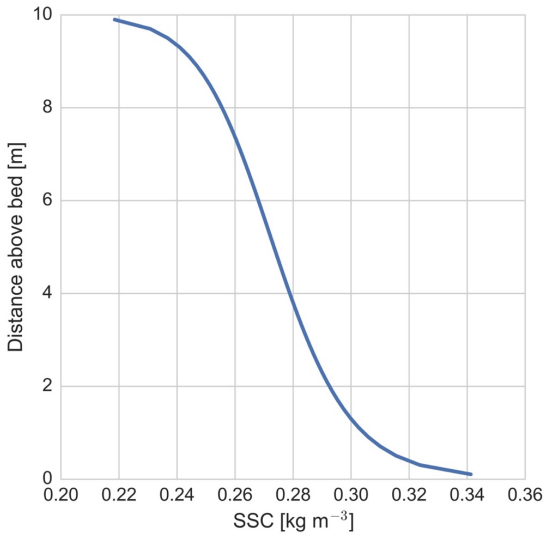

Figure 43 Profile of analytical solution to open channel case using z0 = 0.0053 assuming a no-slip bottom boundary condition, a logarithmic velocity profile, a Prandlt number of 0.8, and a Rouse profile.